Studies on Strain Rate Sensitivity of Bulk Multi-Phase Nanocrystalline Aluminium Based Alloys Evaluated by Nanoindentation

A thesis

Submitted by

Sreedevi Varam

in partial fulfilment of the requirement for the award of the degree of

Doctor of Philosophy

in

Materials Engineering

Under the supervision of

Dr. Koteswararao V Rajulapati

School of Engineering Sciences and Technology

December 2014

DECLARATION

I, **Varam Sreedevi**, declare that this thesis work entitled "**Studies on Strain Rate Sensitivity of Bulk Multi-Phase Nanocrystalline Aluminium Based Alloys Evaluated by Nanoindentation"**, submitted in partial fulfillment of the requirements for the award of **Doctor of Philosophy** (in Materials Engineering) in the School of Engineering Sciences and Technology (SEST), University of Hyderabad is completely my own work except for those referenced. This work was done under the supervision of **Dr. Koteswararao V Rajulapati**. This report is a record of bonafide work carried out by me and the results incorporated in it have not been reproduced / copied from any source. This work has not been submitted to any other University or Institute for the award of any other degree or equivalent.

Sreedevi Varam
Reg. No.: 09ETPM02
School of Engineering Sciences and Technology
University of Hyderabad

CERTIFICATE

This is to certify that the thesis work entitled "**Studies on Strain Rate Sensitivity of Bulk Multi-Phase Nanocrystalline Aluminium Based Alloys Evaluated by Nanoindentation**" submitted by **Sreedevi Varam** (Reg. No. **09ETPM02**) in partial fulfillment of the requirements for the award of the degree of **Doctor of Philosophy** in **Materials Engineering** is a bonafide work carried out by her under my guidance. The thesis work has not been submitted previously in part or in full to this or any other University or Institute for the award of any degree or equivalent.

Thesis supervisor

Dr. Koteswararao V Rajulapati
Assistant Professor
School of Engineering Sciences and Technology
University of Hyderabad

Approved by

Prof. Rajender Singh
Dean
School of Engineering Sciences and Technology
University of Hyderabad

ACKNOWLEDGEMENTS

I would like to express my special thanks to my project supervisor **Dr. Koteswararao V Rajulapati** for giving me an opportunity to work with him. I appreciate his encouragement, guidance and the constant support he has provided throughout the course of my research work. I have learned a lot from his suggestions, comments and discussions. I express my sincere gratitude to **Prof. K. Bhanu Sankara Rao** (former Dean) who has been my co-supervisor during his tenure at School of Engineering Sciences and Technology (SEST) for his wonderful suggestions.

I would like to thank the doctoral research committee members **Dr.-Ing. V.V.S. S. Srikanth** and **Prof. K.A. Padmanabhan** for invaluable suggestions provided during the review meetings. I am grateful to **Prof. R. Singh** (Dean) and all the faculty members of SEST for their support during the course of my work. I am thankful to **Prof. M. Sundararaman** (former Dean) for his encouragement and support.

I would like to thank Muvva D. Prasad, Center For Nanotechnology, University of Hyderabad for assisting in transmission electron microscopy (TEM) studies. Special thanks to Dr. Dibyendu Chakravarty, Scientist 'D' International Advanced Research Centre for Powder Metallurgy and New Materials (ARCI), Hyderabad; Dr. Tata Narasinga Rao, Scientist 'F', ARCI, Prof. B.S. Murty, IIT Chennai and Niraj (Ph D scholar), IIT Chennai, for assisting in spark plasma sintering (SPS). I am grateful to Nano facility (Prof. N. Ravishankar, Prof. Vikram Jayaram and Prof. Kamanio Chattopadhyay) of Indian Institute of Science Bangalore, for advanced TEM studies. I would like to thank Mr Kalyan Kamal, Scientist 'D', Defence Metallurgical Research Laboratory (DMRL), Hyderabad, for assisting in chemical analysis of the

samples. I am grateful to Anant Sagar and Dr. N. Eswara Prasad, Director, Regional Centre for Military Airworthiness (RCMA), Hyderabad, for assisting in microhardness measurements.

I am thankful to PVSL Narayana, former M Tech student, for providing the Al-W alloy sample for further investigations. I would like to thank Chandrasekhar, Rahul, Mohan, Pardhu, Supriya and Pramod for technical help. I am very thankful to all the SEST office staff and technical staff for their constant support and help. I am thankful to the B Tech project students Nagalakshmi and Aneesha. I am grateful to all my friends for their support. Special thanks to my friends, Radha, Ramya, Srilatha, Bhavana, Pavitra and Archana for their support.

I would like to thank Department of Science and Technology, Government of India, for funding the fast track project. I am thankful to University Grants Commission, New Delhi, India, for providing me the Junior Research Fellowship in Engineering and Technology.

Very special thanks to my husband Lalit, without whose encouragement and constant support my work would not have reached this stage. I am thankful to my beloved daughter Gayatri and my in-laws, who have been very supportive throughout. I am grateful to my brothers and sister-in laws for their constant support. I am deeply indebted to everyone who helped me directly or indirectly during my research. Finally, I would like to dedicate this work to my parents, without their love and support I would not be what I am today.

Sreedevi Varam

List of Publications

1. S. Varam, K.V. Rajulapati and K.B.S. Rao "Strain rate sensitivity studies on bulk nanocrystalline aluminium by nanoindentation", *Journal of Alloys and Compounds*, 585 (2014) 795-799.

   The article is featured in ***Advances in Engineering*** (***Advances in Engineering*** alerts the scientific and industrial community to innovative papers considered to be of importance to the progress in engineering technologies) as a **Key Scientific Article** contributing to excellence in engineering scientific and industrial research.

2. S. Varam, K.V. Rajulapati, K.B.S. Rao, R.O. Scattergood, K.L. Murty and C.C. Koch "Loading rate-dependent mechanical properties of bulk two-phase nanocrystalline Al-Pb alloys studied by nanoindentation", *Metallurgical and Materials Transactions A*, 45 (11) (2014) 5249-5258.

3. S. Varam, P.V.S.L. Narayana, M.D. Prasad, D. Chakravarty, K.V. Rajulapati, and K.B.S. Rao, "Strain rate sensitivity of bulk multi-phase nanocrystalline Al–W-based alloy", *Philosophical Magazine Letters*, 94(9) (2014) 582-591.

4. S. Varam, M.D. Prasad, K.B.S. Rao and K.V. Rajulapati "Strain rate sensitivity and modulus mapping studies on in-situ consolidated nanocrystalline multi-phase Al-Pb-W alloy by nanoindentation" – Submitted to *Journal of Materials Research* (2014).

5. S. Varam, K.V. Rajulapati and K.B.S. Rao "Structural details of mechanically alloyed nanocrystalline Al-Pb alloy powders", *Proceedings of International Conference on Electron Nanoscopy and XXXII Annual Meeting of EMSI* 2011, Hyderabad.

6. S. Varam, P.V.S.L. Narayana, K. Sreelatha, K.V. Rajulapati, D. Chakravarty and K.B.S. Rao "Loading rate dependence of mechanical properties in bulk nanocrystalline multi-phase materials", *Proceedings of the National Conference on Innovations in Chemical Engineering*, ICE-2013, BITS-Pilani, Hyderabad Campus, ISBN: 978-81-7800-329-0, 14-17.

Conferences Attended

1) Oral presentation on "Mechanical characterization of in-situ consolidated nanocrystalline Al-Pb-W alloy" at IUMRS-ICA-2013, December 16-20, IISc Bangalore, India.

2) Poster presentation on "Strain Rate Sensitivity Studies on Bulk Nanocrystalline Aluminium by nanoindentation" at International Symposium for Research Scholars on Metallurgy 2012, Materials Science and Engineering, IIT Madras. (Received the **Best Paper Award** for the poster presentation).

3) Poster presentation on "Evaluation of Loading Rate Dependent Mechanical Properties of Novel Engineering Materials at Small Length Scales" at 7th National Frontiers of Engineering Symposium For Young Engineers, 12-14 October 2012, IIT-Guwahati.

4) Oral presentation on "Processing and mechanical behavior of nanostructured bulk aluminum based alloys" at National Metallurgists Day Conference 2012, Jamshedpur.

5) Oral presentation on "Thermal stability and mechanical behavior of nanostructured high entropy alloys" at National Metallurgists Day Conference 2012, Jamshedpur.

6) Poster presentation on "Deformation characteristics at nano scale in Al-Pb system" at National Metallurgists Day Conference 2011, Hyderabad.

7) Poster presentation on "Structural Details of Mechanically Alloyed Nanocrystalline Al-Pb Alloy Powders" at International Conference on Electron Nanoscopy and XXXII Annual Meeting of EMSI 2011, Hyderabad.

8) Oral presentation on "Synthesis and Structural Details of Nanostructured Cu-Pb and Cu-Sn Alloys" at International Symposium for Research Scholars on Metallurgy 2010, Materials Science and Engineering, IIT Madras.

9) International Winter School on "Advances in Aeronautical Materials and Technologies – 2010", 15-21 December 2010, Taramati Baradari Heritage Complex, Hyderabad, India.

10) India-Singapore Joint Physics Symposium 2010, 06-08 January 2010, School of Physics, University of Hyderabad, Hyderabad.

Contents

List of Figures

Chapter 2

Chapter 3

Chapter 4

Chapter 5

Chapter 6

Chapter 7

Chapter 8

List of Tables

Chapter 3

Chapter 5

Chapter 8

Abstract

Aluminium and its alloys have extensive applications as structural materials mainly due to their high strength-to-weight ratio. It is well known that grain refinement is one of the major strengthening mechanisms used for improving the strength of materials through Hall-Petch strengthening. In recent years there has been a growing interest in understanding the deformation behavior of nanocrystalline (nc) metals/materials (average grain sizes < 100 nm). Nanocrystalline metal/alloy powders can be produced in bulk quantities by high energy ball milling. Retaining the nano structure is a grand challenge while consolidating nc powders. Spark plasma sintering (SPS) and cold sintering methods are used in the present work to produce the bulk samples from the synthesized powders.

Nanocrystalline Al, Al-Pb, Al-W, Al-Pb-W and Al-Bi alloys are fabricated using a combination of high energy ball milling followed by uni-axial pressing and/or SPS. Spark plasma sintering is employed for Al-Pb, Al-W and Al-Bi alloys. Bulk nc Al-Pb-W alloy/composite has been fabricated by *in situ* consolidation ball milling. Mechanical properties are evaluated using Vickers microindentation and depth sensing nanoindentation. The main aim of the current investigation is to study the rate sensitive deformation behavior of these alloys by nanoindentation. Nanocrystalline Al (~ 42 nm) consolidated using high-pressure compaction (~98% of theoretical density) showed an average hardness and elastic modulus values of 1.67 ± 0.09 GPa and 83 ± 8 GPa respectively at a peak force of 8000 μN and a strain rate of 10^{-2} s^{-1} when measured using a nanoindenter. High SRS values of 0.024 - 0.054 are obtained for nc Al which are high over conventional coarse grained Al.

Various nc Al-Pb alloys with Pb content of 1-4at.% have been synthesized. Al matrix in Al-2at.%Pb alloy had a grain size of 53 nm and Pb particle size was 6±2 nm. High angle annular dark field image obtained in STEM mode of TEM indicates the presence of Pb along the nc Al grain boundaries as well as dispersion of smaller Pb particles in the intra-granular regions. Hardness of Al-Pb alloys increased with increase in Pb content up to 2 at.% Pb addition, beyond that the hardness decreased for higher Pb additions of 3% and 4%. The initial hardening behavior is explained based on the interplay between grain boundary weakening and particle strengthening. Strain rate sensitivity has increased with increase in Pb content reaching a value

of 0.1 for Al-4at.%Pb alloy. Activation volumes measured are between 2.84-6.15 b^3. Higher SRS and lower activation volume suggest that grain boundary mediated processes are controlling the deformation characteristics.

In case of Al-10at.%W alloy, transmission electron micrographs revealed that nanocrystalline intermetallic $Al_{12}W$ phase with an average particle size of 175 nm is uniformly distributed in the nc Al matrix with a grain size of 40 nm. At room temperature, the alloy exhibited high SRS of 0.025±0.002 and low activation volume of 1.63-3.88 b^3. The structural studies on *in-situ* consolidated Al-Pb-W alloy indicated nc structure having an average grain size of ~ 23 nm. The consolidated bulk sample is having a nano hardness value of ~ 1.5 GPa for an applied peak force of 8000 µN with a loading rate of 400 µN/s. The material showed a high SRS value of 0.071±0.004 which is a good measure of ductility. The modulus mapping studies of the bulk sample enabled mapping of elastic modulus of the material surface by dynamic mechanical analysis. Nanoindentation studies on the hardness behavior of nc Al with Bi addition showed reduction in hardness with increasing Bi content. The alloys were found to be unstable in air and hence these alloys might not be good candidates for structural applications. These alloys were observed to be highly reactive in water and in future, experimental studies on possible production of hydrogen gas from these alloys shall be considered.

Chapter 1 - Introduction

Grain refinement is one of the major strengthening mechanisms used for improving the strength of engineering materials through Hall-Petch strengthening [1]. Interest in synthesis and processing of nanocrystalline/nanostructured materials (average grain sizes < 100 nm) is growing, due to their unique mechanical and physical properties [2-6]. Nanocrystalline (nc) materials have potential applications as structural materials mainly due to their high strength. Aluminium and its alloys have an added advantage of high strength-to-weight ratio [7]. Nanocrystalline metal/alloy powders can be produced by several processing routes and ball milling is being used in producing these powders in bulk quantities [8]. Retaining the nano structure is a big challenge while consolidating nc powders. Fine grain structure can be retained by sintering the powders at lower temperatures and high applied pressures.

The deformation behavior of nc materials has been fascinating as it distinctly differs from that of coarse grained materials [4]. Finer grain size yielded higher strength values in nc single phase materials but at the expense of ductility [9]. Therefore, acceptable ductility levels should also be available along with strength in these materials for potential structural applications. Strain rate sensitivity (SRS) and activation volume are important parameters in a plastic deformation process [10]. SRS is a qualitative indicator of ductility of a given material, with higher SRS value means more ductility [11]. While suggesting strategies to improve ductility of nc materials, Koch [12] indicated that incorporation of a second phase could delay the onset of localized deformation under tensile loading conditions. Although extensive research investigations have been carried out to explore the mechanical behavior of various single phase

nc materials, studies that address the influence of a nano sized second phase dispersed in an nc matrix with an average grain size less than 100 nm are very limited as on today [13].

Bulk nc Al, Al-Pb, Al-W, and Al-Bi alloys are fabricated using a combination of high energy ball milling followed by uni-axial pressing and/or spark plasma sintering. Bulk nc Al-Pb-W alloy/composite has been fabricated by *in situ* consolidation ball milling. Mechanical properties are evaluated using Vickers microindentation as well as depth sensing nanoindentation. The aim of the current investigation is to study the rate sensitive deformation behavior of bulk nc materials by nanoindentation. When enough sample sizes are not available to measure ductility and other mechanical properties as per ASTM standards, as is the case with nc materials, nanoindentation is a very promising technique to evaluate various mechanical properties including strain rate sensitivity. Nanoindentation was performed at different peak loads and loading rates to calculate SRS and activation volume associated during the deformation process. Nanoindentation also enabled scanning probe microscopy (SPM) imaging of the indent to study the plastic deformation region around the indent made on the bulk samples. Modulus mapping studies also have been carried out on Al-Pb-W alloy using nano indenter to study the distribution of dispersions in Al matrix.

1.1 Motivation

Retaining the nanostructure is a big challenge in processing of bulk nc materials. Fabricating these bulk nc materials, which can be tested for mechanical properties (strength, ductility) as per ASTM testing procedures, is another challenging task as on today. Extensive work has been carried out on the mechanical behavior of single phase nc materials where in the grain size and the grain size distribution govern the mechanical properties. When a second phase (which is also

nanocrystalline) is added to the nc matrix, various other factors like the second phase grain size / particle size, size distribution, etc also effect the mechanical properties. The interesting and superior mechanical properties of nc materials have thrown a grand challenge to the scientific community in the form of several uncertainties and unanswered questions while unfolding the underlying deformation mechanisms. There is a limited data available on the deformation characteristics of multi-phase nc materials especially strain rate sensitivity. In order to address this, the current study has been undertaken.

1.2 Objectives and scope

With the above-mentioned current status and motivation, the objectives of this work are:

- Fabrication of bulk nanocrystalline Al with an average grain size < 100 nm.
- Fabrication of bulk multi-phase nanocrystalline Al-Pb, Al-W, Al-Pb-W and Al-Bi alloys
- Detailed characterization of above mentioned multi-phase nanocrystalline alloys using XRD, TEM etc.
- Understanding the loading rate dependence of flow stress in all these alloys by evaluating SRS and activation volume.
- Identifying the role of nature of reinforcement and its crystal structure on overall SRS and activation volume
- Evaluation of structure-property correlations

1.3 Overview of the thesis

Chapter 2 presents the available literature on synthesis of nc powders, various consolidation processes to make them into bulk form and mechanical behavior of nc materials. Studies on SRS and activation volume of nc materials are discussed in detail. Chapter 3 discusses the

experimental techniques used in the current study. High energy ball milling process has been discussed in detail. High pressure consolidation at room temperature and spark plasma sintering processes are presented briefly. Structural and mechanical characterization techniques employed are also presented.

The results of the current thesis work are discussed in the following chapters, Chapter 4 to Chapter 8. Chapter 4 deals with the processing and mechanical properties of bulk nc Al. Details of structural characterization are also discussed. This chapter is based on the journal article, S. Varam, K.V. Rajulapati, K. Bhanu Sankara Rao, *Journal of Alloys and Compounds*, 585 (2014) 795. Chapter 5 presents the mechanical properties and the underlying deformation mechanisms of Al-Pb nanocomposites. Hardness, SRS and activation volume of these two-phase materials are discussed. This chapter is based on the journal article, S. Varam, K.V. Rajulapati, K.B.S. Rao, R.O. Scattergood, K.L. Murty and C.C. Koch, *Metallurgical and Materials Transactions A*, 45 (2014) 5249-5258. Chapter 6 is on structural and mechanical characterization of Al-W alloys. This chapter is based on the journal article, S. Varam, P.V.S.L. Narayana, M.D. Prasad, D. Chakravarty, K.V. Rajulapati and K.B.S. Rao, *Philosophical Magazine Letters*, 94 (2014) 582-591. Chapter 7 discusses the work on in-situ consolidated nanocrystalline Al-Pb-W ternary alloy. This chapter is based on the journal article, S. Varam, M.D. Prasad, K.B.S. Rao and K.V. Rajulapati, Strain rate sensitivity and modulus mapping of *in-situ* consolidated nanocrystalline Al-Pb-W alloy, 2014, submitted to *Journal of Materials Research*. Chapter 8 includes the effect of Bi addition on the structural evolution and hardness behavior of nc Al. Chapter 9 presents the summary and conclusions of the entire work. Future scope of the work is presented in Chapter 10.

References

[1] G.E. Dieter, Mechanical metallurgy, third ed. ed., McGraw-Hill Book Company, Boston, 1986.

[2] H. Gleiter, Nanostructured materials: basic concepts and microstructure, Acta Materialia, 48 (2000) 1-29.

[3] H. Gleiter, Nanocrystalline materials, Progress in Materials Science, 33 (1989) 223-315.

[4] M.A. Meyers, A. Mishra, D.J. Benson, Mechanical properties of nanocrystalline materials, Progress in Materials Science, 51 (2006) 427-556.

[5] K.S. Kumar, H. Van Swygenhoven, S. Suresh, Mechanical behavior of nanocrystalline metals and alloys, Acta Materialia, 51 (2003) 5743-5774.

[6] C. Suryanarayana, C.C. Koch, Nanocrystalline materials – Current research and future directions, Hyperfine Interactions, 130 (2000) 5-44.

[7] ASM Specialty Handbook: Aluminum and Aluminum Alloys, ASM International, 1993.

[8] C. Suryanarayana, Mechanical alloying and milling, Progress in Materials Science, 46 (2001) 1-184.

[9] C.C. Koch, D.G. Morris, K. Lu, A. Inoue, Ductility of nanostructured materials, MRS Bulletine, 24 (1999) 54-58.

[10] R.J. Asaro, S. Suresh, Mechanistic models for the activation volume and rate sensitivity in metals with nanocrystalline grains and nano-scale twins, Acta Materialia, 53 (2005) 3369-3382.

[11] M.Y. Wu, O.D. Sherby, Superplasticity in a silicon carbide whisker reinforced aluminum alloy, Scripta Metallurgica, 18 (1984) 773-776.

[12] C.C. Koch, Optimization of strength and ductility in nanocrystalline and ultrafine grained metals, Scripta Materialia, 49 (2003) 657-662.

[13] C.C. Koch, R.O. Scattergood, K.L. Murty, The Mechanical Behavior of Multiphase Nanocrystalline Materials, JOM, 59 (2007) 66-70.

Chapter 2 – Literature Review

2.1 Nanocrystalline materials

Interest in synthesis and processing of nanocrystalline/nanostructured materials (average grain sizes < 100 nm) is growing due to their improved mechanical, physical and chemical properties [1-6]. Nanocrystalline (nc) materials are single phase or multi-phase polycrystalline materials with nano scale grain size. Schematic representation of atomic arrangement in a nanocrystalline material is shown in Fig. 2.1 [1]. The atoms inside the crystals are represented as solid circles and the atoms in the inter-crystal region are represented by open circles. In these materials, significant volume fraction of atoms is present in the inter-crystal region i.e. the grain boundary area, triple junctions, quadruple junctions, etc. As the grain size decreases, the fraction of inter-crystal region increases. The superior properties of nc materials [1] have been attributed to the presence of these interfacial regions.

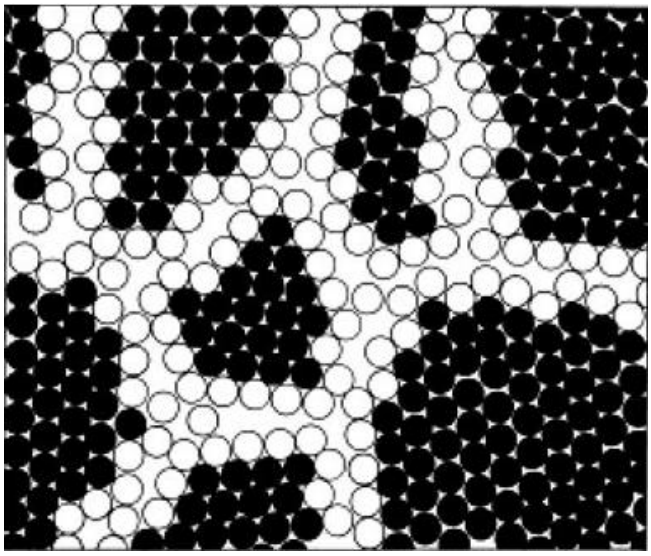

Fig. 2.1 Two-dimensional model of a nanocrystalline material with atoms in the grain interiors indicated as solid circles and the atoms in the inter-crystal regions represented as open circles [1].

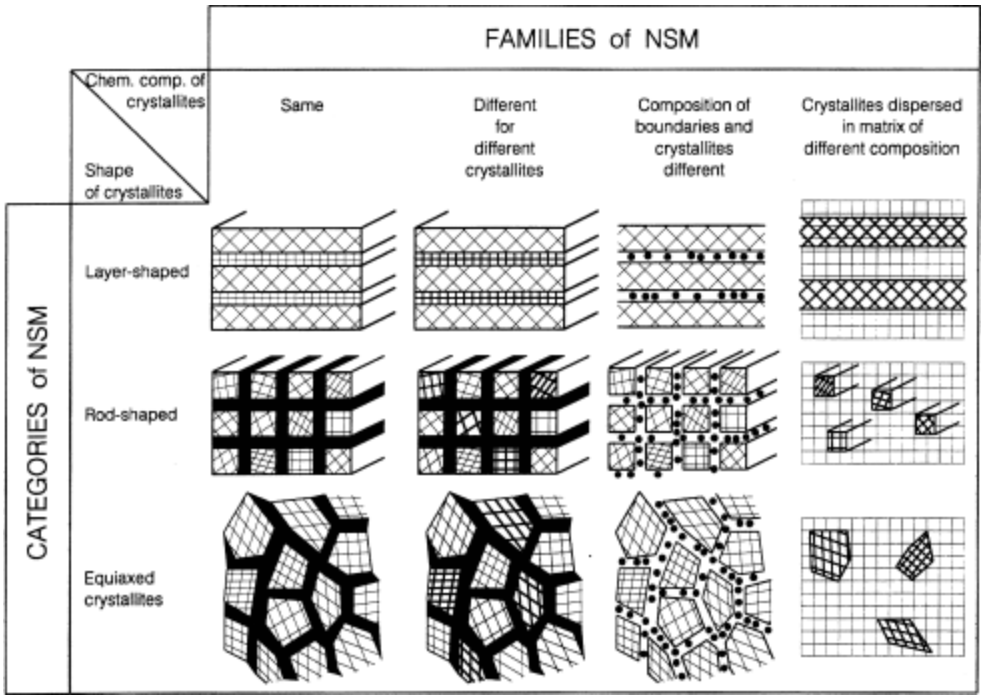

Fig. 2.2 Classification scheme for nanostructured materials according to their chemical composition and the shape of the crystallites (structural elements) forming the nanostructure [1].

Gleiter has classified nanostructured materials based on chemical composition and shape of the crystallites [1]. The classification scheme is depicted in Fig. 2.2. The current study is on materials with equiaxed crystallites (a) having boundaries of different composition and (b) dispersed in matrix of different composition.

2.2 Processing of nanocrystalline materials

There are two basic approaches of synthesizing nc materials – *bottom-up* approach and *top-down* approach. In *bottom-up* approach, the nanostructure is arranged atom-by-atom, layer-by-layer where as in *top-down* approach, the bulk material's initial structure is disintegrated to obtain a nanostructure. The common synthesis methods are [3] as follows

- Inert gas condensation [7]
- Mechanical alloying/milling [8, 9]
- Cryomilling [10]

- Severe plastic deformation [11, 12]
- Crystallization from amorphous material [13, 14]
- Plasma synthesis [15, 16]
- Electrodeposition [17]
- Pulse electrodeposition [18, 19]
- Sputtering [20, 21]
- Chemical vapor deposition [22]
- Physical vapor deposition [22]
- Spark erosion [23]

Each of these methods has its own advantages and disadvantages. Nanocrystalline powders are typically produced from inert gas condensation, mechanical alloying or cryomilling and the resultant powders are further consolidated to bulk form. The material yield is low with inert gas condensation technique. Though the material can be produced in reasonable quantities using mechanical alloying, maintaining the material purity is difficult. Retaining the nanostructure after consolidation of the powders is another challenging task. Purity can be maintained using severe plastic deformation techniques (high pressure torsion, equi-channel angular pressing) but, they generally lead to material with ultra-fine grain sizes. Bulk metallic glasses having controlled two-phase microstructures are produced by crystallization of amorphous material [4] but, this technique is limited to glass-forming compositions. Electrodeposition techniques are employed for a wide range of materials such as metals, alloys and composites and yield porosity-free products [17, 18].

In the present investigation, mechanical milling has been used to synthesize the nc powders. Hence, it is discussed in detail along with various consolidation processes used to produce bulk

materials from nc powders. The literature on i*n situ* consolidation ball milling has also been discussed.

2.2.1 Synthesis of nanocrystalline powders by mechanical alloying/milling

Mechanical alloying is a powder metallurgy processing technique used to synthesize equilibrium as well as non-equilibrium phases of materials from elemental powders [24]. This is a solid-state processing technique and hence alloying of immiscible elements is also possible with this technique. This technique was first developed by John S. Benjamin [25, 26] to synthesize oxide-dispersion strengthened nickel- and iron-base superalloys. This is an effective processing technique which can be applied to metals, ceramic, polymers and composite materials. Main advantages of mechanical alloying are [24]:

- Fine dispersions of second phase particles
- Extended limits of solid solubility
- Grain size refinement to nanometer range
- Synthesis of novel quasi-crystalline phases
- Production of amorphous phases
- Possible alloying of alloy systems with large miscibility gap

The term mechanical alloying is generally used when different metals or alloys/compounds are involved in milling. During mechanical alloying material transfer takes place which leads to the formation of a homogeneous alloy. Mechanical milling involves milling of pure metals, intermetallics or pre-alloyed powders and homogenization is achieved without the need of material transfer.

2.2.1.1 Mechanism of alloying

During mechanical alloying which is carried out in a ball mill, the powder particles get cold welded, fractured and re-welded. The mechanism of nanostructure formation by mechanical alloying was first proposed by Fecht et al. [9]. The explanation was given based on the transmission electron microscopy (TEM) studies of ball milled powders of Ru and AlRu. The nanostructure formation was expected to occur in three stages as follows:

- Stage 1. Localized deformation occurs in shear bands with higher dislocation density.
- Stage 2. Dislocations are rearranged to form cells/subgrains with nanosclae dimensions
- Stage 3. Low-angle grain boundaries disappear due the re-arrangement of grains and high-angle grain boundaries are formed by grain boundary rotation/sliding.

Large variety of metal-based and ceramic-based nanocomposites have been produced by mechanical alloying [27]. There are various types of mills (planetary ball mill, attritor mills, shaker mills, etc.) available to produce mechanically alloyed powders. Shaker mills are the most widely used mills for carrying out investigations in the laboratory. The vial containing the powder sample and grinding balls moves back and forth several thousand times a minute tracing "figure-8" resulting in very high impact of balls against the sample. Hence, these mills are considered as high energy ball mills and they have been in use to refine the grain size of materials to the nano scale. Using high energy ball mills, the minimum grain size can be achieved in less time when compared to low energy ball mills such as planetary ball mil. As the milling time is increased, the grain size decreases reaching a steady state after certain period of time.

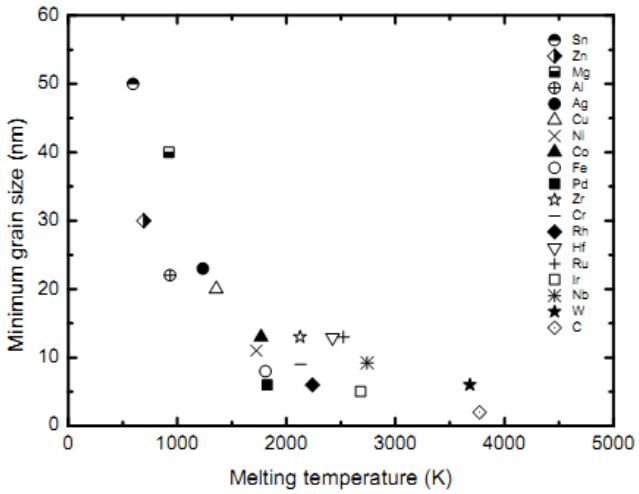

Fig. 2.3 Minimum grain size obtainable for various elements vs their melting temperature [28].

Various process variables and the properties of materials being milled influence the minimum grain size that can be obtained. Investigations on milling of face-centered cubic (fcc) metals revealed that the minimum obtainable grain size is inversely proportional to the melting temperature of the metal [28]. This data was obtained from experiments conducted by several research groups using different equipment and is depicted in Fig. 2.3.

Other than the type of mill, milling time and the material being milled, the following process parameters also influence the formation of nanostructure:

- Milling media
- Ball to powder weight ratio
- Milling temperature
- Process controlling agent

Selecting the right milling media is very essential to avoid/minimize contamination of the material being milled. The material of the milling media is preferred to be the same as the material being milled. Common materials that are used as milling media are hardened steel, tool steel, tungsten carbide, stainless steel, etc. The rate of refinement of grain size increases with

increasing milling time and it also increases with higher ball-to-powder weight ratios as shown in Fig. 2.4 [24]. Generally, ball-to-powder weight ratios of 5:1 or 10:1 are used in most of the research studies. The temperature of milling also affects the rate of milling. The lower temperatures (cryomilling) help in attaining the nano grain structure in less time by suppressing the recovery rates. The powder particles tend to become brittle at low temperatures, thus, resulting in effective milling. For ductile materials, process controlling agent (PCA) is added during milling to avoid the powder particles getting cold welded to the walls of the vial as well as to the balls. The PCA gets adsorbed on the surface of the powder particles and lowers the surface tension by acting as surfactants. Since the energy required for milling is the product of surface tension and the new surface area generated, lowering of surface tension results in lowering of the milling time. The PCAs are mostly organic compounds which include stearic acid, methanol, ethanol, acetone, toluene, etc. Usually 1 to 4 wt.% of the total charge material is added as PCA. Addition of PCA usually introduces some impurities in the final product, hence, for high-purity alloys the use of PCA should be avoided.

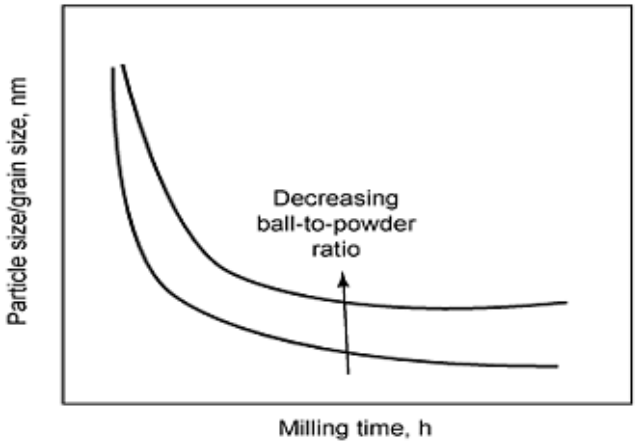

Fig. 2.4 Variation of grain size with milling time, the effect of ball-to-powder weight ratio is also shown [24].

2.2.2 Consolidation of nanocrystalline powders

Retaining the nano structure is a big challenge while consolidating nanocrystalline powders. Densification of nc powders occurs at relatively lower temperatures when compared to microcrystalline materials and the activation energies for sintering are also observed to be much lower for these materials [29, 30]. Generally, nc powders tend to sinter at temperatures of 0.2 - 0.4 T_m as compared to 0.5 - 0.8 T_m for conventional microcrystalline powders [29, 30]. Various manufacturing processes like sinter forging, hot isostatic pressing and cold sintering (high pressure consolidation) are already in use for consolidation of these materials. Pressure levels of above 1 GPa are often used in pressure-assisted consolidation methods to overcome the large interfacial friction effect [29]. Hot processing methods might result in considerable coarsening of nanocrystalline structure [29]. Fine grain structure can be retained by sintering the powders at lower temperatures and high applied pressures. Warm compaction method has been in use to improve the density of Al and its alloys [31, 32]. Under high applied pressures, the oxide layers formed on the powder particles can be broken leading to enhanced densification. Densification occurs due to plastic deformation as well as surface diffusion at particle interfaces.

2.2.2.1 Cold sintering - high pressure consolidation

Cold sintering involves application of very high pressures at room temperature or temperatures below 450 ^{0}C to consolidate powders [33-35]. Full densities can be achieved without compromising the fine grain structures. Generally reduction treatment is given to the powder particles to remove the surface oxide layer on the particle surfaces. Plastic deformation of powder particles leads to the formation of chemical bonds through diffusion of atoms across particle surfaces. Cold sintering of nc Al, nickel and iron powders as well as nanocomposites

resulted in >99% of theoretical density [34]. These materials exhibited high strength and microhardness values after cold sintering.

2.2.2.2 Spark plasma sintering

In spark plasma sintering (SPS), high temperature plasma is generated between the powder particles by electrical discharge. The ON-OFF DC pulse energizing method is used which generates spark plasma, spark impact pressure, Joule heating and electrical field diffusion effect [36]. In this process, the surface oxide layers on the powder particles are easily removed and material transfer is promoted by diffusion resulting in high quality sintered products. This technique is mainly used for functionally graded materials, intermetallic compounds, and various types of ceramics and composites which are difficult to sinter using conventional sintering techniques. Sintering occurs at much lower temperatures and in shorter times when compared to conventional sintering techniques such as hot pressing, hot isostatic pressing (HIP), etc. Hence, it can be considered as a rapid sintering technique which can be used to consolidate nc powders so that the nanostructure is retained in the final end product.

The basic setup of a SPS system is depicted in Fig. 2.5 [36] which illustrates the operation of SPS. The SPS system consists of a sintering die, vacuum and water cooling chamber, DC pulse generator which is connected to the upper and bottom punch electrodes, a sintering press and a SPS controller. SPS controller is attached to a positioning unit, water cooling control unit and an atmosphere (vacuum/air/argon) control unit. The advantages of SPS over conventional sintering methods include ease of operation, high reproducibility and reliability. Ceramic materials such as silicon carbide and silicon nitride have been successfully fabricated using SPS technique [37, 38]. Various surface engineered coatings including ceramic and nanocomposite coatings have been successfully prepared using this technique [39-41].

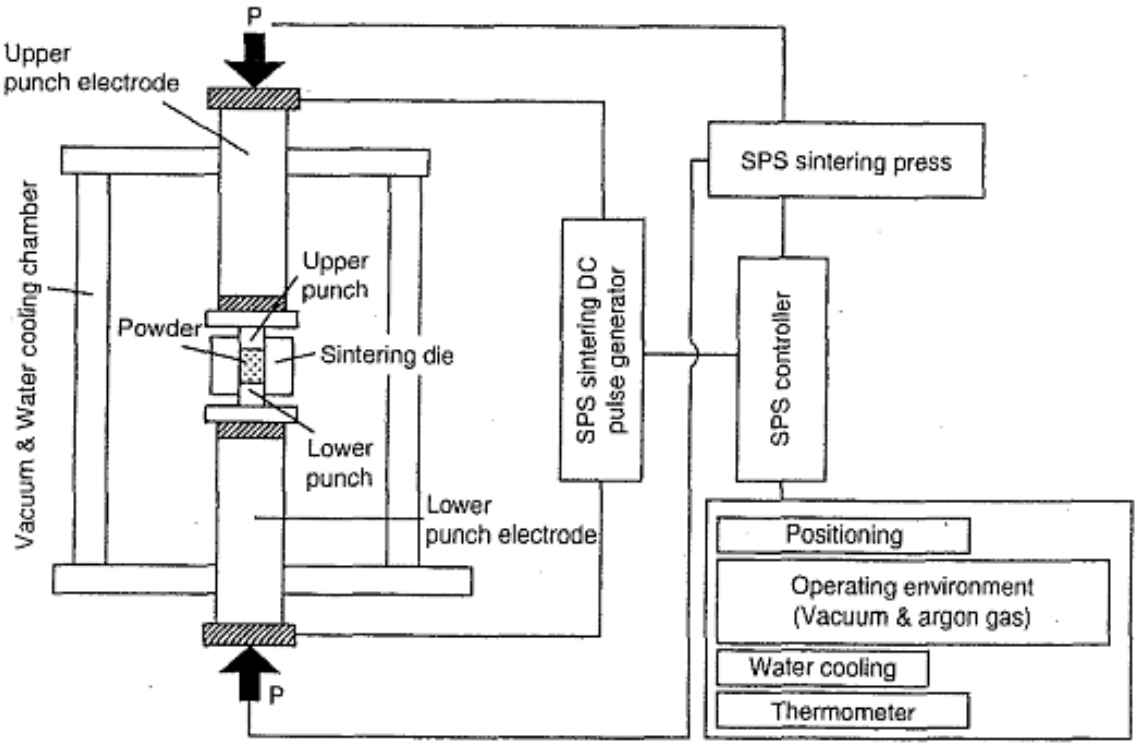

Fig. 2.5 General configuration of a spark plasma sintering system [36].

2.2.3 *In situ* consolidation ball milling

In situ consolidation ball milling has been developed to produce artifact-free bulk nc samples for various ductile metals and alloys such as Zn, Al and its alloys, Cu and its alloys, etc. [42]. In artifact-free nc materials high strength can achieved along with good ductility. Porosity was one of the major artifacts in materials developed by consolidation of ball milled nc powders which is a two-step process. Through advanced processing techniques even though density close to the theoretical density was obtained with no porosity, the inter particle bonding may be lacking. *In situ* consolidation method avoids the additional step of consolidation of nc powders in fabricating bulk nc materials. Excessive cold welding of pure Al during ball milling was reported by Gilman and Nix [43].

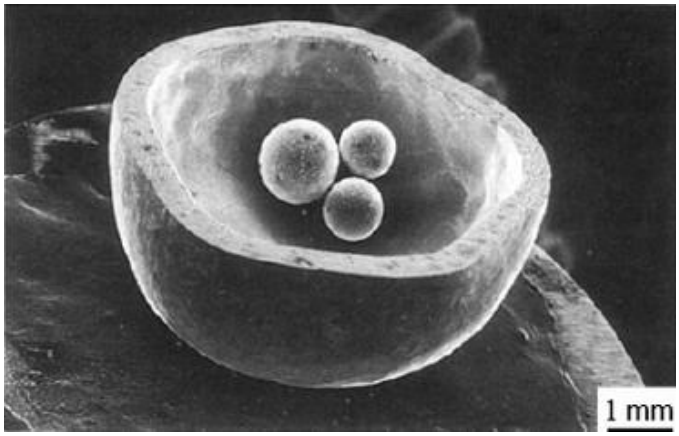

Fig. 2.6 SEM micrograph of a sectioned particle of Cu (containing smaller particles inside) formed by milling Cu powder for 222 hours [44].

Cold welding of powder to powder in the absence of a surfactant resulted in the formation of irregularly shaped spheres of 1-7 mm in diameter but, these were found to be having large internal voids. Prolonged milling of copper powder in a ball mill resulted in particles of 7-8 mm diameter [44]. When these particles were sectioned, smaller particles were found within them as shown in Fig. 2.6. Smaller particles were again hollow and contained even smaller particles, which the researchers termed as "Russian doll effect". Such fascinating observations led to further research on *in situ* consolidation ball milling. This process usually involves a combination of low temperature (liquid nitrogen temperature, below 77K) and room temperature ball milling of powder particles [42]. The irregular/spherical balls formed can be pressed into disks of ~ 10 mm diameter and can be further subjected to mechanical property measurements. The materials fabricated by this process exhibited improved mechanical properties such as good ductility along with high strength [42]. The mechanical properties of metals and alloys produced by this process are discussed in detail in the subsequent section. The major disadvantage of this technique is that the samples produced are limited in size.

2.3 Mechanical properties of nanocrystalline materials

Interest in the study of mechanical properties of nanocrystalline materials is increasing in recent years since these materials exhibit superior mechanical properties over conventional coarse grained materials. Some of these properties include ultra-high strength, high hardness, improved wear resistance and superplasticity at lower temperatures and higher strain rates. But, most of the investigations on nanostructured bulk materials resulted in low ductility along with high strength [4]. Some of the properties of these materials are discussed in the following sections.

2.3.1 Elastic properties

The early elastic modulus measurements on nc materials produced by inert- gas-condensation method were lower than the values obtained for conventional grain size materials [45]. Krstic et al. [46] suggested that the observed lower values of Young's modulus, E, were due to the presence of extrinsic defects for example pores, cracks, etc. Nanoindentation studies [47] on the Young's modulus of nc Ni, Cu and Cu-Ni synthesized by mechanical milling/alloying, showed E values identical to those of conventional grain size materials. Based on a model Shen et al. [47] have shown the dependence of ratios of Young's (E) and Shear (G) moduli of nanocrystalline Fe to those of conventional grain size Fe as a function of grain size (Fig. 2.7). The solid and dashed curves correspond to the grain boundary thickness of 1 nm and 0.5 nm respectively. The data for nc Fe is shown in open circles, which is closely matching with the plot for 0.5 nm grain boundary thickness. It was concluded that nc materials possess the same values of intrinsic moduli as those of coarse grained materials except for materials with grain sizes lower than 5 nm.

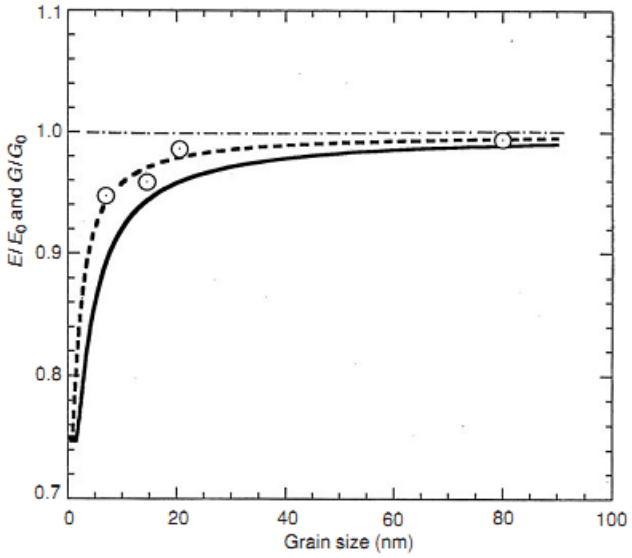

Fig. 2.7 Calculated ratios of Young's and Shear modulus of nanocrystalline Fe to those of polycrystals as a function of grain size [47].

Even though the *E* values of nc materials were found to be slightly less than their coarse grained counterparts especially at very finer grain sizes [48, 49], Liu et.al [50] also have reported an *E* value of 91.8 GPa for nano Al having a grain size of about 100 nm.

2.3.2 Hardness and strength

The variation of flow stress as a function of grain size is schematically represented in Fig. 2.8 [4]. In microcrystalline (mc) and ultrafine crystalline (ufc) metals and alloys having grain size larger than 100 nm, the strengthening with decreasing grain size is as per the Hall-Petch mechanism which is as given by the following equation [51, 52]:

$$\sigma_y = \sigma_o + kd^{-1/2} \qquad (2.1)$$

where σ_y is the yield strength, σ_o is the friction stress, k is the Hall-Petch slope and d is the grain size. In mc and ufc regimes the strengthening is due to pile-up of dislocations at grain boundaries, resulting in enhanced resistance to plastic flow.

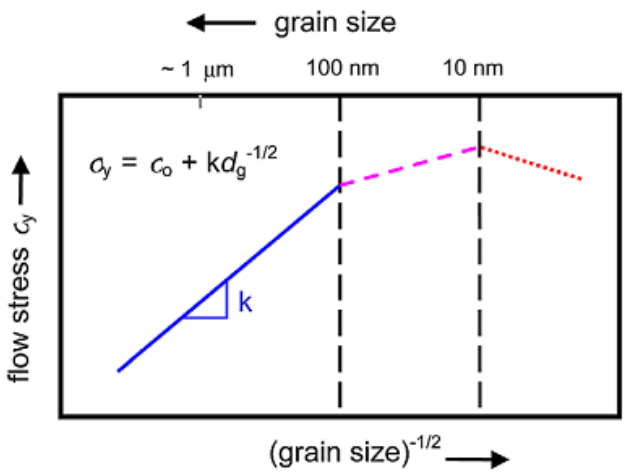

Fig. 2.8 Variation of flow stress with grain size [4].

As the grain size is lowered to nanocrystalline regime (~10-100 nm range), there is a deviation in the slope of the Hall-Petch plot. The deformation mechanisms responsible for the behavior in nc regime are still not very clear. Further refinement (below 10 nm) results in weakening of the metal, which is also termed as the inverse "Hall-Petch" type relationship. It is predicted that the deformation in this regime involves mechanisms other than conventional dislocation generation and motion [53, 54]. Since nc materials cannot be produced in sufficient sizes in order to perform standard mechanical testing, hardness is the most measured property which is usually measured by either microindentation or nanoindentation. Strength and hardness values of nc metals have been found to be much larger than those of conventional grain size metals. Yield strength of nc Cu (23 nm) was found to be 22 times that of conventional grain size Cu [55]. Shen and Koch [56] worked on nc solid solution alloys and found that their strength depends on solid-solution hardening as well as grain-boundary hardening. They also explained that the major contribution to the increased strength is from grain-boundary hardening. Intermetallic compounds also exhibited increased strength with decrease in grain size [57].

Considerable work has been carried out on multiphase materials having nanoscale second phases in an amorphous matrix [58]. Studies on multiphase nc materials with nc matrix have been limited. Experimental studies on Al-Pb nanocomposites processed by ball milling and consolidation [59] showed increased hardness for small amounts of softer Pb additions (up to 5 wt.%). The Al matrix was microcrystalline where as the second phase Pb particles were in nano size. In later studies by Rajulapati et.al, addition of Pb to nc Al resulted in softening of the matrix [60]. Hardness decreased with increasing amount of Pb addition. The decrease in hardness was attributed to the segregation of Pb atoms at Al grain boundaries. Supporting these results, molecular dynamic straining simulations carried out [61] for Al-Pb alloys with 1 to 3 at.% Pb addition showed decreased yield stress with increasing Pb content.

Investigations on nanostructured Al-20wt.%Sn alloy [62] resulted in both hardening and softening of the Al matrix. Sintering of ball milled powders below eutectic temperature (487 K) resulted in homogeneous distribution of Sn in Al and sintering above eutectic temperature resulted in inhomogeneous distribution and this behavior in-turn resulted in hardening and softening effect respectively in nc Al-Sn system. Hence the size and distribution of second phase particles in the matrix greatly influence hardness of the composite. The harder second phase (W) dispersions in nc Al resulted in increase in hardness and it was attributed to the Orowan particle strengthening mechanism [63].

2.3.3 Ductility

Most of the investigations on nanostructured bulk materials resulted in high strength, but low ductility. The low ductility of nc materials was attributed to the presence of pores and other artifacts. The other reasons for limited ductility are identified as force instability in tension and instability in crack nucleation or crack propagation. Hence, optimization of strength and ductility

is challenging in nc materials. Koch [64] suggested that material with the ability for strain hardening is essential to prevent the premature failure in nanocrystalline materials and for this reason the material has to be artifact-free. He indicated that bimodal grain size distribution with few larger grains helps in sustaining the dislocation activity which is needed for strain hardening. Investigations by Wang et al. [65] on thermomechanical treatment of Cu resulted in bimodal grain size distribution leading to high strength and high tensile ductility.

In situ consolidation ball milling of various ductile metals (Cu, Zn, Al) and alloys has been reviewed by Koch et al. [42] which results in artifact free bulk samples. This process was used to make nc Zn [66] and Al-Mg alloy [67] having high strength and good ductility. As shown in Fig. 2.9, nc Cu made by this process [68] showed improved ductility when compared to nc Cu produced by inert gas condensation technique [69].

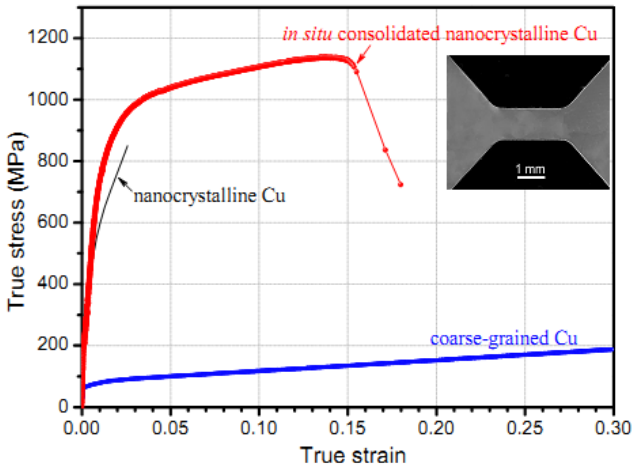

Fig. 2.9 Tensile stress-strain curves of in situ consolidated nc Cu, nc Cu produced by inert gas condensation and coarse grained Cu [68].

2.4 Deformation mechanisms in nanocrystalline materials

The specific behavior of high strength but low ductility of nanocrystalline materials led to the extensive research in understanding the deformation characteristics of these materials. The deformation mechanisms that are responsible for conventional polycrystalline materials cannot be simply extrapolated to nc materials. Based on experimental and simulation results, following mechanisms are expected to be operative in nc materials:

2.4.1 Pile-up breakdown

The Hall-Petch effect (strengthening due to decrease in grain size) has been due to the pile-up of dislocations at the grain boundary. As the grain size is decreased to the nc regime, the number of dislocations piling up at the grain boundary decreases, at an applied stress level and eventually the Hall-Petch relationship breaks down. Wadsworth and Nieh [70] assumed that at certain point each grain in a polycrystalline material will be able to support only one dislocation. They predicted the grain size values for various materials at which the Hall-Petch relation breaks down. Under equilibrium the spacing between dislocations, l_c, is given as

$$l_c = \frac{3Gb}{\pi(1-\nu)H} \qquad (2.2)$$

Where G is the shear modulus, H is the hardness, b is the Burger's vector and ν is the Poisson's ratio. When the grain size, d is smaller than l_c, the Hall-Petch relation will break down due to the absence of dislocation pile-ups. Therefore,

$$d = \frac{3Gb}{\pi(1-\nu)H} \qquad (2.3)$$

2.4.2 Grain-boundary sliding

During grain-boundary sliding, one layer of grain slides over the other which produces shear strain in the process. Hahn et al. [71, 72] have proposed that this is one of the dominant deformation mechanisms in nc materials having grain size less than 50 nm. This is also the principal mechanism in superplasticity. The following hardness (H_v) relationships have been proposed by Hahn et al. [71]

$$H_v = H_0 + \frac{k}{\sqrt{d}} \qquad (2.4)$$ in the dislocation dominated regime and

$$H_v = H_{v0} - \frac{m_1}{d}(d - m_2)^{\frac{1}{2}} \qquad (2.5)$$ in the grain boundary sliding regime

Where d is the grain size, m_1, m_2 and k are material parameters. Molecular dynamics simulations revealed grain-boundary sliding in nc materials [73, 74]. Stress builds up across neighboring grains during grain-boundary sliding and this stress is relieved by grain boundary migration.

2.4.3 Grain rotation/grain coalescence

During plastic deformation nano-sized grains rotate and coalesce along shear direction resulting in elongated grains by the annihilation of grain boundary. The grains rotate in such a way that their orientation becomes closer and larger elongated grains form. Softening and localization may also occur because of this mechanism. Disclinations were observed experimentally by Murayama et al. [75] in mechanically milled Fe by High Resolution TEM (HRTEM). A disclination is a line defect which is characterized by change in orientation of the crystalline lattice along its line [76]. Grains can rotate by the motion of disclinations. It was claimed that because of the large amount of stress field that is associated with these disclinations,

motion of the other deformation defects within the metal becomes very difficult, thus resulting in higher strength.

2.4.4 Grain-boundary dislocation creation and annihilation

Van Swygenhoven et al. have carried out molecular dynamics simulations and showed that the dislocation density after plastic deformation is very low in nc materials. If the grain size is lowered to nc regime, the mean free path of dislocations generated at grain boundaries becomes limited. The dislocations move freely from one end to the opposite end where they get annihilated. Hence because of the low dislocation density, there will not be significant work hardening. A dislocation emitting from a grain boundary is shown in Fig. 2.10 [3]. The shear stress, τ required to form a dislocation of radius, $r = d/2$, is

$$\tau = \frac{\alpha G b}{r} = \frac{2\alpha G b}{d} \qquad (2.6)$$

Where, G is the shear modulus, b is the Burgers vector and α, the constant, $0.5 \leq \alpha \leq 1$. For example, for copper having a grain size of 50 nm, assuming α = 0.5 and b = 0.25 nm, the shear stress, τ obtained is 242 MPa. Even though this value is slightly higher than the strength of nc Cu, it is of the same order of magnitude.

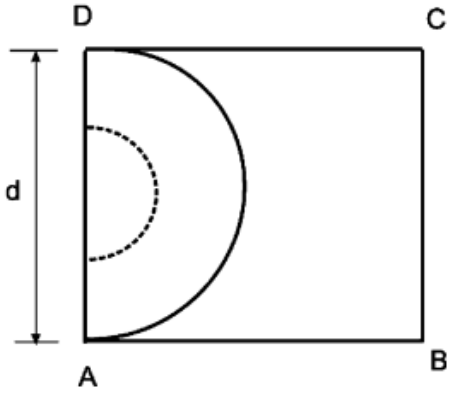

Fig. 2.10 Dislocation emitted from a grain boundary [3].

2.4.5 Twinning

Both types of twins – mechanical and growth twins influence the properties in nc materials. In case of fcc metals and/or alloys, the mechanical twinning stress depends on stacking fault energy. Higher the stacking fault energy, higher the twinning stress [77]. It is expected that at lower grain sizes twinning is more difficult. In fcc metals low temperatures and high strain rates are required to produce twinning. But, the molecular dynamics simulations predicted twinning in fcc metals during deformation [78]. Twins were experimentally observed in nc Al [79] and also in nc stainless steels [80] by TEM. Annealing twins play a significant role in optimizing strength and ductility in Cu [65]. It was stated that the twins present in the larger grains allow strain hardening which would prevent localized deformation. The growth twins also helped in achieving low electrical resistivity in nc Cu [81]. In nc Cu, the uniform elongation increased from 1% to 10% by the introduction of twins.

2.5 Strain rate sensitivity and activation volume

Strain rate sensitivity (SRS) is an important parameter which controls the ductility of materials. High values of work hardening and SRS help delay the onset of localized deformation under tensile stress, resulting in improved ductility [82]. Microcrystalline and ultra-fine crystalline pure Ni were strain rate independent, whereas nc pure Ni was strain rate dependant [83]. Nanocrystalline face-centered cubic (fcc) metals showed higher and body-centered cubic (bcc) metals showed lower SRS values than their coarse grained counterparts [84]. Wang et al. [85] suggested that the increased SRS values for fcc metals could be due to the onset of new rate-controlling deformation mechanisms. Investigations by Chinh et al. [86, 87] on ultrafine grained Al and Al-30wt.%Zn alloy, revealed the possibility of obtaining improved ductility through SPD process. They observed high SRS values for these materials and suggested that enhanced

diffusion along the grain boundaries leading to grain boundary sliding resulted in increased ductility in Al-30wt.%Zn alloy.

Considerable work has been carried out on SRS of nc metals [88-95]. Asaro and Suresh have developed mechanistic models [96] for activation volume and rate sensitivity and estimated increased SRS values and decreased activation volumes (3 – $10b^3$) for fcc metals. They summarized the literature data for Cu and Ni and depicted the same in the form of grain size vs loading rate sensitivity (Fig. 2.11) and grain size vs activation volume (Fig. 2.12) plots. In both the plots, the open diamonds indicate the data for Cu (average grain size of 500 nm) having nanotwins of 20 or 90 nm width [88]. In this case twin width is considered instead of grain size while plotting. It is clear from Fig. 2.11 that when grain size is reduced from micro to nano regime, there is a change is rate sensitivity by an order of magnitude. Decreased activation volume values are clearly evident from Fig. 2.12 [96].

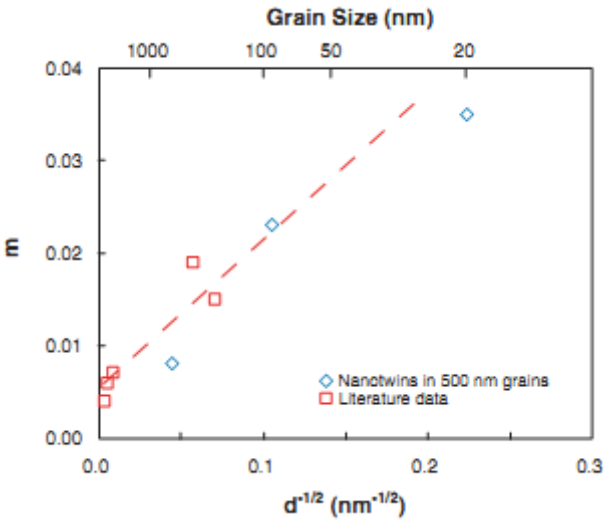

Fig. 2.11 Effect of grain size on the loading rate sensitivity, m of Cu and Ni at room temperature based on literature data. The open diamonds indicate the data for Cu (avg. grain size of 500 nm) having nanotwins of 20 or 90 nm width and twin width is considered instead of grain size while plotting [96].

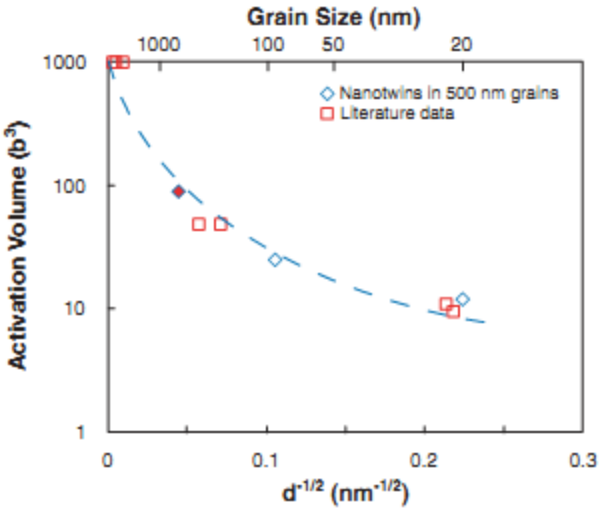

Fig. 2.12 Effect of grain size on activation volume of Cu and Ni obtained from literature data. The open diamonds indicate the data for Cu (avg. grain size of 500 nm) having nanotwins of 20 or 90 nm width and twin width is considered instead of grain size while p lotting [96].

Investigations by Gianola et al. [91] on nc Al thin films synthesized by magnetron sputtering revealed higher SRS values. They have also carried out molecular dynamics simulations and reported that the higher SRS values are associated with grain boundary deformation processes such as grain boundary sliding, migration, etc. **Error! Reference source not found.**Fig. 2.13 shows the stress vs strain rate plots of nc Al submicron thin films of 150 nm and 300 nm thickness [91].

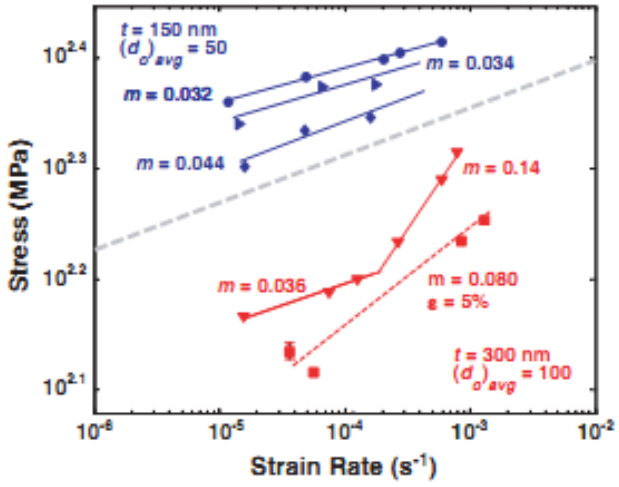

Fig. 2.13 Strain rate sensitivity of nc Al submicron thin films (150 nm and 300 nm thick). The solid lines are from strain rate jump tests where as the dashed lines are the values measured at 5% strain from the monotonic tests [91].

The solid lines in the plot are from strain rate jump tests where as the dashed lines are from the monotonic tests. They also measured the activation volume and the values obtained are 35±4 b^3 and 10-55 b^3 for 150 nm and 300 nm think nc Al films respectively.

Current focus is to study the effect of second phase on the SRS and activation volume of nc matrix. Recently, Niu et al [97], studied the SRS behavior of nanostructured two phase Cu-Cr and Cu-Zr multilayer thin films. These represent fcc-bcc and fcc-hcp combinations. In case of Cu-Cr, SRS was found to be varying between 0.022-0.031 whereas for Cu-Zr, SRS was in between 0.012-0.025. Cu-Cr had an activation volume of 11.57-15.20 b^3 whereas Cu-Zr had an activation volume in the range of 14.35-22.13 b^3.

K.A. Darling et al. have studied the mechanical properties of nanostructured Cu-Ta alloys prepared by equal channel angular extrusion (ECAE) [98]. Effect of grain size on physical activation volume for coarse grained (CG) Cu, nc Cu, Cu-1Ta (processed at 700 °C) and Cu-10Ta (processed at 900 °C) is shown in Fig. 2.14 [98]. The activation volume values measured are in the range of 10 b^3 to 100 b^3.

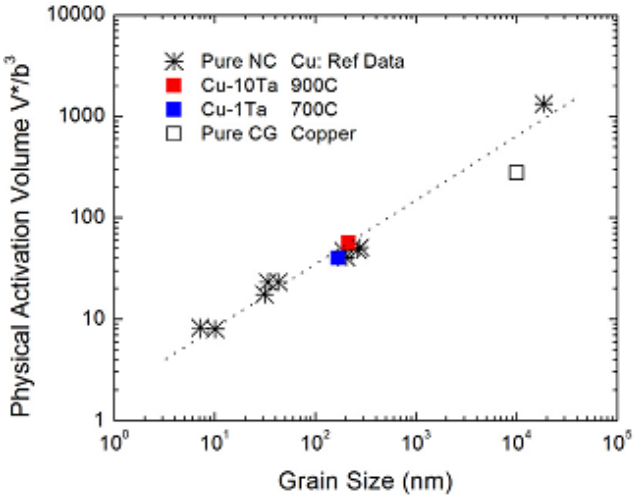

Fig. 2.14 Effect of grain size on physical activation volume for coarse grained (CG) Cu, nanocrystalline (NC) Cu, Cu-1Ta and Cu-10Ta [98].

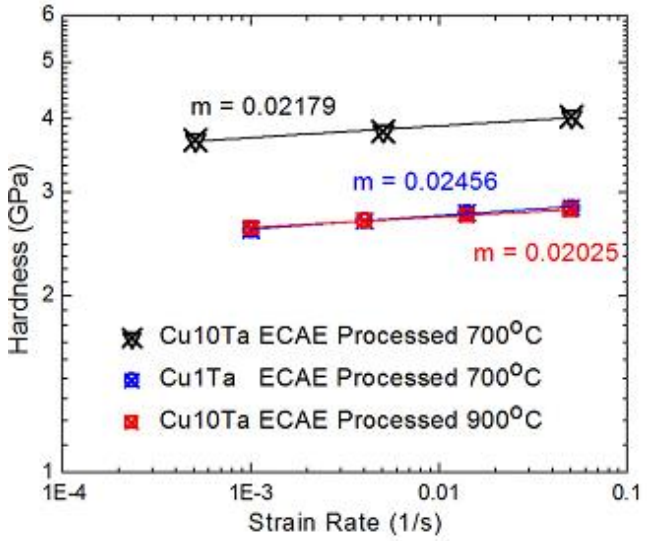

Fig. 2.15 Effect of strain rate on the hardness of Cu-1Ta and Cu-10Ta measured by nanoindentation. 'm' indicates the strain rate sensitivity [98].

Fig. 2.15 shows the effect of strain rate on the hardness of Cu-1Ta and Cu-10Ta measured by nanoindentation [98]. SRS value of ~ 0.02 was obtained. Lu et al. [99] have reported an SRS value of 0.036 for electrodeposited nc Cu with a grain size of 28 nm. Since the processing conditions are different in the above two cases, it is difficult to declare that the addition of Ta has resulted in reduction in SRS. Hence it is important to investigate the effect of various phases, in detail on the SRS and activation volume of nc multi-phase materials.

References

[1] H. Gleiter, Nanostructured materials: basic concepts and microstructure, Acta Materialia, 48 (2000) 1-29.

[2] C. Suryanarayana, C.C. Koch, Nanocrystalline materials – Current research and future directions, Hyperfine Interactions, 130 (2000) 5-44.

[3] M.A. Meyers, A. Mishra, D.J. Benson, Mechanical properties of nanocrystalline materials, Progress in Materials Science, 51 (2006) 427-556.

[4] K.S. Kumar, H. Van Swygenhoven, S. Suresh, Mechanical behavior of nanocrystalline metals and alloys, Acta Materialia, 51 (2003) 5743-5774.

[5] J.R. Weertman, Mechanical behavior of nanocrystalline metals, in: C.C. Koch (Ed.) Nanostructured materials, Noyes Publications, Norwich, NY, 2002, pp. 393–417.

[6] J.R. Weertman, D. Farkas, H. Kung, M. Mayo, R. Mitra, H. Van Swygenhoven, Structure and mechanical behavior of bulk nanocrystalline materials, MRS Bulletine, 24 (1999) 44.

[7] H. Gleiter, Nanocrystalline materials, Progress in Materials Science, 33 (1989) 223-315.

[8] C. Suryanarayana, Mechanical alloying and milling, Progress in Materials Science, 46 (2001) 1-184.

[9] H.J. Fecht, E. Hellstern, Z. Fu, W.L. Johnson, Nanocrystalline metals prepared by high-energy ball milling, Metallurgical Transactions A, 21 (1990) 2333.

[10] B. Huang, R.J. Perez, E.J. Lavernia, Grain growth of nanocrystalline Fe–Al alloys produced by cryomilling in liquid argon and nitrogen, Materials Science and Engineering: A, 255 (1998) 124-132.

[11] R.Z. Valiev, I.V. Alexandrov, Nanostructured materials from severe plastic deformation, Nanostructured Materials, 12 (1999) 35-40.

[12] R.Z. Valiev, R.K. Islamgaliev, I.V. Alexandrov, Bulk nanostructured materials from severe plastic deformation, Progress in Materials Science, 45 (2000) 103-189.

[13] A. Kojima, F. Ogiwara, A. Makino, A. Inoue, T. Masumoto, Micro structure of nanocrystalline Fe-Nb-Pr-B alloys produced by crystallization of amorphous phase, Materials Science and Engineering: A, 226–228 (1997) 520-525.

[14] M.L. Trudeau, Engineering nanocrystalline materials from amorphous precursors, Materials Science and Engineering: A, 204 (1995) 233-239.

[15] K. Kim, Plasma synthesis and characterization of nanocrystalline aluminum nitride particles by aluminum plasma jet discharge, Journal of Crystal Growth, 283 (2005) 540-546.

[16] L. Wang, J. Zhang, W. Jiang, Recent development in reactive synthesis of nanostructured bulk materials by spark plasma sintering, International Journal of Refractory Metals and Hard Materials, 39 (2013) 103-112.

[17] E. Beltowska-Lehman, A. Bigos, P. Indyka, M. Kot, Electrodeposition and characterisation of nanocrystalline Ni–Mo coatings, Surface and Coatings Technology, 211 (2012) 67-71.

[18] I. Baskaran, T.S.N. Sankara Narayanan, A. Stephen, Pulsed electrodeposition of nanocrystalline Cu–Ni alloy films and evaluation of their characteristic properties, Materials Letters, 60 (2006) 1990-1995.

[19] I. Kosta, E. Vallés, E. Gómez, M. Sarret, C. Müller, Nanocrystalline CoP coatings prepared by different electrodeposition techniques, Materials Letters, 65 (2011) 2849-2851.

[20] S.K. Mukherjee, L. Joshi, P.K. Barhai, A comparative study of nanocrystalline Cu film deposited using anodic vacuum arc and dc magnetron sputtering, Surface and Coatings Technology, 205 (2011) 4582-4595.

[21] P. Singh, D. Kaur, Room temperature growth of nanocrystalline anatase TiO2 thin films by dc magnetron sputtering, Physica B: Condensed Matter, 405 (2010) 1258-1266.

[22] S.C. Tjong, H. Chen, Nanocrystalline materials and coatings, Materials Science and Engineering: R: Reports, 45 (2004) 1-88.

[23] M.S. Hsu, M.A. Meyers, A. Berkowitz, Synthesis of nanocrystalline titanium carbide by spark erosion, Scripta Metallurgica et Materialia, 32 (1995) 805-808.

[24] C. Suryanarayana, Mechanical alloying, in: Powder Metal Technologies and Applications, ASM Handbook, ASM International, Metals Park, OH, 1998, pp. 193-215.

[25] J.S. Benjamin, Mechanical Alloying, Scientific American, 234 (1976) 40-48.

[26] J.S. Benjamin, Mechanical Alloying - A Perspective, Metal Powder Report, 45 (1990) 122-127.

[27] C. Suryanarayana, N. Al-Aqeeli, Mechanically alloyed nanocomposites, Progress in Materials Science, 58 (2013) 383-502.

[28] J. Eckert, J.C. Holzer, C.E. Krill, W.L. Johnson, Reversible grain size changes in ball-milled nanocrystalline Fe–Cu alloys, Journal of Materials Research, 7 (1992) 1751.

[29] D.L. Bourell, J.R. Groza, Consolidation of Ultrafine and Nanocrystalline Powders, in: Powder Metal Technologies and Applications, ASM Handbook, ASM International, Metals Park, OH, 1998, pp. 1176–1227.

[30] J.R. Groza, Nanocrystalline Powder Consolidation Methods, in: C.C. Koch (Ed.) Nanostructured materials: Processing, Properties and Potential Applications, Noyes publications/William Andrew Publishing, Norwich, NY, 2002, pp. 115–178.

[31] L. Melúch, Warm Compaction of Aluminium Alloy Alumix 123, in, University of Birmingham, United Kingdom, 1999.

[32] W. Liu, Q. Zhou, Nanocrystalline Aluminum by Warm-Vacuum-Compaction Method, in: Supplemental Proceedings, General Paper Selections, The Minerals, Metals and Materials Society (TMS), A John Wiley & Sons, Inc., Publication, 2011, pp. 237-244.

[33] E.Y. Gutmanas, A. Rabinkin, M. Roitberg, Cold sintering under high pressure, Scripta Metallurgica, 13 (1979) 11-15.

[34] E.Y. Gutmanas, L.I. Trusov, I. Gotman, Consolidation, microstructure and mechanical properties of nanocrystalline metal powders, Nanostructured Materials, 4 (1994) 893-901.

[35] E.Y. Gutmanas, Materials with Fine Microstructures by Advanced Powder Metallurgy, Progress in Materials Science, 34 (1990) 261-366.

[36] Tokita, Mechanism of Spark Plasma Sintering, Sumitomo coal mining company ltd., Kanagawa, Japan.

[37] D.S. Perera, M. Tokita, S. Moricca, Comparative Study of Fabrication of Silicon Nitride by Spark Plasma Sintering and Hot Isostatic Pressing, in: Proceedings of the 2nd International Meeting of Pacific Ceramic Societies, 1996.

[38] N. Tamari, T. Tanaka, K. Tanaka, M. Kawahara, M. Tokita, Effect of Spark Plasma Sintering on Densification and Mechanical Properties of Silicon Carbide, Journal of Ceramic Society of Japan, 103 (1995) 740-742.

[39] M. Mrinalini, A. Singh, S.P. Harimkar, Spark Plasma Sintering for Multi-scale Surface Engineering of Materials, JOM, 62 (2010) 65-71.

[40] H. Li, K.A. Khor, L.G. Yu, P. Cheang, Microstructure modifications and phase transformation in plasma-sprayed WC–Co coatings following post-spray spark plasma sintering, Surface and Coatings Technology, 194 (2005) 96-102.

[41] I. Manna, J. Dutta Majumdar, B. Ramesh Chandra, S. Nayak, N.B. Dahotre, Laser surface cladding of Fe–B–C, Fe–B–Si and Fe–BC–Si–Al–C on plain carbon steel, Surface and Coatings Technology, 201 (2006) 434-440.

[42] C.C. Koch, K.M. Youssef, R.O. Scattergood, Mechanical Properties of Nanocrystalline Materials Produced by in situ Consolidation Ball Millin, Materials Science Forum, 579 (2008) 15-28.

[43] P.S. Gilman, W.D. Nix, The structure and properties of aluminum alloys produced by mechanical alloying: Powder processing and resultant powder structures, Metallurgical Transactions A, 12A (1981) 813.

[44] A.M. Harris, G.B. Schaffer, N.W. Page, The Russian Doll effect by mechanical alloying, Journal of Materials Science Letters, 12 (1993) 1103.

[45] C. Suryanarayana, Nanocrystalline materials, International Materials Reviews, 40 (1995) 41-64.

[46] V. Krstic, U. Erb, G. Palumbo, Effect of porosity on Young's modulus of nanocrystalline materials, Scripta Metallurgica et Materialia, 29 (1993) 1501-1504.

[47] T.D. Shen, C.C. Koch, T.Y. Tsui, G.M. Pharr, On the elastic moduli of nanocrystalline Fe, Cu, Ni, and Cu–Ni alloys prepared by mechanical milling/alloying, Journal of Materials Research, 10 (1995) 2892-2896.

[48] Q. Wei, Z.L. Pan, X.L. Wu, B.E. Schuster, L.J. Kecskes, R.Z. Valiev, Microstructure and mechanical properties at different length scales and strain rates of nanocrystalline tantalum produced by high-pressure torsion, Acta Materialia, 59 (2011) 2423-2436.

[49] Z. Pan, Y. Li, Q. Wei, Tensile properties of nanocrystalline tantalum from molecular dynamics simulations, Acta Materialia, 56 (2008) 3470–3480.

[50] Y.Q. Liu, H.T. Cong, W. Wang, C.H. Sun, H.M. Cheng, AlN nanoparticle-reinforced nanocrystalline Al matrix composites: Fabrication and mechanical properties, Materials Science and Engineering: A, 505 (2009) 151-156.

[51] E.O. Hall, The deformation and ageing of mild stee: III Discussion of results, Proc. Phys. Soc. B, 64 (1951) 747-753.

[52] N.J. Petch, The cleavage strength of polycrystals, J. Iron and Steel Institute, (1953) 25-28.

[53] C.C. Koch, J. Narayan, The Inverse Hall-Petch Effect—Fact or Artifact?, in: MRS Proceedings, Cambridge Univ Press, 2000, pp. B5. 1.1.

[54] C. Carlton, P. Ferreira, What is behind the inverse Hall–Petch effect in nanocrystalline materials?, Acta Materialia, 55 (2007) 3749-3756.

[55] K.M. Youssef, R.O. Scattergood, K.L. Murty, C.C. Koch, Ultratough nanocrystalline copper with a narrow grain size distribution, Applied Physics Letters, 85(6) (2004) 929-931.

[56] T.D. Shen, C.C. Koch, Formation, solid solution hardening and softening of nanocrystalline solid solutions prepared by mechanical attrition, Acta Materialia, 44 (1996) 753-761.

[57] G. Sauthoff, Plastic deformation, in: J.H. Westbrook, R.L. Fleischer (Eds.) Intermetallic Compounds, Principles and Practice, John Wiley and Sons, Chichester, 1994, pp. 924-925.

[58] J. Eckert, Structure formation and mechanical behavior of two-phase nanostructured materials, in: C.C. Koch (Ed.) Nanostructured Materials: Processing, Properties and Applications, William Andrew publ., Norwich, NY, 2002, pp. 423-525.

[59] H.W. Sheng, F. Zhou, Z.Q. Hu, K. Lu, Investigation of Al-Pb nanocomposites synthesized by non-equilibrium processes, Journal of Materials Research, 13 (1998) 308-315.

[60] K.V. Rajulapati, R.O. Scattergood, K.L. Murty, G. Duscher, C.C. Koch, Effect of Pb on the mechanical properties of nanocrystalline Al, Scripta Materialia, 55 (2006) 155-158.

[61] S. Jang, Y. Purohit, D.L. Irving, C. Padgett, D. Brenner, R.O. Scattergood, Influence of Pb segregation on the deformation of nanocrystalline Al: Insights from molecular simulations, Acta Materialia, 56 (2008) 4750-4761.

[62] X. Liu, M.Q. Zeng, Y. Ma, M. Zhu, Melting behavior and the correlation of Sn distribution on hardness in a nanostructured Al–Sn alloy, Materials Science and Engineering: A, 506 (2009) 1-7.

[63] K.V. Rajulapati, R.O. Scattergood, K.L. Murty, Z. Horita, T.G. Langdon, C.C. Koch, Mechanical properties of bulk nanocrystalline aluminum-tungsten alloys, Metallurgical and Materials Transactions A, 39 (2008) 2528-2534.

[64] C.C. Koch, Optimization of strength and ductility in nanocrystalline and ultrafine grained metals, Scripta Materialia, 49 (2003) 657-662.

[65] Y. Wang, M. Chen, F. Zhou, E. Ma, High tensile ductility in a nanostructured metal, Nature, 419 (2002) 912-915.

[66] X. Zhang, H. Wang, C.C. Koch, Mechanical behavior of bulk ultrafine-grained and nanocrystalline Zn, Reviews on advanced materials science 6(2004) 53-93.

[67] K.M. Youssef, R.O. Scattergood, K.L. Murty, C.C. Koch, Nanocrystalline Al–Mg alloy with ultrahigh strength and good ductility, Scripta Materialia, 54 (2006) 251-256.

[68] K.M. Youssef, R.O. Scattergood, K.L. Murty, J.A. Horton, C.C. Koch, Ultrahigh strength and high ductility of bulk nanocrystalline copper, Applied Physics Letters, 87 (2005) 091904.

[69] M. Legros, B.R. Elliott, M.N. Rittner, J.R. Weertman, K.J. Hemker, Microsample tensile testing of nanocrystalline metals, Philosophical Magazine A, 80 (2000) 1017-1026.

[70] T.G. Nieh, J. Wadsworth, Hall-petch relation in nanocrystalline solids, Scripta Metallurgica et Materialia, 25 (1991) 955-958.

[71] H. Hahn, P. Mondal, K.A. Padmanabhan, Plastic deformation of nanocrystalline materials, Nanostructured Materials, 9 (1997) 603-606.

[72] H. Hahn, K. Padmanabhan, A model for the deformation of nanocrystalline materials, Philosophical Magazine B, 76 (1997) 559-571.

[73] H. Van Swygenhoven, P.M. Derlet, Grain-boundary sliding in nanocrystalline fcc metals, Phys. Rev. B, 64 (2001) 224105-224109.

[74] H. Van Swygenhoven, M. Spaczer, A. Caro, Microscopic description of plasticity in computer generated metallic nanophase samples: a comparison between Cu and Ni, Acta Materialia, 47 (1999) 561.

[75] M. Murayama, J.M. Howe, H. Hidaka, S. Takaki, Atomic-level observation of disclination dipoles in mechanically milled nanocrystalline Fe, Science, 295 (2002) 2433–2435.

[76] I.A. Ovid'ko, Deformation of nanostructures, Science, 295 (2002) 2386.

[77] J.A. Venables, Deformation twinning in face-centered cubic metals, Philosophical Magazine, 6 (1961) 379-396.

[78] V. Yamakov, S.R. Phillpot, D. Wolf, H. Gleiter, Deformation twinning in nanocrystalline Al by molecular-dynamics simulation, Acta Materialia, 50 (2002) 5005-5020.

[79] X.Z. Liao, F. Zhou, E.J. Lavernia, D.W. He, Y.T. Zhu, Deformation twins in nanocrystalline Al, Applied Physics Letters, 83 (2003) 5062-5064.

[80] Y.T. Zhu, X.Z. Liao, S.G. Srinivasan, Y.H. Zhao, M.I. Baskes, F. Zhou, E.J. Lavernia, Nucleation and growth of deformation twins in nanocrystalline aluminum, Applied Physics Letters, 85 (2004).

[81] L. Lu, Y. Shen, X. Chen, L. Qian, K. Lu, Ultrahigh strength and high electrical conductivity in copper, Science, 304 (2004) 422-426.

[82] Y.T. Zhu, X.Z. Liao, Nanostructured metals - Retaining ductility, Nature Materials, 3 (2004) 351–352.

[83] R. Schwaiger, B. Moser, M. Dao, N. Chollacoop, S. Suresh, Some critical experiments on the strain-rate sensitivity of nanocrystalline nickel, Acta Materialia, 51 (2003) 5159-5172.

[84] Q. Wei, S. Cheng, K.T. Ramesh, E. Ma, Effect of nanocrystalline and ultrafine grain sizes on the strain rate sensitivity and activation volume: fcc versus bcc metals, Materials Science and Engineering: A, 381 (2004) 71-79.

[85] Y.M. Wang, E. Ma, Strain hardening, strain rate sensitivity, and ductility of nanostructured metals, Materials Science and Engineering: A, 375–377 (2004) 46-52.

[86] N.Q. Chinh, T. Csanádi, J. Gubicza, R.Z. Valiev, B.B. Straumal, T.G. Langdon, The effect of grain boundary sliding and strain rate sensitivity on the ductility of ultrafine-grained materials, Materials Science Forum, 667-669 (2011) 677-682.

[87] N.Q. Chinh, T. Csanádi, T. Győri, R.Z. Valiev, B.B. Straumal, M. Kawasaki, T.G. Langdon, Strain rate sensitivity studies in an ultrafine-grained Al–30 wt.% Zn alloy using micro- and nanoindentation, Materials Science and Engineering A, 543 (2012) 117-120.

[88] L. Lu, R. Schwaiger, Z. Shan, M. Dao, K. Lu, S. Suresh, Nano-sized twins induce high rate sensitivity of flow stress in pure copper, Acta Materialia, 53 (2005) 2169-2179.

[89] Y. Shen, L. Lu, M. Dao, S. Suresh, Strain rate sensitivity of Cu with nanoscale twins, Scripta materialia, 55 (2006) 319-322.

[90] J. Chen, L. Lu, K. Lu, Hardness and strain rate sensitivity of nanocrystalline Cu, Scripta Materialia, 54 (2006) 1913-1918.

[91] D. Gianola, D. Warner, J.-F. Molinari, K. Hemker, Increased strain rate sensitivity due to stress-coupled grain growth in nanocrystalline Al, Scripta Materialia, 55 (2006) 649-652.

[92] K. Jonnalagadda, N. Karanjgaokar, I. Chasiotis, J. Chee, D. Peroulis, Strain rate sensitivity of nanocrystalline Au films at room temperature, Acta Materialia, 58 (2010) 4674-4684.

[93] V. Maier, K. Durst, J. Mueller, B. Backes, H.W. Höppel, M. Göken, Nanoindentation strain-rate jump tests for determining the local strain-rate sensitivity in nanocrystalline Ni and ultrafine-grained Al, Journal of Materials Research, 26 (2011) 1421-1430.

[94] B. Ahn, R. Mitra, A. Hodge, E.J. Lavernia, S. Nutt, Strain rate sensitivity studies of cryomilled Al alloy performed by nanoindentation, in: Materials Science Forum, Trans Tech Publ, 2008, pp. 221-226.

[95] I.-C. Choi, Y.-J. Kim, Y.M. Wang, U. Ramamurty, J.-i. Jang, Nanoindentation behavior of nanotwinned Cu: Influence of indenter angle on hardness, strain rate sensitivity and activation volume, Acta Materialia, 61 (2013) 7313-7323.

[96] R.J. Asaro, S. Suresh, Mechanistic models for the activation volume and rate sensitivity in metals with nanocrystalline grains and nano-scale twins, Acta Materialia, 53 (2005) 3369-3382.

[97] J.J. Niu, J.Y. Zhang, G. Liu, P. Zhang, S.Y. Lei, G.J. Zhang, J. Sun, Size-dependent deformation mechanisms and strain-rate sensitivity in nanostructured Cu/X (X=Cr, Zr) multilayer films, Acta Materialia, 60 (2012) 3677-3689.

[98] K. Darling, M. Tschopp, R. Guduru, W. Yin, Q. Wei, L. Kecskes, Microstructure and mechanical properties of bulk nanostructured Cu–Ta alloys consolidated by equal channel angular extrusion, Acta Materialia, 76 (2014) 168-185.

[99] L. Lu, S.X. Li, K. Lu, An abnormal strain rate effect on tensile behavior in nanocrystalline copper, Scripta Materialia, 45 (2001) 1163–1169.

Chapter 3 – Experimental Details

Nanocrystalline (nc) alloy powders are synthesized using high energy ball milling at room temperature. Structural characterization of the alloy powders has been carried out by X-ray diffraction (XRD) and transmission electron microscopy (TEM). The powders are consolidated into bulk samples by high pressure compaction (at room temperature) and/or spark plasma sintering (SPS). Thin electron transparent samples were prepared using ion-beam milling and examined using a TEM. The bulk samples were metallographically polished to a mirror-like surface and hardness measurements were carried out using microhardness tester (Omnitech-MVH-Sauto with 10 sec dwell time) and a depth sensing nanoindenter (Hysitron's TI950 Triboindenter). The following sections include details on the initial materials used along with their basic properties, the processing parameters used during synthesis of nc materials and the structural and mechanical characterization that has been carried out on the bulk samples.

3.1 Materials used

The initial materials used are aluminium (Al), lead (Pb), tungsten (W) and bismuth (Bi) powders. The details (purity, mesh size and make) of these powders are given in Table 3.1.

Table 3.1 Details of initial powders used.

	Aluminium (Al)	Lead (Pb)	Tungsten (W)	Bismuth (Bi)
Make	S-D Fine Chemicals Ltd	Alfa Aesar	Alfa-Aesar	Alfa-Aesar
Purity	99.0%	99.9%	99.9%	99.9%
Mesh size	+200	-200	-200	-200

The basic properties of these metal powders in general are listed in Table 3.2. Al and its alloys have high strength-to-weight ratio and are extensively used as structural materials. The focus of the current investigation is to study the mechanical behavior of nc alloys/composites having the grain size of both the phases in nano-scale. Aluminium was chosen as the matrix element and Pb, W and Bi were chosen as second phase materials. Pb and Bi are softer when compared to Al and both the elements are immiscible in Al. The equilibrium binary phase diagrams of Al-Pb and Al-Bi systems [1] are shown in Fig. 3.1 and Fig. 3.2 respectively. Tungsten is a harder phase having BCC crystal structure and forms some intermetallic compounds with Al under equilibrium conditions [1] as shown in Fig. 3.3.

Table 3.2 The basic elemental properties of Al, Pb, W and Bi.

Property	Aluminium (Al)	Lead (Pb)	Tungsten (W)	Bismuth (Bi)
Atomic number (Z)	13	82	74	83
Atomic mass (A)	27	207.21	183.84	208.98
Atomic radius (Å)	1.43	1.75	1.37	156 pm
Crystal structure	FCC	FCC	BCC	Rhombohedral
Lattice parameter (Å)	4.0494	4.9506	3.1648	4.75
Density (g/cc)	2.7	11.34	19.3	9.78
Melting point (K)	933	600	3643	544.7
Hardness (MPa)	147	49	3038	94.2
Poisson's ratio	0.33	0.42	0.28	0.33

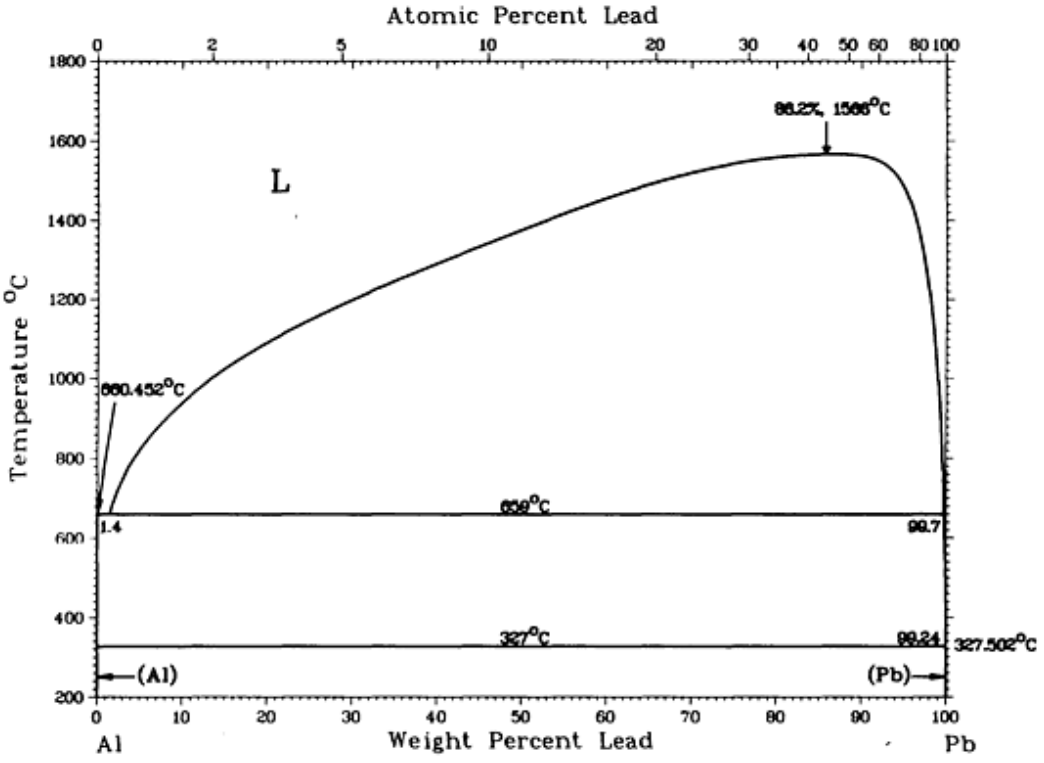

Fig. 3.1 Equilibrium phase diagram of Al-Pb system [1].

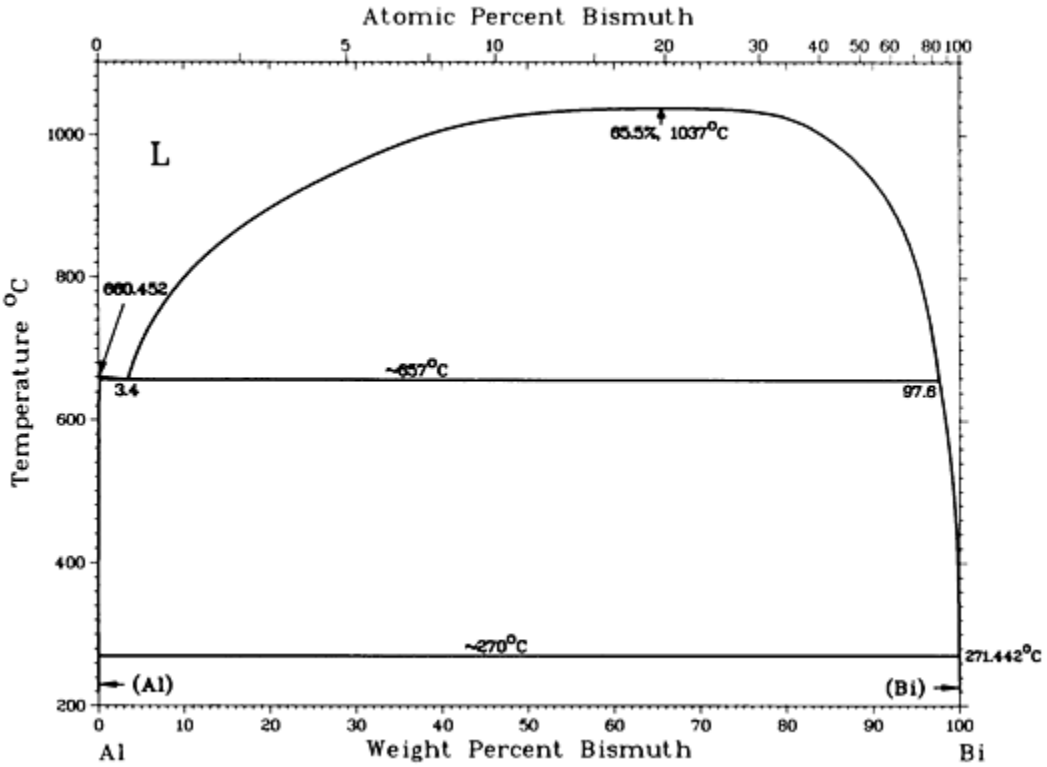

Fig. 3.2 Equilibrium phase diagram of Al-Bi system [1].

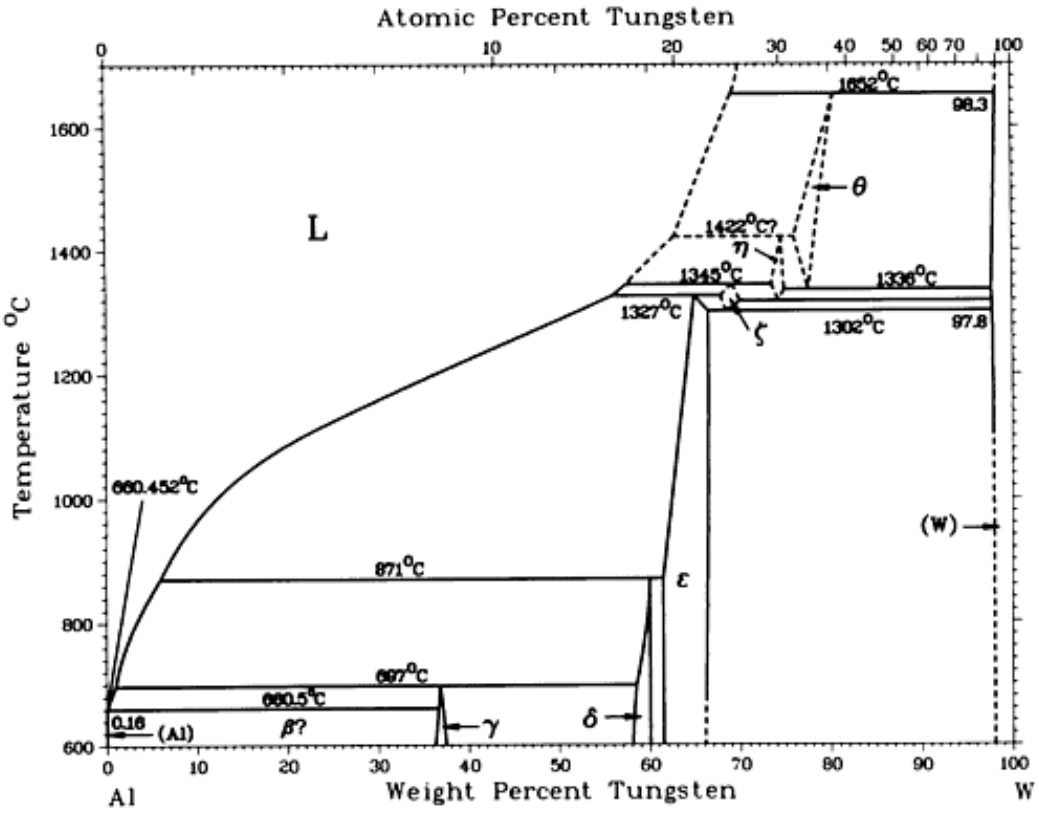

Fig. 3.3 Equilibrium phase diagram of Al-W system [1].

3.2 Processing of nanocrystalline materials

3.2.1 High energy ball milling

The process parameters used during high energy ball milling are listed in the following table.

Table 3.3 Process parameters used during high energy ball milling.

Type of mill	SPEX 8000 Shaker mill
Milling media	Hardened steel
Ball to powder weight ratio	5:1
Process controlling agent	Stearic acid
Temperature	Room temperature
Atmosphere	Argon

3.2.2 High pressure compaction

The process parameters used during high pressure compaction are listed in the following table.

Table 3.4 Process parameters used during high pressure compaction.

Type of press	Uni-axial press
Pressure applied	1.5 GPa
Temperature	Room temperature
Atmosphere	Air
Holding time	1 hour
Die set material	Hardened steel

3.2.3 Spark plasma sintering

The process parameters used during spark plasma sintering are listed in the following table.

Table 3.5 Process parameters used during spark plasma sintering.

Type of press	DR SINTER (SPS)
Pressure applied	70 MPa
Temperature	573 K for Al-Pb and 523 K for Al-Bi
Atmosphere	Vacuum
Holding time	5 min
Die set material	Graphite

3.3 Structural characterization

Structural characterization of the milled powders as well as the sintered samples has been carried out by XRD and TEM. Sintered samples were cut into smaller discs and thin electron-

transparent samples (3 mm diameter) were prepared by ion-beam milling using Gatan's precision ion polishing system (PIPS) for TEM observations. Differential scanning calorimetry (DSC) was also used to characterize the milled Al-Bi alloy powders to check if there is any non-equilibrium phase formation or change in melting point of Bi.

3.3.1 X-ray diffraction (XRD)

X-ray diffraction is a characterization technique used to identify various crystalline phases present in the material, to determine crystal structur, lattice parameter and to estimate cryatallite size. A collimated beam of X-rays having wavelength 0.5-2 A^0, is made to incident on a specimen, which is diffracted by the crystalline phases in the material. According to Bragg's law [2],

$$n\lambda = 2d \sin\theta \qquad (3.1)$$

where d is the interplanar spacing; n is the order of reflection; λ is the wavelength of the incident X- ray beam. Diffracted X-ray intensity is measured as a function of the diffraction angle 2θ.

The lattice parameter, a is calculated using the following equation [2] for a material with a cubic crystal structure:

$$a = d\sqrt{h^2 + k^2 + l^2} \qquad (3.2)$$

where d is the inter planar spacing measured using Bragg's law and h, k, l are the indices of the plane. There is an error involved in measuring $\sin\theta$, and the error decreases with increasing value of θ. The error in the value of measured d is zero for a value of $\theta = 90^0$. Hence the following Nelson-Riley extrapolation function [3] is used to calculate the precise lattice parameter value:

$$\frac{\cos^2\theta}{\sin\theta} + \frac{\cos^2\theta}{\theta} \qquad (3.3)$$

When the lattice parameter is plotted against the above function, a straight line is obtained and the lattice parameter corresponding to the value of 0 for the above function ($\theta = 90^0$) gives the precise lattice parameter. Crystallite size is estimated from the broadening of XRD peaks using the Scherrer equation [3]:

$$B_{Crysta\,llite} = \frac{k\lambda}{L\,\cos\theta} \qquad (3.4)$$

where λ is the wavelength of the X-ray beam, k is a constant, L is the average crystallite size and θ is the Bragg angle. The constant k is usually taken as 0.9.

3.3.2 Transmission electron microscopy (TEM)

Transmission electron microscopy (TEM) is a powerful technique to characterize materials at nano-scale for structural details. High resolution of TEM is due to the short wavelength of electron used. When an electron beam is passed though a material, the material interacts with the beam and scatters the electrons in different ways. Part of the beam is reflected, part of the beam is absorbed and part of the beam is transmitted. The electron scattering can be *elastic* that involves no loss of energy or *inelastic* that results in loss of energy.

3.3.2.1 Imaging in TEM

Contrast is defined as the difference in brightness between two adjacent points in an image. In light microscopy, contrast is due to difference in absorption of light at different regions of the sample. In TEM, image contrast is mainly due to electrons that are scattered from the transmitted beam. Electron scattering occurs through mass thickness contrast, diffraction contrast and phase contrast [4]. Mass-thickness contrast and diffraction contrast are due to amplitude contrast which is due to the change in amplitude of the transmitted electrons. Bright field (BF) and dark field

(DF) images are obtained by selecting the direct beam and diffracted beam respectively using an objective aperture.

3.3.2.1.1 Mass-thickness contrast

When the electrons interact with the atomic nucleus, the amount of electron scattering at any point depends on the mass and thickness of the sample at that point. The contrast, C is defined as follows [5]

$$C = \frac{I_o - I_t}{I_o} \qquad (3.5)$$

where I_o and I_t are the intensities of the primary beam and the transmitted beam respectively. This is the main contrast mechanism in non-crystalline materials like polymers and biological materials.

3.3.2.1.2 Diffraction contrast

This is the main image formation mechanism in crystalline materials. Similar to X-ray diffraction, Bragg's law is applicable to electron diffraction as well. Bright-field and dark-field images are generated using diffraction contrast. When the transmitted beam alone is allowed to pass through the objective aperture, bright-field is obtained. The dark-field image is obtained when the diffracted beam passes through the objective aperture. To obtain the dark-field images, different diffraction spots/rings (corresponding to different set of planes) are selected from a selected area diffraction pattern. The interplanar spacing, d can be measured using the following relationship [5]

$$\lambda L = rd \qquad (3.6)$$

Where L is the camera length, λ is the wavelength of electron beam and r is the radius of the diffraction ring.

3.3.2.1.3 Phase contrast

Phase contrast is obtained due to the phase difference in electron waves which gives highest resolution in TEM imaging. This is also termed as high-resolution transmission electron microscopy (HRTEM). Both the transmitted beam and the diffracted beam are involved in image formation. When multiple diffracted beams are involved in TEM image formation, a clear lattice image can be produced.

3.3.2.2 High-resolution imaging

High-resolution imaging is a powerful technique that provides quantitative information about the atomic arrangement in a material and especially for understanding details of nanoscale materials. HRTEM enables imaging lattice defects, dislocations, grain boundaries, and interfaces [4, 6, 7]. The contrast is mainly due to the phase shifts of the electron waves as they pass through the specimen. HRTEM images are formed from coherent elastically-scattered electrons. Fast Fourier Transform (FFT) analysis is used to analyze the atomic structure in the obtained image.

3.3.2.3 Z-contrast imaging

In Z-contrast imaging or "high-angle annular dark-field" (HAADF) imaging, images are formed from incoherent elastically-scattered electrons. HAADF images are obtained in scanning transmission electron microscopy (STEM) mode in which the sample area is scanned by a high-intensity electron probe. Annular dark-field detector is used to capture high-angle electrically scattered electrons. Intensity of scattering, I, scales with the square of atomic number, Z i.e. I is directly proportional to Z^2 [4].

3.3.3 Differential scanning calorimetry (DSC)

In differential scanning calorimetry (DSC), the difference in the heat required to increase the temperature of the sample with respect to that of an inert reference is measured and is plotted as a function of temperature. The sample and reference are heated at constant rate and are maintained at the same temperature during the experiment. Generally, the temperature of the sample holder increases linearly with time. Using DSC, melting temperature, crystallization temperature, glass transition temperature, phase changes and product stability can be measured [8] and all these measurements can be done under various atmospheres. When the sample undergoes physical transformation, for example phase transition, there will be change in heat flow between the sample and the reference to maintain both of them at the same temperature. This difference in heat flow depends on whether the process is exothermic or endothermic. In an endothermic reaction, energy is absorbed in the form of heat, whereas, in an exothermic reaction energy is released in the form of heat.

3.4 Mechanical characterization

Mechanical characterization of the bulk samples was carried out using microhardness tester and nanoindentation. Microhardness measurements were carried out using Vickers microindenter (Omnitech-MVH-Sauto with 10 sec dwell time) at various loads ranging from 25-100 g. Each datum point is an average of 10 indentations performed under identical conditions. The mechanical properties were also measured using a depth sensing nanoindenter (Hysitron's TI950 Triboindenter) coupled with Scanning Probe Microscopy (SPM).

3.4.1 Microhardness testing

In Vickers hardness test a square-based diamond pyramid indenter is used. The included angle between opposite faces of the pyramid is 136^0. Vickers hardness number (VHN) is

obtained by dividing the applied load with surface area of the indentation. The lengths of the diagonals of the indent are measured microscopically from which the area is calculated. The VHN may be determined from the following equation [9]:

$$VHN = \frac{2P \sin\left(\frac{136}{2}\right)}{d^2} = \frac{1.8544\,P}{d^2} \qquad (3.7)$$

where P is the load applied in kgf and d is the mean diagonal (in mm) of the impression made after indentation. The hardness value can be obtained in GPa by taking the value of P in Newtons and the value of d in meters and substituting them in the above equation. Usually the hardness testers are designed to apply the load smoothly without any impact.

3.4.2 Nanoindentation

Working principle of a nanoindenter is shown in Fig. 3.4. Hardness and elastic modulus values are measured from the load-displacement data obtained from load-unload cycle of nanoindentation (Fig. 3.5). Hardness, H is estimated from the peak load applied, P_{max} and the contact area under load, A as per the following equation

$$H = \frac{P_{max}}{A} \qquad (3.8)$$

The contact area is a function of contact depth, h_c of the indenter and for a Berkovich indenter, it is given as per the following equation

$$A = C_0\, h_c^2 + C_1\, h_c^1 + C_2\, h_c^{1/2} + C_3\, h_c^{1/4} + \cdots + C_8\, h_c^{1/128} \qquad (3.9)$$

Where, C_0 = 24.56, C_1 = 1.6991E+4, C_2 = -1.1537E+6, C_3 = 1.1977E+7, C_4 = -3.0602+7 and C_5 = 1.9918E+7. In most of the cases it can be simplified as $A = 24.56\, h_c^2$.

Elastic modulus values are calculated from the reduced modulus values obtained from nanoindentation data using the following formula [10, 11]

$$\frac{1}{E_r} = \frac{(1-\nu_i^2)}{E_i} + \frac{(1-\nu_s^2)}{E_s} \qquad (3.10)$$

where, E_r is the reduced modulus, E_i and ν_i are the Young's modulus and Poisson's ratio of the diamond indenter which are considered as 1140 GPa and 0.07 respectively. E_s is the Young's modulus of the sample and ν_s is the Poisson's ratio of the sample, 0.33.

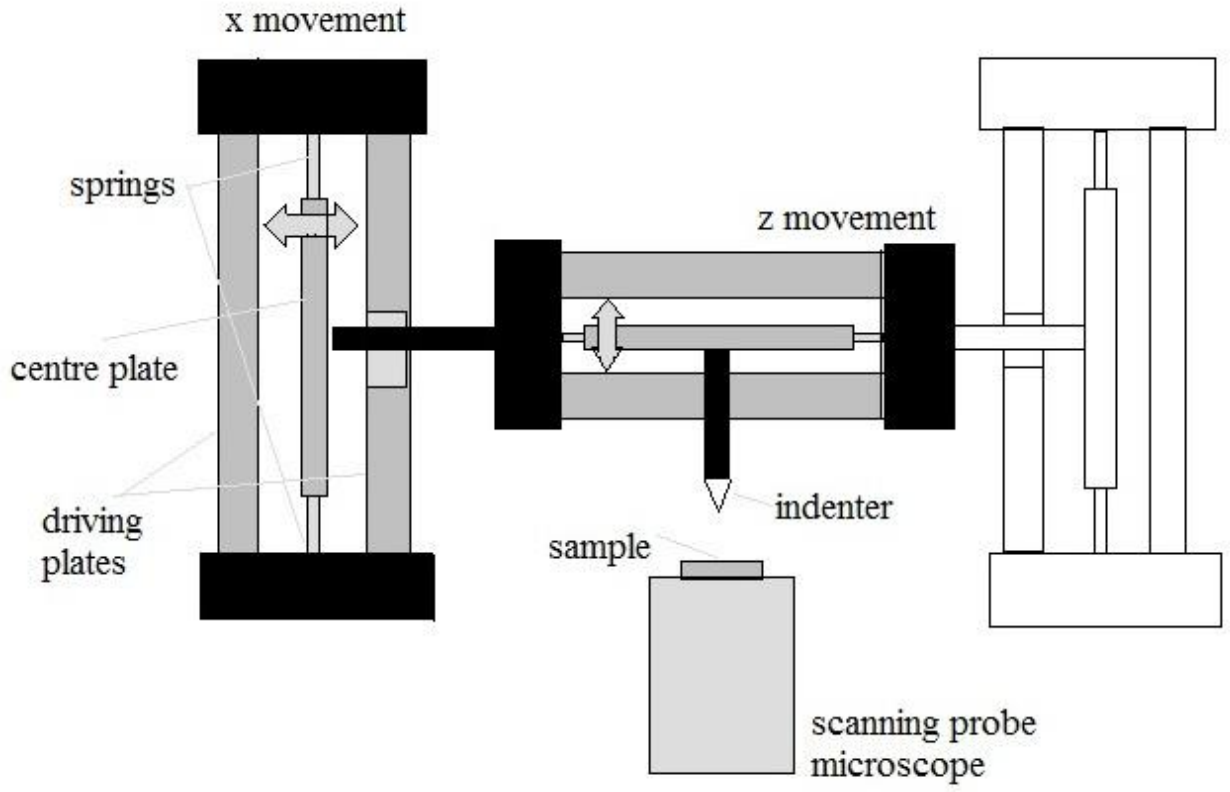

Fig. 3.4 Schematic showing the working principle of a nanoindenter.

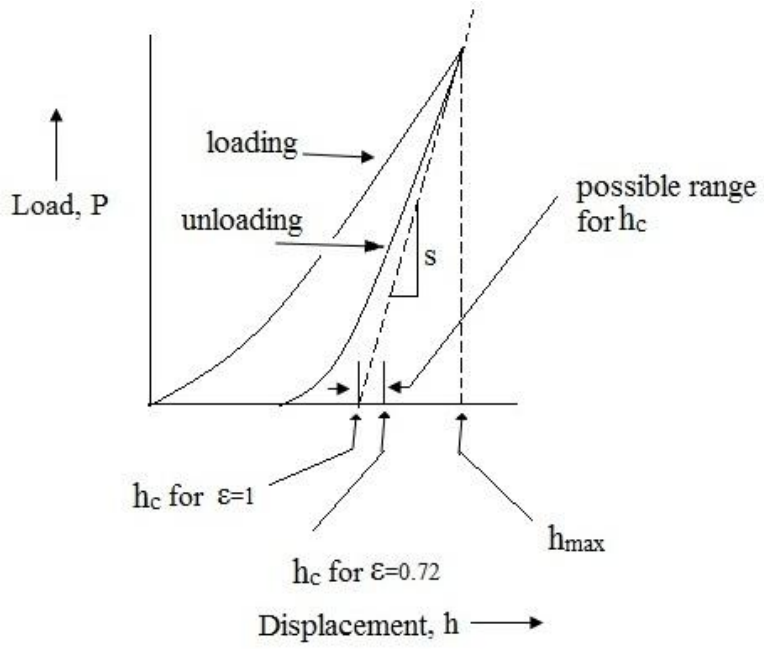

Fig. 3.5 Schematic showing the load vs displacement plot.

The flow stress of a material is dependent on the strain rate. Strain rate sensitivity or the strain-rate exponent, m can be measured from the variation of flow stress, σ with strain rate, $\dot{\varepsilon}$ in uniaxial tension as per the following equation [12]

$$m = \frac{\partial \ln \sigma}{\partial \ln \dot{\varepsilon}} \qquad (3.11)$$

The flow stress of a material is related to the strain rate by the following power law equation [12]

$$\sigma = \sigma_0 \left(\frac{\dot{\varepsilon}}{\dot{\varepsilon}_0}\right)^m \qquad (3.12)$$

In the current study, SRS is measured from the slope of yield strength vs strain rate plots on logarithmic scale obtained from nanoindentation data for different peak forces by varying the loading rates. Yield strength is calculated based on Tabor's law [13], $\sigma = H/3$, where σ is the yield strength and H being the hardness value obtained from nanoindentation data. The peak force divided by the loading rate is considered as the effective strain rate. In order to study the

distribution of dispersions in Al matrix, modulus mapping studies have been carried out on Al-Pb-W alloy using a nano indenter. During modulus mapping a dynamic force is applied on the sample while the sample surface is scanned by a probe in raster mode.

References

[1] ASM Handbook, Volume 3, Alloy phase diagrams, ASM International, 1992.

[2] B.D. Cullity, Elements of X-ray Diffraction, Addison-Wesley Publishing Company, Inc., Reading, Massachusetts, 1956.

[3] C. Suryanarayana, M. Grant Norton, X-Ray Diffraction A Practical Approach, Plenum Press, New York, 1998.

[4] B. David Williams, C. Barry Carter, Transmission Electron Microscopy A Textbook for Materials Science, Springer, New York, 2009.

[5] Y. Leng, Materials Characterization - Introduction to Microscopic and Spectroscopic Methods, John Wiley & Sons (Asia) Pte Ltd., Singapore, 2008.

[6] B. Fultz, J.M. Howe, Transmission Electron Microscopy and Diffractometry of Materials, Third Edition ed., Springer-Verlag Heidelberg, 2007.

[7] A. Leonid, Bendersky, W.G. Frank, Electron Diffraction Using Transmission Electron Microscopy, Journal of Research of the National Institute of Standards and Technology, 106 (2001) 997–1012.

[8] G. Höhne, W. Hemminger, H.-J. Flammersheim, Differential Scanning Calorimetry: An Introduction for Practitioners, Springer-Verlag, 1996.

[9] ASM Handbook, Volume 8, Mechanical Testing and Evaluation, 2000.

[10] W.C. Oliver, G.M. Pharr, An Improved Technique for Determining Hardness and Elastic Moduli using Load and Displacement Sensing Indentation Experiments, Journal of Materials Research, 7 (1992) 1564-1583.

[11] W.C. Oliver, G.M. Pharr, Measurement of hardness and elastic modulus by instrumented indentation: Advances in understanding and refinements to methodology, Journal of materials research, 19 (2004) 3-20.

[12] Y. Wei, A.F. Bower, H. Gao, Enhanced strain-rate sensitivity in fcc nanocrystals due to grain-boundary diffusion and sliding, Acta Materialia, 56 (2008) 1741-1752.

[13] D. Tabor, The hardness and strength of metals, Journal Institute of Metals, 79 (1951) 1-18.

Chapter 4 - Strain Rate Sensitivity of Nanocrystalline Al

4.1 Introduction

Aluminium and its alloys have extensive applications as structural materials mainly due to their high strength-to-weight ratio. It is well known that grain refinement is one of the major strengthening mechanisms used for improving the strength of materials through Hall-Petch strengthening [1]. In recent years there has been a growing interest in synthesis and processing of nanocrystalline/nanostructured materials (average grain sizes < 100 nm) due to their improved mechanical and physical properties [2-15]. Nanocrystalline (nc) metal powders can be produced by several processing routes and ball milling is being used in producing these powders in bulk quantities [6]. Retaining the nano structure is a big challenge while consolidating nc powders. Densification of nc materials occurs at relatively lower temperatures when compared to microcrystalline materials and the activation energies for sintering are also observed to be much lower for these materials [16, 17]. Generally, nc powders tend to sinter at temperatures of 0.2 - 0.4 T_m as compared to 0.5 - 0.8 T_m for conventional microcrystalline powders [16, 17]. Various manufacturing processes like sinter forging, hot isostatic pressing and cold sintering (high-pressure consolidation) are already in use for consolidation of these materials. Pressure levels of above 1 GPa are often used in pressure-assisted consolidation methods to overcome the large interfacial friction effects [16]. Hot processing methods might result in considerable coarsening of nc structure. Fine grain structure can be retained by sintering the powders at lower temperatures and high applied pressures. Warm compaction method has been in use to improve the density of Al and its alloys [18, 19]. Under high applied pressures, the oxide layers formed

on the powder particles can be broken leading to further densification. Densification occurs due to plastic deformation and surface diffusion at particle interfaces.

Most of the investigations on nanostructured bulk materials resulted in high strength, but low ductility [3]. The low ductility was attributed to the presence of pores and other artifacts. Koch [13] suggested that material with the ability for strain hardening is essential to prevent the premature failure in nc materials and for this reason the material has to be artifact-free. He indicated that bi-modal grain size distribution with few larger grains helps in sustaining the dislocation activity which is needed for strain hardening. Strain rate sensitivity (SRS) is also an important parameter which controls the ductility of materials. High values of work hardening and SRS help delay the onset of localized deformation under tensile stress, resulting in improved ductility [20]. Experimental data available on the strain rate sensitive mechanical properties of nc metals and alloys is very limited. Such experiments are useful in revealing deformation mechanisms in these materials, which are mostly associated with grain boundary processes. Some of the results on nanostructured copper processed by equal channel angular pressing (ECAP) - a severe plastic deformation (SPD) technique, showed longer uniform deformation with increasing number of ECAP cycles indicating improved ductility due to large processing strain [20]. The reason for increased ductility was also attributed to the presence of sharp, narrow grain boundaries. Schwaiger et al. [21] presented their work on SRS of electrodeposited nc nickel. They observed that microcrystalline and ultra-fine crystalline pure Ni was strain rate independent, whereas nc pure Ni was strain rate dependant. Both depth-sensing indentation and tensile test results showed increased hardness with increase in strain rate indicating positive SRS. Based on the experimental results published by Wei et al. [22], it has been observed that nc face-centered cubic (fcc) metals show higher and body-centered cubic (bcc) metals show lower SRS

values than their coarse grained counterparts. Wang et al. [23] suggested that the increased SRS values for fcc metals could be due to the onset of new rate-controlling deformation mechanisms. Results obtained by May et al. [24] on SPD Al (99.5% pure) indicated positive SRS value for ultrafine-grained Al, and it was higher than the value obtained for coarse grained counterpart. Experimental studies by Lu et al. [25] on fracture behavior of nc electrodeposited Cu, indicated increased strain-to-failure with increase in strain rate. Thus, in general, it may be concluded that nc materials exhibit rate sensitivity.

The present work involves understanding the SRS behavior of nc Al at room temperature using depth-sensing nanoindentation technique by indenting the sample at different loading rates and different depths. Fabricating bulk nc materials (with an average grain size around 40 nm), which can be tested for mechanical properties (strength, ductility) as per ASTM testing procedures, is a challenging task as on today. In the current investigation the measurement of both strength (from hardness) and qualitative indication on ductility (from SRS sensitivity measurements) on nc Al sample are realized using nanoindentation technique.

4.2 Materials and methods

Nanocrystalline Al powder was synthesized using high energy ball milling at room temperature. Al powder (99.0% purity, S-D Fine Chemicals Limited) of +200 mesh particle size was used as initial powder for milling. Al powder was loaded into the high energy ball mill (Spex 8000D Mixer/Mill) and milled for 50 hours. Hardened steel was used as milling media (vials and balls). Milling was performed under argon atmosphere to avoid oxidation of the powder particles during milling. The ball to powder weight ratio was maintained as 5:1 and 1.5 wt.% stearic acid was added as process controlling agent to avoid agglomeration of powder particles during milling operation. The milled powder was consolidated into 10 mm diameter

disks by applying a uni-axial pressure of 1.5 GPa at room temperature for 1 hour. The densities of the compacted disks were measured using Archimedes principle.

The compacted disc was subjected to elemental analysis to find out the presence of Carbon, Nitrogen, Hydrogen and Sulfur using combustion technique. Oxygen present in the compacted product was measured using inert gas fusion technique. Structural characterization was carried out by X-ray diffraction (XRD) and transmission electron microscopy (TEM). XRD analysis of the powdered sample as well as the bulk sample was carried out by BRUKER D8 ADVANCE X-ray diffractometer using Cu K-α radiation of wavelength 1.54056 Å with a scan speed of 3 sec/step, a step size being 0.05°. Scanning Electron Microscopy (SEM) characterization was performed using HITACHI S3400N SEM coupled with energy dispersive spectroscopy (EDS). TEM analysis was done using Technai FEI G2 S-Twin instrument at an applied voltage of 200 keV. Microhardness measurements were carried out using Vickers microindenter (Omnitech-MVH-Sauto with 10 sec dwell time) at various loads ranging from 25-100 gm. Each datum point is an average of 10 indentations performed under identical conditions. The mechanical properties were also measured using a depth sensing nanoindenter (Hysitron's TI950 Triboindenter) coupled with scanning probe microscopy (SPM).

4.3 Results and discussion

The X-ray diffractograms of ball milled powder and cold compacted nc Al are shown in Fig. 4.1. Precise lattice parameter values calculated for these samples using Nelson-Riley extrapolation function are 4.0481 ± 0.0005 Å and 4.0479 ± 0.0005 Å respectively, which are in good agreement with the standard literature value of 4.0495 Å. Grain size value of bulk nc Al measured using Scherrer formula [26] from X-ray line broadening data after accounting for instrumental broadening is 40 ± 10 nm. Fig. 4.2 (a) and (b) represent the bright-field and dark-

field transmission electron micrographs obtained from Al showing the nc structure. The corresponding diffraction pattern of the micrograph (as in Fig. 4.2 (b) inset) showed concentric rings corresponding to Al.

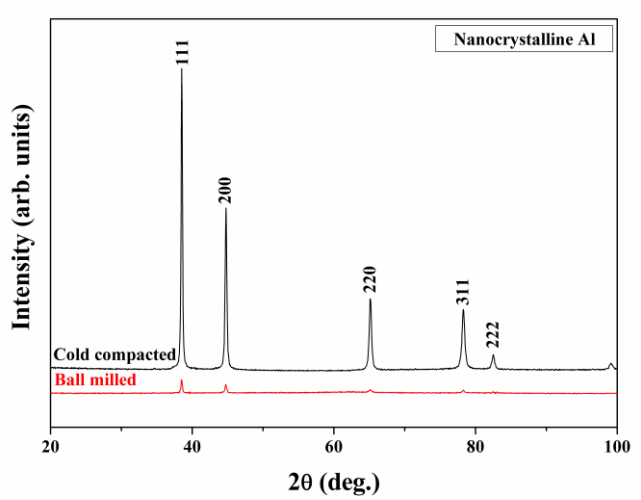

Fig. 4.1 X-ray diffractograms of ball milled nanocrystalline Al powder and cold compacted nanocrystalline Al.

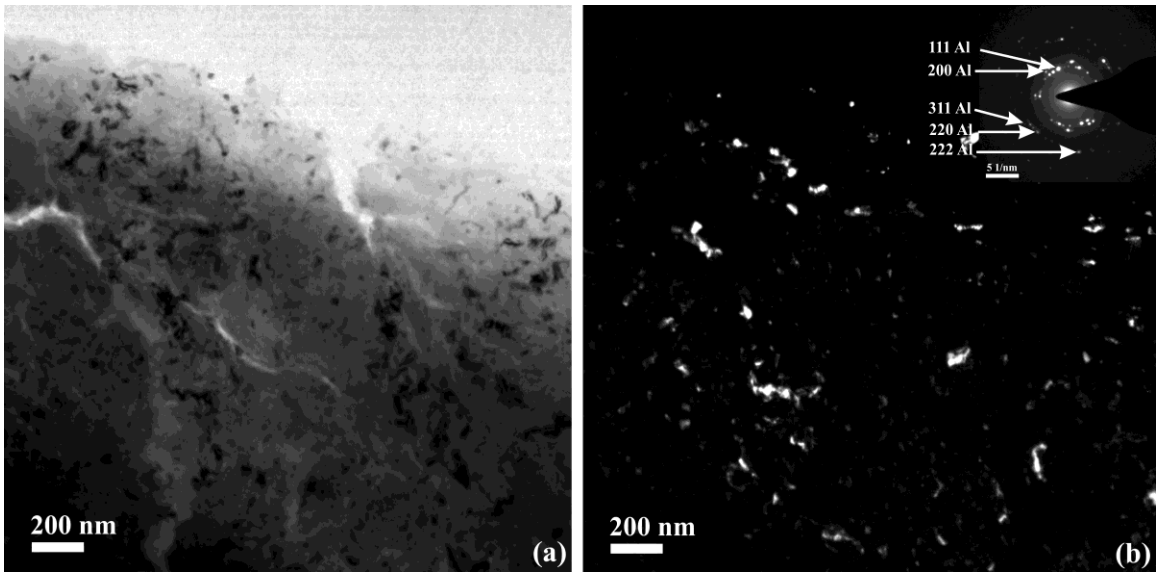

Fig. 4.2 (a) Bright field and (b) dark field transmission electron micrographs (inset shows the corresponding diffraction pattern) of Al showing nanocrystalline structure.

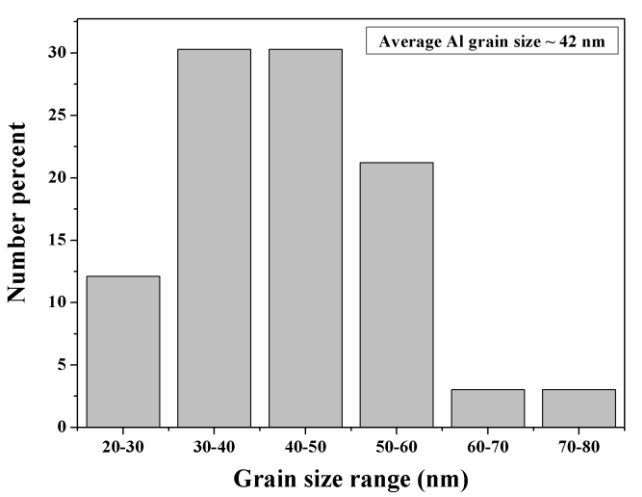

Fig. 4.3 The grain size distribution plot of nanocrystalline Al having an average Al grain size of ~ 42 nm.

Fig. 4.3 indicates the Al grain size distribution obtained from the dark field transmission electron micrographs having an average Al grain size of ~ 42 (± 9) nm which is closely matching with the value obtained from XRD data. Al grains are of irregular shape and the grain size distribution is nearly uniform with grain size varying between 20 to 80 nm.

The room temperature compacted powders resulted in bulk samples having ~ 98 % of theoretical density. The as-prepared bulk nc Al samples of different thicknesses are shown in Fig. 4.4. The compaction has been carried out under normal air atmosphere. High density was achieved at room temperature by applying a uni-axial pressure of 1.5 GPa which was maintained for 1 hour. Liu et al. presented their work on warm-vacuum-compaction of nanocrystalline Al powders synthesized by flow levitation technology [19]. They studied the effect of pressure and temperature on the density of Al compacts. The samples compacted at 323 K by applying a pressure of 1.5 GPa showed 98.26% density. They also emphasized the possibility of less vacancy defects and release of internal stresses in the compacts subjected to constant-pressure for longer time. They obtained an average microhardness of 1.65 GPa.

Fig. 4.4 Cold compacted bulk nanocrystalline Al samples.

In the present work, the powder particles obtained through high energy ball milling are in micron size, which are nanocrystalline. Therefore here, the densification seems to be occurring due to the rearrangement of micron size particles leading to large pore collapse under high applied pressure for prolonged time. High pressures also result in breakage of the oxide layer formed if any on the surface of powder particles leading to better inter-particle bonding. Hence, high pressure compaction at room temperature could be a good method to achieve good density in certain nc materials which would result in realization of the original strength and inherent ductility of the material.

The variation of microhardness with the applied load is shown in Fig. 4.5 which indicates the decreasing trend in hardness with increasing load. Each datum point in the plot was taken from an average of 10 readings. The hardness data obtained from nanoindentation is shown in Fig. 4.6 representing the variation of hardness with contact depth for various strain rates. The loading rate divided by the peak force applied is considered as strain rate. The peak forces corresponding to the contact depth values are also depicted in the figure. Each datum point in the plots was taken from an average of 49 indents. Higher hardness values are obtained for an applied peak force of

1000 µN which resulted in a contact depth of ~ 120 nm. As the applied force is increased, the contact depth increased and hardness values decreased indicating the indentation size effect. The hardness values increased with increasing strain rate and a maximum hardness value of 2.18 ± 0.17 GPa was obtained for a peak force of 1000 µN and a strain rate of 10^0 (=1) s^{-1}.

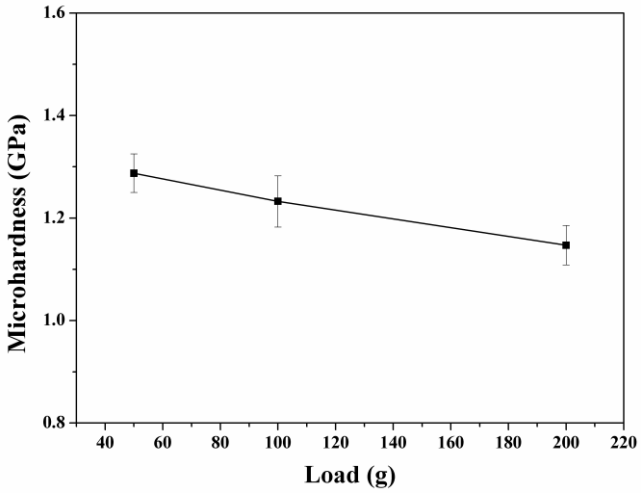

Fig. 4.5 Variation of microhardness with applied load for cold compacted nanocrystalline Al showing the decreasing trend in hardness with increasing load.

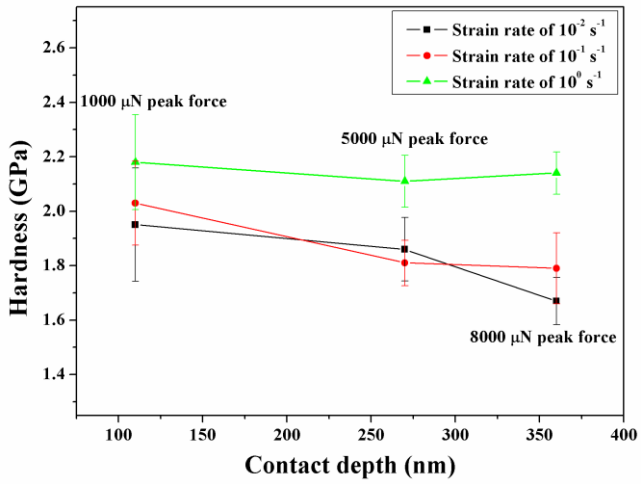

Fig. 4.6 Variation of hardness with contact depth of cold compacted nanocrystalline Al obtained from nanoindentation data for various strain rate values.

Elastic modulus values are calculated from the reduced modulus values obtained from nanoindentation data using the following formula [27]

$$\frac{1}{E_r} = \frac{(1-\nu_i^2)}{E_i} + \frac{(1-\nu_s^2)}{E_s} \qquad (4.1)$$

where, E_r is the reduced modulus, E and ν are the Young's modulus and Poisson's ratio respectively. The subscripts 'i' and 's' represent the values for indenter and sample respectively. The indenter being a diamond indenter, the values of E_i and ν_i used here are 1140 GPa and 0.07 respectively. The Poisson's ratio of Al, ν_s is considered as 0.33. Nanocrystalline Al showed an average elastic modulus value of ~ 80 (± 5) GPa which is comparable with conventional coarse grained material (~ 70 GPa). It is to be noted that nanoindentation yielded slightly higher numbers, in majority of the studies, for both hardness and Young's modulus in comparison to other techniques. Therefore the higher modulus value obtained could be partly due to the technique used (i.e. nanoindentation) in this study. Even though the Young's modulus of nc materials was found to be slightly less than their coarse grained counterparts especially at very finer grain sizes [28-30], Liu et.al [31] have reported an Young's modulus value of 91.8 GPa for nano Al having a grain size of about 100 nm. The ball milling could introduce contamination from the milling media, however these contamination levels were found to be very less and sometimes negligible while working with soft metals such as Al. The contamination levels were significant while hard metals, ceramics etc. were ball milled. Regarding chemical analysis, EDS performed in SEM shows the presence of only Al and not any other elements. In the present work, to investigate the purity of the compacted end product, combustion technique was employed to find the presence of low atomic number elements such as carbon, nitrogen, hydrogen and sulfur. The obtained results indicated the presence of 0.9 wt.% of carbon which might have come from stearic acid (surfactant used during ball milling). There were no traces of

nitrogen, hydrogen and sulfur in the sample. To measure the amount of oxygen present in the compacted product, it is subjected to inert gas fusion technique and the final sample had 0.32 wt.% of Oxygen whereas the as-received material has 0.08 wt.% of Oxygen. However the presence of any oxide or carbide was not observed both during the X-Ray analysis (Fig. 4.1) as well as TEM (SAD pattern) analysis (Fig. 4.2 (b) inset). The TEM diffraction pattern contains the rings corresponding to only Al. It is plausible that these small amounts of oxygen and carbon might be going to the interstitial locations in the Al lattice. The contribution of this small oxygen content coupled with low carbon content, to the observed slightly higher Young's modulus value, is expected to be very minimal. However, at this stage, it appears that presence of these interstitial elements such as carbon, oxygen and employment of nanoindentation technique are only the possible reasons for this nc sample to have around 80 GPa as its Young's modulus against a value of 70 GPa for coarse grained Al.

Yield strength vs strain rate plots on logarithmic scale obtained from nanoindentation data for nc Al at three different peak forces of 1000 µN, 5000 µN and 8000 µN are shown in Fig. 4.7. Yield strength is calculated based on Tabor's law [32], $\sigma = H/3$, where σ is the Yield strength and H being the hardness value obtained from nanoindentation data. Loading rates for each peak force are selected in such a way that the strain rate changes by an order of magnitude for each datum point in the plot. The yield strength values are observed to be increasing with increasing loading rate which indicates the positive SRS. SRS is calculated from slope, m of the plots and values of 0.024, 0.027 and 0.054 are obtained at peak forces of 1000 µN, 5000 µN and 8000 µN respectively. The SRS value increased with increasing peak force. Researchers [33-35] have reported improved ductility along with high strength in ultrafine-grained metals and alloys. These materials also showed higher SRS values which can be correlated to improved ductility.

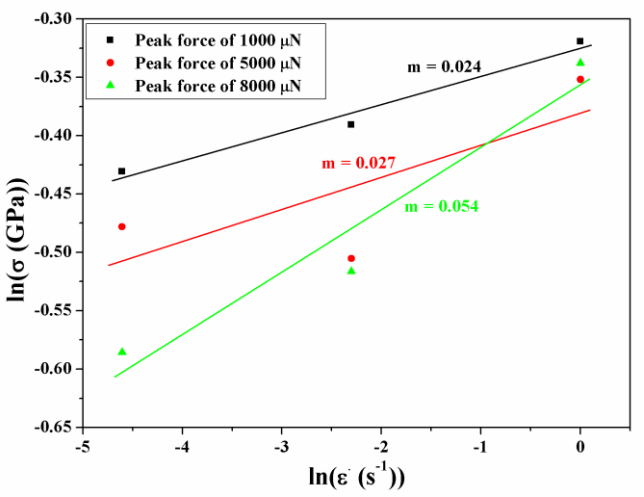

Fig. 4.7 Yield strength vs strain rate plots on logarithmic scale of nanocrystalline Al at various maximum peak forces of 1000 μN, 5000 μN and 8000 μN indicating higher strain rate sensitivity value of 0.054 at maximum peak force of 8000 μN.

The SRS values obtained for nc Al in the present work are higher by an order of magnitude when compared to the value of 0.004 obtained for coarse grained Al by May et.al [24]. They studied SRS behavior of ultrafine-grained Al processed by SPD and obtained a value of 0.014 at room temperature. These values were obtained from strain rate jump tests in compression. A value of 0.25 obtained at 423 K is close to the region of superplastic deformation behavior. Chinh et al. [33, 34] studied SRS of SPD processed ultrafine-grained Al and Al-30wt.%Zn alloys using micro and nanoindentation. They observed an unusually high SRS value of ~ 0.22 at room temperature for Al-30wt.%Zn and an elongation to failure of more than 150% was achieved. They emphasized that there is a close relationship between increased SRS and ductility.

Fig. 4.8 (a) shows the SPM image of the indent obtained using the nanoindenter by applying a peak force of 8000 μN at a loading rate of 800 μN/s. It is clear from the image that there is an observable amount of plasticity along the periphery of the indent. The corresponding line profile analysis (Fig. 4.8 (b)) of this indent suggests that there exists some amount of plastically flown region adjacent to the indent. In addition to that there are no cracks observed during indentation.

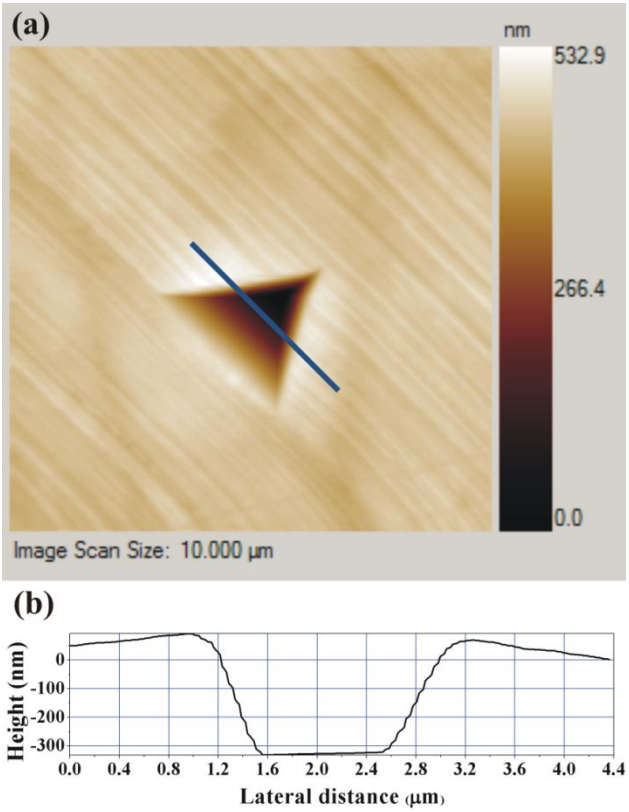

Fig. 4.8 (a) The Scanning Probe Microscopy image of the indent obtained using the nanoindenter by applying a peak force of 8000 µN at a loading rate of 800 µN/s and (b) the depth profile of the line drawn across the indent shown in (a).

These observations clearly suggest that this nc Al sample has some amount of ductility associated with it.

In the present work, the range of SRS values obtained at room temperature, 0.024 to 0.054 (Fig. 4.7) for peak forces of 1000 µN to 8000 µN, clearly indicate the influence of grain boundaries in the deformation process. At a low peak force of 1000 µN, where relatively few grains are involved in the deformation process, the nanohardness is observed to be less strain rate sensitive. As applied peak force is increased to 8000 µN, high SRS of 0.054 was obtained indicating the influence of grain boundaries as more grains are involved in the deformation process. Hence, it can be stated that increased SRS values are obtained when large volume

fraction of grain boundary area is involved in the deformation process. This strain rate dependent mechanical behavior helps in delaying the onset of localized deformation. Therefore, though ductility has not been measured quantitatively, high SRS values obtained from nanoindentation data qualitatively indicate good ductility of nc Al with an average grain size of 42 nm.

The deformation mechanisms in nc metals are believed to involve grain boundary mediated processes and/or deformation twinning and the unique mechanical properties observed could be attributed to these processes [36-38]. Elevated SRS values in nc face-centered cubic (fcc) metals help in reducing the plastic instability and this reduced plastic instability could be due to hardening of localized plastic deformation regions [36]. It was observed that nano-sized twins enhanced the SRS of Cu [36]. Deformation twinning has been observed experimentally in plastically deformed nc Al with the aid of high resolution transmission electron microscopy [37, 38]. In the current study, although exact deformation mechanism is not identified, within the scope of this manuscript, it is believed that it is the increased volume fraction of interfacial regions that are contributing to the enhanced SRS values.

4.4 Summary and conclusions

Nanocrystalline bulk Al samples synthesized through high energy ball milling followed by high pressure room temperature consolidation using a uni-axial press showed ~ 98 % of theoretical density. High density was achieved by the application of 1.5 GPa pressure for prolonged time of 1 hour. High pressure compaction seems to be a good method of consolidation in achieving good densities for nc Al. Hardness values were measured using depth sensing nanoindentation and an average hardness and elastic modulus values of 1.67 ± 0.09 GPa and 83 ± 8 GPa respectively were obtained at an applied peak force of 8000 μN and a strain rate of 10^{-2}

s^{-1}. Nanoindentation has been performed at different peak forces by varying the loading rates, so that the strain rate is changed by an order of magnitude. The hardness values were found to be increasing with increasing loading rate indicating positive SRS of the material. A SRS of 0.054 was obtained for an applied peak force of 8000 μN. The high SRS values obtained indicate good ductility of nc Al. In addition, the Scanning Probe Microscopy image of the indent shows the presence of plastically flown region around the periphery of the indent. Therefore, this work highlights the usefulness of nanoindentation to have a qualitative understanding on ductility of nano materials as evidenced by increased SRS values of nc Al.

References

[1] G.E. Dieter, Mechanical metallurgy, third ed. ed., McGraw-Hill Book Company, Boston, 1986.

[2] H. Gleiter, Nanocrystalline materials, Progress in Materials Science, 33 (1989) 223-315.

[3] K.S. Kumar, H. Van Swygenhoven, S. Suresh, Mechanical behavior of nanocrystalline metals and alloys, Acta Materialia, 51 (2003) 5743-5774.

[4] M.A. Meyers, A. Mishra, D.J. Benson, Mechanical properties of nanocrystalline materials, Progress in Materials Science, 51 (2006) 427-556.

[5] C. Suryanarayana, Nanocrystalline materials, International Materials Reviews, 40 (1995) 41-64.

[6] C. Suryanarayana, E. Ivanov, V. Boldyrev, The science and technology of mechanical alloying, Materials Science and Engineering: A, 304 (2001) 151-158.

[7] K.V. Rajulapati, R.O. Scattergood, K.L. Murty, G. Duscher, C.C. Koch, Effect of Pb on the mechanical properties of nanocrystalline Al, Scripta Materialia, 55 (2006) 155-158.

[8] H.W. Sheng, F. Zhou, Z.Q. Hu, K. Lu, Investigation of Al-Pb nanocomposites synthesized by non-equilibrium processes, Journal of Materials Research, 13 (1998) 308-315.

[9] K.V. Rajulapati, R.O. Scattergood, K.L. Murty, Z. Horita, T.G. Langdon, C.C. Koch, Mechanical properties of bulk nanocrystalline aluminum-tungsten alloys, Metallurgical and Materials Transactions A, 39 (2008) 2528-2534.

[10] C.C. Koch, R.O. Scattergood, K.L. Murty, The Mechanical Behavior of Multiphase Nanocrystalline Materials, JOM, 59 (2007) 66-70.

[11] C. Suryanarayana, C.C. Koch, Nanocrystalline materials – Current research and future directions, Hyperfine Interactions, 130 (2000) 5-44.

[12] C. Koch, I. Ovid'ko, S. Seal, S. Veprek, Structural nanocrystalline materials: fundamentals and applications, 2007, in, Cambridge University Press, Cambridge, UK.

[13] C.C. Koch, Optimization of strength and ductility in nanocrystalline and ultrafine grained metals, Scripta Materialia, 49 (2003) 657-662.

[14] E. Botcharova, J. Freudenberger, L. Schultz, Mechanical and electrical properties of mechanically alloyed nanocrystalline Cu–Nb alloys, Acta materialia, 54 (2006) 3333-3341.

[15] X. Liu, M.Q. Zeng, Y. Ma, M. Zhu, Melting behavior and the correlation of Sn distribution on hardness in a nanostructured Al–Sn alloy, Materials Science and Engineering: A, 506 (2009) 1-7.

[16] D.L. Bourell, J.R. Groza, Consolidation of Ultrafine and Nanocrystalline Powders, in: Powder Metal Technologies and Applications, ASM Handbook, ASM International, Metals Park, OH, 1998, pp. 1176–1227.

[17] J.R. Groza, Nanocrystalline Powder Consolidation Methods, in: C.C. Koch (Ed.) Nanostructured materials: Processing, Properties and Potential Applications, Noyes publications/William Andrew Publishing, Norwich, NY, 2002, pp. 115–178.

[18] L. Melúch, Warm Compaction of Aluminium Alloy Alumix 123, in, University of Birmingham, United Kingdom, 1999.

[19] W. Liu, Q. Zhou, Nanocrystalline Aluminum by Warm-Vacuum-Compaction Method, in: Supplemental Proceedings, General Paper Selections, The Minerals, Metals and Materials Society (TMS), A John Wiley & Sons, Inc., Publication, 2011, pp. 237-244.

[20] Y.T. Zhu, X.Z. Liao, Nanostructured metals - Retaining ductility, Nature Materials, 3 (2004) 351–352.

[21] R. Schwaiger, B. Moser, M. Dao, N. Chollacoop, S. Suresh, Some critical experiments on the strain-rate sensitivity of nanocrystalline nickel, Acta Materialia, 51 (2003) 5159-5172.

[22] Q. Wei, S. Cheng, K.T. Ramesh, E. Ma, Effect of nanocrystalline and ultrafine grain sizes on the strain rate sensitivity and activation volume: fcc versus bcc metals, Materials Science and Engineering: A, 381 (2004) 71-79.

[23] Y.M. Wang, E. Ma, Strain hardening, strain rate sensitivity, and ductility of nanostructured metals, Materials Science and Engineering: A, 375–377 (2004) 46-52.

[24] J. May, H.W. Höppel, M. Göken, Strain rate sensitivity of ultrafine-grained aluminium processed by severe plastic deformation, Scripta Materialia, 53 (2005) 189-194.

[25] L. Lu, S.X. Li, K. Lu, An abnormal strain rate effect on tensile behavior in nanocrystalline copper, Scripta Materialia, 45 (2001) 1163–1169.

[26] B.D. Cullity, Elements of X-ray Diffraction, Addison-Wesley Publishing Company, Inc., Reading, Massachusetts, 1956.

[27] W.C. Oliver, G.M. Pharr, An Improved Technique for Determining Hardness and Elastic Moduli using Load and Displacement Sensing Indentation Experiments, Journal of Materials Research, 7 (1992) 1564-1583.

[28] T.D. Shen, C.C. Koch, T.Y. Tsui, G.M. Pharr, On the elastic moduli of nanocrystalline Fe, Cu, Ni, and Cu–Ni alloys prepared by mechanical milling/alloying, Journal of Materials Research, 10 (1995) 2892-2896.

[29] Q. Wei, Z.L. Pan, X.L. Wu, B.E. Schuster, L.J. Kecskes, R.Z. Valiev, Microstructure and mechanical properties at different length scales and strain rates of nanocrystalline tantalum produced by high-pressure torsion, Acta Materialia, 59 (2011) 2423-2436.

[30] Z. Pan, Y. Li, Q. Wei, Tensile properties of nanocrystalline tantalum from molecular dynamics simulations, Acta Materialia, 56 (2008) 3470–3480.

[31] Y.Q. Liu, H.T. Cong, W. Wang, C.H. Sun, H.M. Cheng, AlN nanoparticle-reinforced nanocrystalline Al matrix composites: Fabrication and mechanical properties, Materials Science and Engineering: A, 505 (2009) 151-156.

[32] D. Tabor, The hardness and strength of metals, Journal Institute of Metals, 79 (1951) 1-18.

[33] N.Q. Chinh, T. Csanádi, J. Gubicza, R.Z. Valiev, B.B. Straumal, T.G. Langdon, The effect of grain boundary sliding and strain rate sensitivity on the ductility of ultrafine-grained materials, Materials Science Forum, 667-669 (2011) 677-682.

[34] N.Q. Chinh, T. Csanádi, T. Győri, R.Z. Valiev, B.B. Straumal, M. Kawasaki, T.G. Langdon, Strain rate sensitivity studies in an ultrafine-grained Al–30 wt.% Zn alloy using micro- and nanoindentation, Materials Science and Engineering A, 543 (2012) 117-120.

[35] R.Z. Valiev, I.V. Alexandrov, Y.T. Zhu, T.C. Lowe, Paradox of strength and ductility in metals processed by severe plastic deformation, Journal of Materials Research, 17 (2002) 5-8.

[36] Q. Wei, Strain rate effects in the ultrafine grain and nanocrystalline regimes—influence on some constitutive responses, Journal of materials science, 42 (2007) 1709-1727.

[37] X.Z. Liao, F. Zhou, E.J. Lavernia, D.W. He, Y.T. Zhu, Deformation twins in nanocrystalline Al, Applied Physics Letters, 83 (2003) 5062-5064.

[38] M. Chen, E. Ma, K.J. Hemker, H. Sheng, Y. Wang, X. Cheng, Deformation twinning in nanocrystalline aluminum, Science, 300 (2003) 1275-1277.

Chapter 5 - Strain Rate Sensitivity of Nanocrystalline Al-Pb Alloys

5.1 Introduction

The deformation behavior of nanocrystalline (nc) materials has been fascinating as it distinctly differs from that of coarse grained materials [1, 2]. In structural materials of engineering importance with micron sized characteristic length scales (grain size) in three dimensions, mobile dislocations located in the interiors of the grains play a dominant role, governing the plasticity [3]. In single phase materials, as the grain size is refined to less than 100 nm, the larger fractions of grain boundaries and other interfaces also will contribute to the plastic deformation in a significant way [4-9]. As grain size (d) is reduced, the strength increases in polycrystalline solids following Hall-Petch relation [10, 11]. However when the grain size approaches ≤100 nm, the Hall-Petch line will have a different slope, than that in 100 nm ≤d≤1000 nm range, albeit a positive number. With grain size further decreasing to about 10 nm, the Hall-Petch line exhibited a negative slope suggesting that the strength decreases in materials with these very fine grain sizes approaching the amorphous limit [4]. This is termed as Inverse Hall-Petch effect [12]. The interesting and superior mechanical properties of nc materials have thrown a grand challenge to the scientific community in the form of several uncertainties and unanswered questions while unfolding the underlying deformation mechanisms [5]. Finer grain size yielded higher strength values in nc single phase materials but at the expense of ductility [13]. Therefore, acceptable ductility levels should also be available along with strength in these materials for potential structural applications. Strain rate sensitivity (SRS) and activation volume are important parameters in a plastic deformation process [14]. SRS is a qualitative indicator of ductility of a given material, with higher SRS value means more ductility [15]. While suggesting

strategies to improve ductility of nc materials, Koch [16] indicated that incorporation of a second phase could delay the onset of localized deformation under tensile loading conditions. Although extensive research investigations have been carried out to explore the mechanical behavior of various single phase nc materials, studies that address the influence of a nano sized second phase dispersions in nc matrix with an average grain size less than 100 nm are very limited as on today [17]. Hardness/strength, SRS and activation volume of several single phase materials with nc features have been reported. Scientific attention is needed to understand the SRS and activation volume involved during the deformation of two-phase nc materials.

Therefore, motivated by the current status on deformation behavior of nc materials especially two-phase materials as mentioned above, attempts have been made to explore the role of a second phase on the mechanical properties (hardness, SRS, activation volume) of nc matrix. Al-Pb system was chosen as a model system as Al and Pb have a misfit of about 22% in size and they are immiscible both in liquid state as well as solid state. Bulk Al-Pb nanocomposites with varied Pb concentrations are fabricated using a combination of high energy ball milling and spark plasma sintering (SPS). Mechanical properties are evaluated using Vickers microindentation as well as nanoindentation. Nanoindentation was performed at different peak loads and loading rates to calculate SRS and activation volume associated during the deformation process.

5.2 Materials and methods

Al powder (99.0% purity, +200 mesh, S-D Fine Chemicals Limited) and Pb powder (99.9% purity, -200 mesh, Alfa Aesar) were used as raw materials. The milling parameters are same as in chapter 4 except that to prevent cold welding during milling 1.5 wt % stearic acid is added as

surfactant in this work. Various compositions were prepared with Pb content varying from 0-4 at%. The as-milled powders are compacted into 20 mm diameter disks by applying a uni-axial pressure of 600 MPa at room temperature. The compacted samples were sintered at 573 K using Spark Plasma Sintering (SPS). Structural characterization has been carried out using XRD and TEM. Thin electron-transparent samples were prepared by ion-beam milling using Gatan's precision ion polishing system (PIPS) for TEM observations. Microhardness measurements were carried out using Vickers microindenter. Nanoindentation was carried out at various peak loads (1000, 2000 and 4500 μN) and loading rates (100, 500 and 1000 μN/s) using Hysitron's TI950 Triboindenter. At a given set of load and loading rate, 49 indentations (7x7 matrix) were made to have a meaningful statistical analysis of the data. Loading rate divided by the peak load applied is considered as strain rate. Hence, for a peak load of 1000 μN the strain rates are 0.1, 0.5 and 1 s^{-1} respectively.

5.3 Results and discussion

5.2.1 Structural details of nanocrystalline Al-Pb alloys

X-ray diffractograms of various Al-Pb alloys in as-milled condition are shown in Fig. 5.1. It is clear that the reflections corresponding to only Al and Pb are present, ruling out the formation of any solid solution or meta-stable phase during ball milling. The precise lattice parameter of Al in all Al-Pb alloys, calculated using Nelson-Riley extrapolation analysis [18], yielded a value of 4.0481±0.0005 Å against standard literature value of 4.0495 Å indicating that there is no considerable change in the lattice parameter of Al and the difference is within the instrumental error. Grain size of Al was calculated using Scherrer equation [19] after accounting for instrumental broadening. The grain size of Al in all the Al-Pb alloys is about 45±6 nm.

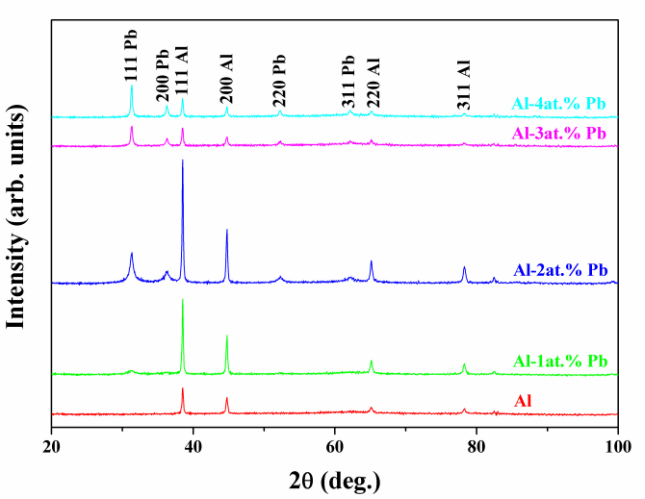

Fig. 5.1 X-ray diffractograms of ball milled Al-Pb nanocomposites showing a two phase mixture of Al and Pb.

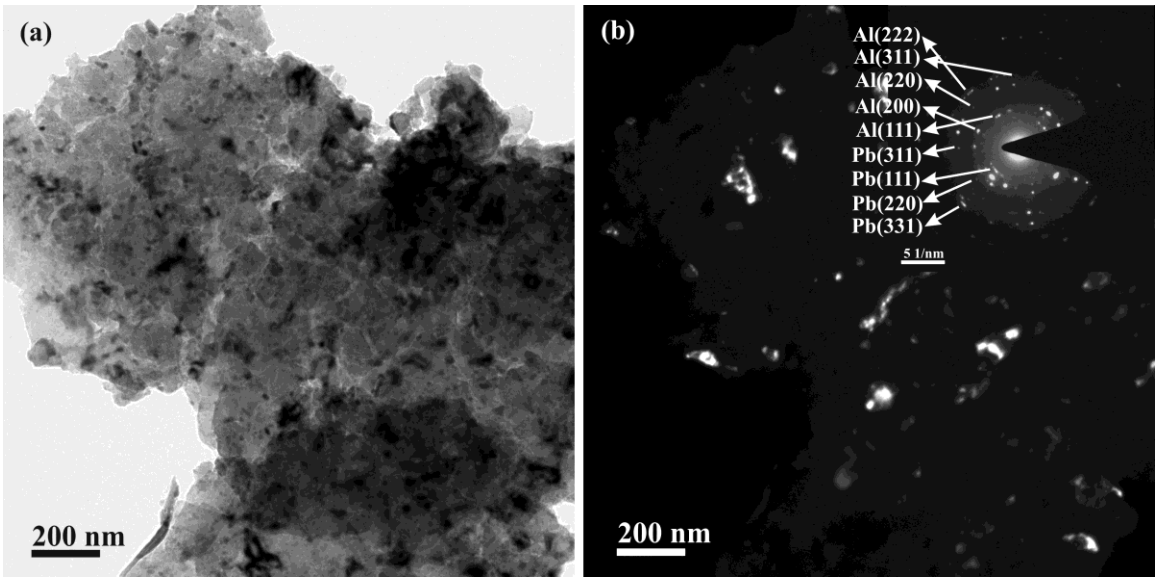

Fig. 5.2 (a) Bright field and (b) dark field transmission electron micrographs, and the corresponding diffraction pattern in the inset of Al-2at.%Pb powder milled for 50 hours.

Although, Pb content was varied between 0-4at.% in various alloys, the grain size of Al matrix remains the same suggesting that Pb is not influencing the grain size in nc Al-Pb system. This is in well agreement with earlier reports on nc Al-Pb alloys prepared using ball milling [20, 21]. The microstructural features of Al-2at.%Pb alloy obtained using TEM are shown Fig. 5.2.

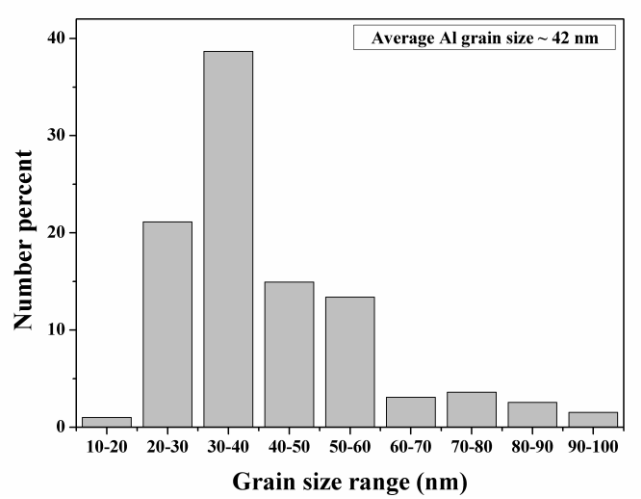

Fig. 5.3 The grain size distribution of Al in Al-2at.%Pb powder milled for 50 hours.

Fig. 5.2 (a) is the bright field image, Fig. 5.2 (b) is the dark field image with diffraction pattern in the inset. Fig. 5.3 is the histogram showing grain size distribution of Al in Al-2at.%Pb alloy in as-milled condition. Grain size calculated using linear intercept method from 200 grains is about 42 (±17) nm. Indexing of the diffraction pattern (Fig. 5.2 (b) inset) shows that reflections corresponding to only Al and Pb are present which is consistent with XRD analysis (Fig. 5.1).

To study the bulk mechanical behavior of these Al-Pb nanocomposites, milled powders are compacted into 20 mm diameter discs (Fig. 5.4) using SPS at 573 K.

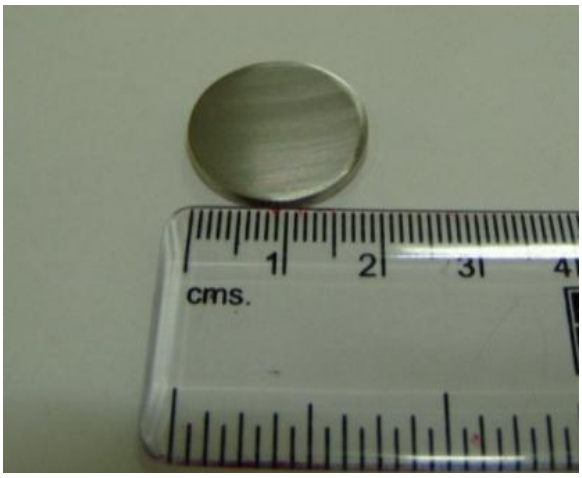

Fig. 5.4 Sintered nanocrystalline Al-Pb nanocomposite.

X-ray diffractograms of various Al-Pb alloys recorded post-sintering are given in Fig. 5.5. From Fig. 5.5, it is evident that only two phase mixtures of Al and Pb are present in these alloys. Microstructural features of Al-2at.%Pb alloy obtained using TEM are shown in Fig. 5.6 (a), (b) and Fig. 5.7. Fig. 5.6 (a) is the bright field image, Fig. 5.6 (b) is the dark field image with diffraction pattern in the inset.

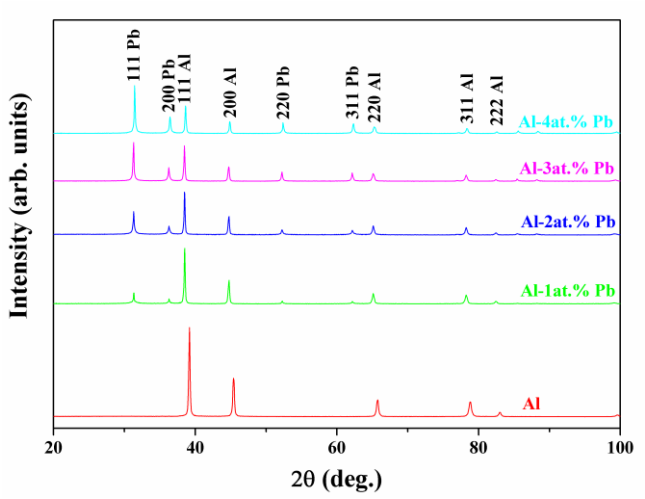

Fig. 5.5 X-ray diffractograms of sintered Al-Pb nanocomposites showing two phase mixture of Al and Pb.

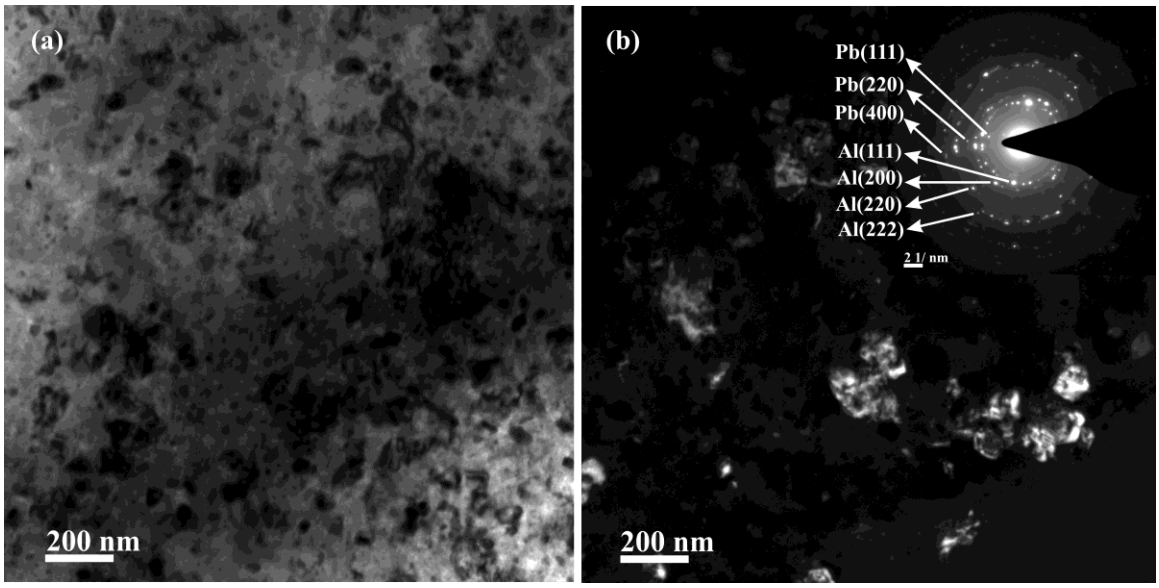

Fig. 5.6 Bright field and dark field transmission electron micrographs ((a) and (b)) and the corresponding diffraction pattern (inset of (b)) of sintered Al-2at.%Pb alloy.

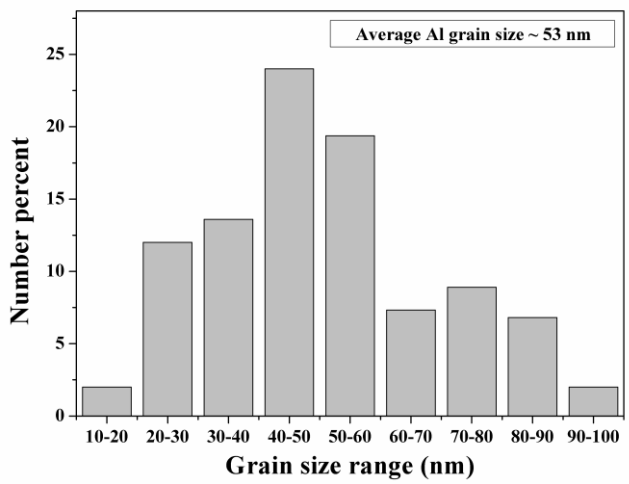

Fig. 5.7 The histogram showing the distribution of Al grain size in sintered Al-2at.%Pb alloy.

Fig. 5.7 is the histogram showing grain size distribution of Al in Al-2at.%Pb alloy in as-sintered condition. Grain size calculated from about 200 grains using linear intercept method is 53 (±18) nm. Grain size of Al has increased from 42 nm to 53 nm during SPS. Even after exposing these alloys to homologous temperature (T/T_M) of 0.6, there was no significant grain growth. This could be because of Pb present in the Al grain boundaries. Pb might be pinning the grain boundaries and affecting their mobility at elevated temperatures and in turn resulting in minimum grain growth. Al-Pb alloys in the present study resulted in 92% density after SPS.

High resolution TEM image shown in Fig. 5.8 infers that the Pb particles (circled) are about 6-8 nm in diameter dispersed in Al matrix. To further elucidate the presence and distribution of Pb, Z-contrast imaging was employed in scanning transmission electron mode (STEM) in TEM. Z-contrast imaging aids in identifying the presence of two different elements/phases with wide variation in their atomic number, Z. The intensity, I scales as Z^2 (i.e., $I \propto Z^2$) [22]. Fig. 5.9 is the Z-contrast image obtained from Al-2at.%Pb sample and it is clear that the region that is brighter in contrast belongs to Pb phase. It is evident that Pb is segregating to Al grain boundaries (shown with arrows) and also dispersed as fine particles within the grain. The

distribution of Pb particle size is shown in Fig. 5.10 and the average Pb particle size assumes to be 6 (±2) nm.

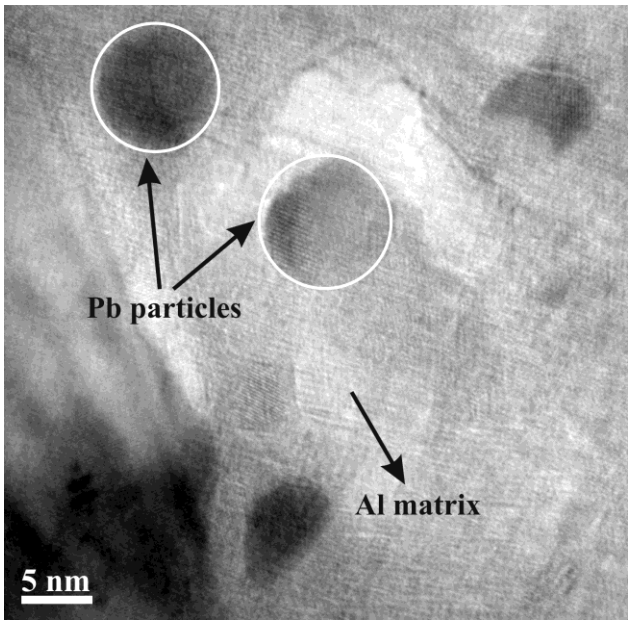

Fig. 5.8 High resolution transmission electron micrograph of sintered Al-2at.%Pb sample indicating Pb particles of ~ 6 nm dispersed in Al matrix.

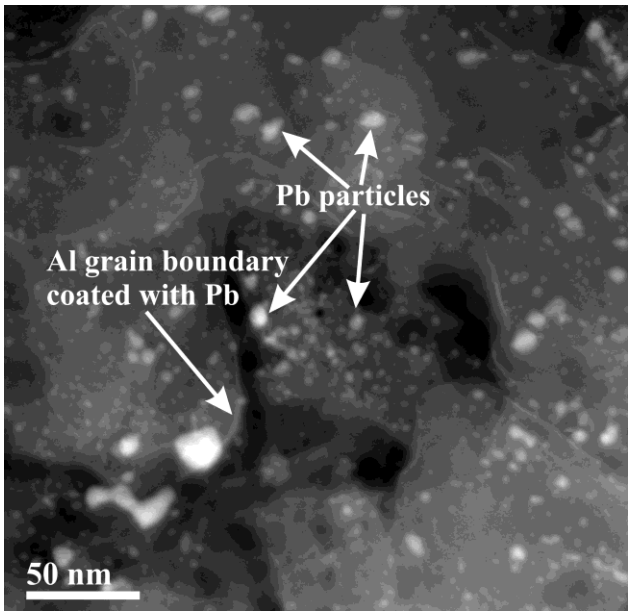

Fig. 5.9 High angle annular dark field image of sintered Al-2at.%Pb sample. The arrow indicates the nc Al grain boundary decorated with Pb phase. The smaller Pb particles are also seen in the grain interior.

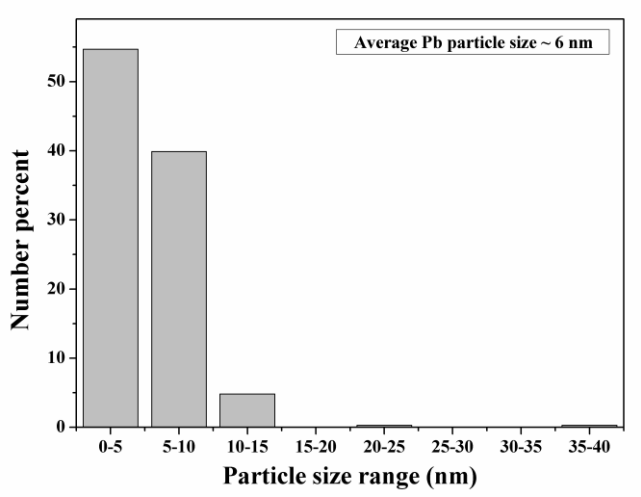

Fig. 5.10 Size distribution plot of Pb particles obtained from high angle annular dark field image (Fig. 5.9) of sintered Al-2at.%Pb sample showing an average particle size of ~ 6 nm.

5.2.2 Hardness measurements using microindentation and nanoindentation

Microhardness measurements are made at various loads in the range of 25-100 g and the obtained data is shown in Fig. 5.11. Nanoindentation data obtained at various loads in the range of 0.1-0.45 g is also shown in Fig. 5.11 for comparison purpose. From Fig. 5.11, it is evident that as Pb content is increased, hardness of these composites also increases by about 7-15% up to 2at.%Pb additions, whereas the addition of Pb above 2at.%, resulted in decrease in hardness. Microhardness values measured for a given composite are always lower than that of nanohardness values. This could be because of indentation size effect (ISE) [23-31] as the loads employed in nanoindentation (0.1 g) are almost about three orders of magnitude lower than those in microindentation (100 g). This observation is also in agreement with various studies performed on various material systems using both microindentation and nanoindentation [23]. Various reasons such as confinement of deformation only to small volumes, elastic recovery after indentation at small loads, indenter-sample friction/surface effects, strain gradient plasticity etc. were attributed to the ISE as summarized in ref. [24]. However, there is no clear understanding and/or universal agreement among the research community for the ISE observed

in various materials. In the current study, even though there is an indentation size effect, the trend in hardness variation among various alloys as well as at various loads is same for both microindentation and nanoindentation data (Fig. 5.11). In addition, it is to be noted that, in order to test the reasonable amount of materials, microindentation as well as nanoindentation testing was carried out at various loads and loading rates thus sampling reasonably larger volume during deformation so that the bulk behavior of these two-phase nanomaterials could be understood.

Since there is a size mismatch of about 22% among Al and Pb atoms, it is possible that Pb atoms initially (i.e., at lower concentrations) segregate to Al grain boundaries. As Pb content is increased, once Al grain boundaries get saturated with Pb atom segregates, excess Pb will be available inside the grains as small Pb particles as it is clearly evident from the Z-contrast image of Al-2at.%Pb alloy in the present investigation (Fig. 5.7). In the earlier experimental work [20], average grain size of the nc Al matrix was reported to be 28 nm. Therefore, in this case, to have a monolayer coating along nc Al grain boundaries, a Pb volume fraction of about 1.4% is required as per $f = 1/(1 + 2.55d)$ [32], where f is volume fraction and d is grain size.

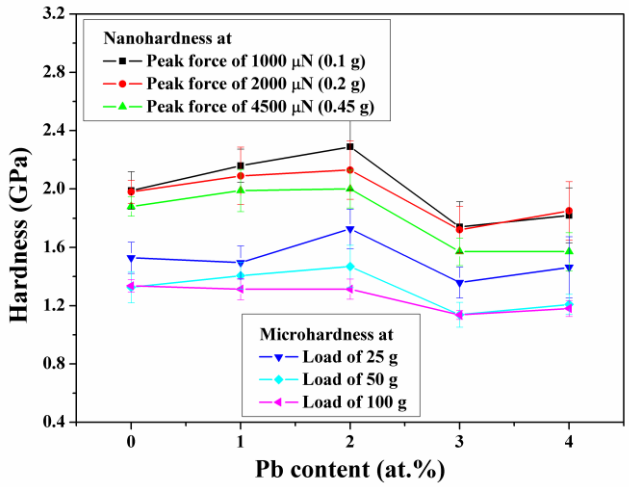

Fig. 5.11 Variation of hardness with increasing Pb content of Al-Pb nanocomposites obtained by performing microhardness testing in the load range of 25-100 g. The hardness data obtained using nanoindentation at different peak forces (1000 μN, 2000 μN and 4500 4500 μN) with a loading rate of 500 μN/s is also shown in the same plot.

In the current study (d = 53 nm), only 0.7 vol. % is sufficient to saturate the grain boundaries. The remaining Pb is expected to be present inside the grains in the form of particles. In addition, these small particles become larger in size with further increase in Pb content [21]. Therefore, contributions to the observed mechanical behavior in the current study come from the following factors: i) Al matrix grain size (53 nm), ii) Pb atom segregates present in nc Al grain boundary (Fig. 5.9), iii) size and distribution of Pb particles present in the intra-granular regions (Fig. 5.9).

Experimental studies on different Al-Pb alloys with Pb content varying between 0.1-1.0 at.% carried out by Rajulapati et al. [20] showed a precipitous softening effect as the Pb content is increased. Al-1at.%Pb sample with Al matrix grain size of 28 nm had a lower hardness value by about 35% in comparison to nc Al with a similar grain size. The dramatic reduction in hardness was attributed to the presence of Pb atom segregates in nc Al grain boundaries and thereby making lattice defect generation easier during deformation. Subsequently, supporting their results, Jang et al. [32] also noticed decrease in yield stress with increased Pb content using Monte Carlo and Molecular Dynamics simulations on Al-Pb alloys containing 1, 2 and 3 at.% Pb. But, this decrease in yield strength observed is less dramatic than the softening observed experimentally earlier [20]. Their simulations also showed that Pb atoms segregate to Al grain boundaries and this segregation resulted in lower yield stresses. Prior to these two studies, investigations by Sheng et al. [21] on Al-Pb nanocomposites indicated that small amounts of Pb, in the form of nano particles may strengthen the Al matrix.

In order to have a detailed understanding on deformation mechanisms that are being operated in these various two-phase Al-Pb alloys, the model equations developed by Scattergood et al. [33] have been considered. These model equations for Hall-Petch strengthening due to decrease in grain size and Orowan particle strengthening in nc alloys are as follows

$$H_{\mathrm{HP}} = H_0 + \frac{3G\mathrm{b}}{\pi}\frac{1}{d}\ln\frac{d}{r_0} \qquad (5.1)$$

$$\Delta H_p = \frac{3G\mathrm{b}}{\pi}\left\{\frac{1}{d\left(1-\sqrt{f}\right)}\left[\frac{d\sqrt{f}}{D}ln\frac{D}{r_0} + \ln d\right] - \frac{1}{d}\ln\frac{d}{r_0}\right\} \qquad (5.2)$$

Where H_{HP} in Eq.(5.1) is the hardening due to grain size d of matrix, H_0 is a free parameter, G is the shear modulus, b is the Burgers vector and r_0 is the core-cutoff distance in the dislocation line energy. Hardening increment due to Orowan particle strengthening is given by ΔH_p in Eq. (5.2) where f and D are the volume fraction and particle size of second phase particles having $D < d$. Based on these equations the hardness values of the Al-Pb alloys are estimated using G = 26.1 GPa, $\boldsymbol{b}$ = 0.286 nm, r_0 = 1 nm, d_{Al} = 53 nm, D = 6 nm and H_{Al} = 1.27 GPa for Al matrix. Fig. 5.12 shows the variation of hardness with Pb content for various Al-Pb alloys. For readers' convenience the hardness variation in the plots is shown with varying atomic percent Pb, but, calculations are done based on equivalent volume percent.

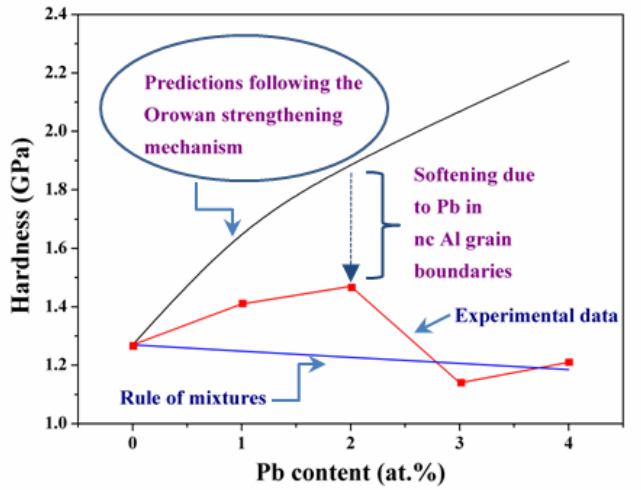

Fig. 5.12 Variation of hardness with Pb content obtained using Eq. (5.1) & Eq. (5.2). Rule of mixtures line and the plot obtained from measured hardness values (Vickers, 50gm load) are also shown.

Rule of mixtures line and the plot obtained from measured hardness values from microindentation tests performed with an applied load of 50 gm are also shown. Hardness values of Al and Pb used for rule of mixtures line are 1.27 GPa and 80 MPa respectively. Experimentally measured hardness values show increasing trend initially with increasing Pb content, then a decreasing trend for larger Pb additions (Fig. 5.12). Initial increasing hardness trend for lower Pb additions is well above the rule of mixtures, whereas the decreasing trend for higher Pb additions is nearly close to rule of mixtures. The predicted Orowan plot obtained using model equations show higher values than the measured values. While calculating the Orowan plots it is considered that the total volume of the Pb particles has equal particle size (6 nm) in all the nc Al-Pb alloys, but, practically it may not be the case and range of particle sizes could exist (Fig. 5.10) in the overall distribution. However the distribution is nearly uniform and significant fraction of particles are indeed in the range of 6-8 nm. Smaller particles and uniform distribution show influential effect on strengthening, whereas larger particles and non-uniform distribution may not show greater strengthening effect. In fact, there is a possibility that non-uniform distribution and segregation of larger second phase particle might lead to softening of the material. It is clear from Fig. 5.9 and Fig. 5.10 which show the transmission electron micrograph and the histogram of Pb particle size distribution of sintered Al-2at.%Pb nanocomposite that fine Pb nano particles are uniformly distributed and major fraction of which are under 10 nm. Hence, the initial increasing hardness trend observed experimentally can be attributed to the strengthening effect due to the presence of uniformly distributed Pb particles in Al matrix. No significant change in the grain size of Al matrix was observed with Pb content for various nc Al-Pb alloys, hence it is imperative that the second phase content along with its size and distribution is solely responsible for the observed mechanical behavior.

Investigations carried out by Liu et al. [34] on nanostructured Al-20wt.%Sn alloy resulted in both hardening and softening of the Al matrix. Sintering of ball milled powders below eutectic temperature (487 K) resulted in homogeneous distribution of Sn in Al and sintering above eutectic temperature resulted in inhomogeneous distribution and this behavior in-turn resulted in hardening and softening effect respectively in nc Al-Sn system. Hence the size and distribution of second phase particles in the matrix greatly influence hardness of the composite. Effect of nano sized harder 'W' phase on the mechanical properties of softer Al matrix were earlier studied by Rajulapati et al. [35]. Hardness of Al matrix increased with increasing volume percent of W. It was observed that the hardening effect was much higher than that is expected from rule of mixtures. Based on the existing models on strengthening mechanisms in nc materials suggested by Scattergood et al. [33], the hardening effect was attributed to the Orowan-particle strengthening due to small W particles dispersed in nc Al matrix. Recently Atwater et al. [36] reported that the harder W phase enhanced the thermal stability of nc Cu-W alloys leading to improved mechanical properties. More recent work on multi-phase nc Al-10at.%W composite [37] resulted in a high hardness of 5.2 GPa and SRS of 0.025.

5.2.3 Elastic modulus using nanoindentation

Elastic modulus values are calculated from reduced modulus values obtained from nanoindentation data using the following formula [38]

$$\frac{1}{E_r} = \frac{(1-\nu_i^2)}{E_i} + \frac{(1-\nu_s^2)}{E_s} \qquad (5.3)$$

where, E_r is the reduced modulus, E_i and ν_i are the Young's modulus and Poisson's ratio of the diamond indenter which are considered as 1140 GPa and 0.07 respectively. ν_s is the Poisson's ratio of the sample, 0.33. Nanocrystalline Al showed an average elastic modulus value of ~

80GPa which is comparable with that of conventional Al (~ 70 GPa). The modulus values decreased with increasing Pb addition which is usual behavior due to the low elastic modulus value of Pb. The modulus values have been reduced by ~ 20-27% for various Al-Pb alloys with Pb addition. The detailed compositional analysis performed using inert gas fusion technique reveals that nc Al and nc Al-4 at %Pb alloy had an oxygen content of 0.32 wt% and 0.36 wt. % respectively. Therefore this minor oxygen content present in these samples will have very minimal effect on E as well as other mechanical properties.

This decrement in elastic modulus of various nc Al-Pb alloys could have the contribution from the presence of softer Pb phase with low elastic modulus. In the simulation work performed in ref. [32], pure Al possessed an elastic modulus in the range of 51-63 GPa as the grain size is varied between 5 nm and 30 nm. Al-Pb alloys had an elastic modulus in the range of 50-56 GPa resulting in an overall reduction of nearly 10% with respect to pure Al. Several experimental studies showed that the elastic modulus will be decreased for nc materials in comparison to their coarse grained counterparts especially at very finer grain sizes [39-41]. In the current study, it is experimentally found that the Pb additions resulted in the decrement of E by about 20-27%. It is to be noted that the grain size of nc Al matrix in the current study is about 53 nm where as in ref. [32], it is 10 nm. Thus the significant variation in E of nc Al-Pb alloys experimentally measured in the current study and theoretically calculated in ref. [32] could be because of different grain sizes employed and also the variation in different experimental conditions prevailing in experiments and simulations.

5.2.3 Strain rate sensitivity and activation volume studies

Nanoindentation is a promising technique to evaluate SRS and activation volume as it offers variation of strain rate by four orders of magnitude at different peak loads [42]. SRS and activation volume studies have been carried out on different nc Al-Pb alloys by performing nanoindentation at various peak loads and loading rates. Fig. 5.13 represents yield strength vs. strain rate plots (on logarithmic scale) obtained from nanoindentation data for various nc Al-Pb alloys and the corresponding linear fits are also shown in Fig. 5.13 at various peak loads. Indentations are performed at three different peak forces of 1000 µN, 2000 µN and 4500 µN with loading rates of 100 µN/s, 500 µN/s and 1000 µN/s for each peak force. Yield strength, σ is calculated based on Tabor's equation [43], $\sigma = H/3$, where H being the hardness value obtained from nanoindentation data. Loading rate divided by the peak load applied is considered as strain rate [44, 45]. SRS values obtained from the slope of each plot are also shown in the plots. The yield strength values are observed to be increasing with increasing loading rate which indicates the positive SRS of these two phase nanostructured materials.

In the current study, at room temperature, SRS values of 0.036 and 0.1 are obtained for nc Al and Al-4at.%Pb respectively. As shown in Fig. 5.14, SRS values increased with increasing Pb content. The nanocomposite with 4at.%Pb showed an SRS value of 0.1 which is high for room temperature deformation conditions. It is clear from Fig. 5.14 that the second phase particles are definitely contributing to the enhanced SRS values which might result in improved ductility as suggested by Koch [16].

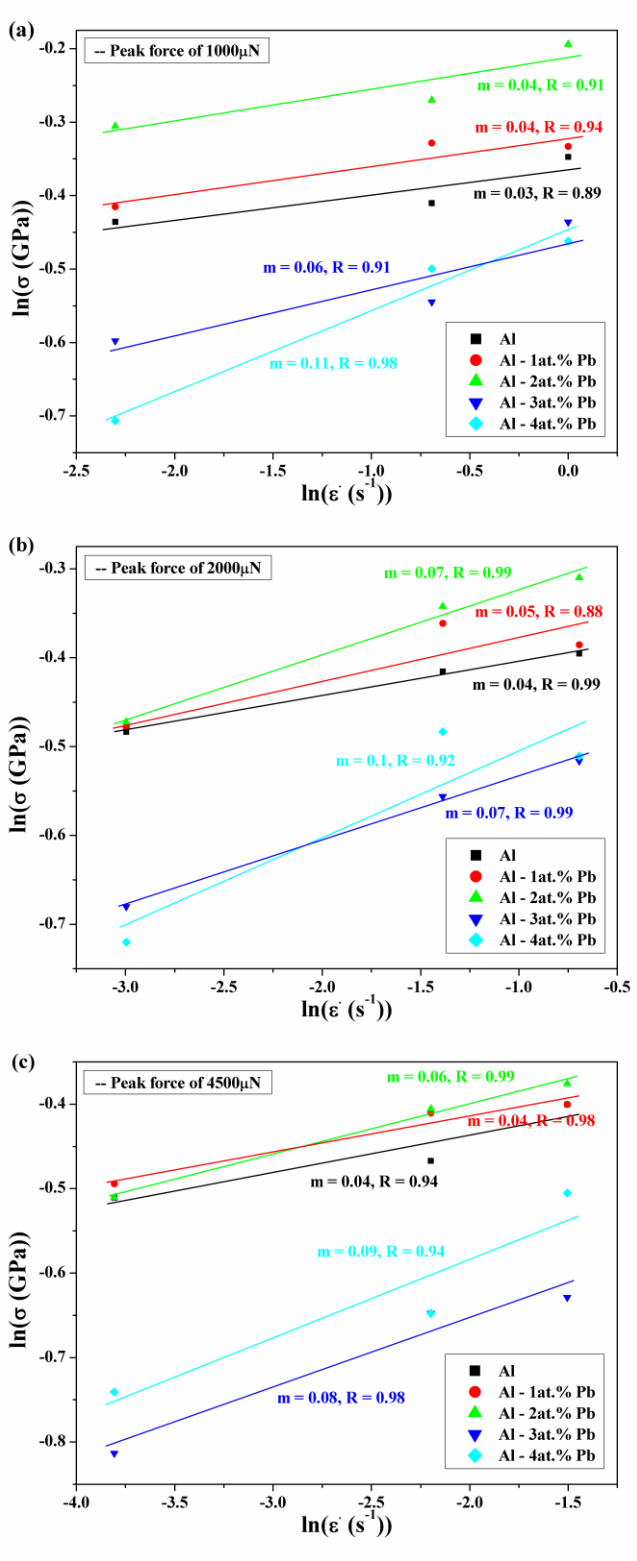

Fig. 5.13 Yield strength vs. strain rate plots on logarithmic scale of Al-Pb nanocomposites at maximum peak force of (a) 1000 μN, (b) 2000 μN and (c) 4500 μN.

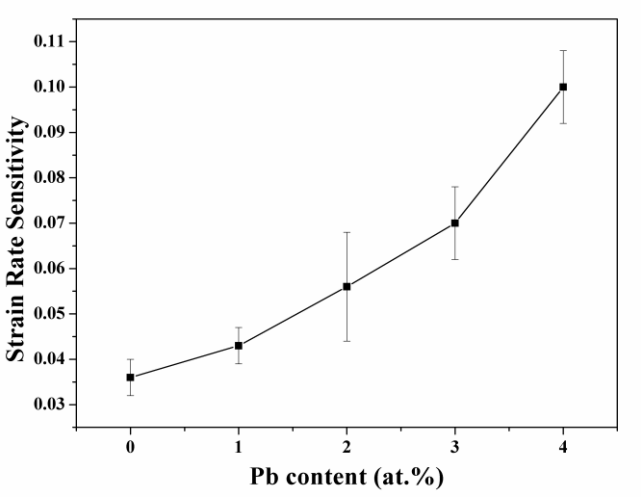

Fig. 5.14 Variation of strain rate sensitivity (SRS) with Pb content for Al-Pb nanocomposites indicating the increase in SRS with increasing Pb content. The error bars indicate the variation in SRS of a given composite at various peak loads (1000-4500 µN).

Activation volume, v^* for flow stress of these materials, assuming constant microstructure and constant temperature, can be calculated using the following relation [14]

$$v^* = \sqrt{3}kT\left(\frac{\partial ln\dot{\varepsilon}}{\partial \sigma}\right) \qquad (5.4)$$

Where k is the Boltzmann constant, T is the absolute temperature, $\dot{\varepsilon}$ is the strain rate and σ *is* the yield strength. The slope of the plot of $kTln(\dot{\varepsilon})$ vs. σ gives the activation volume in m^3 [46] which is converted to the unit of b^3 where b is the Burgers vector of Al (0.286 nm). The calculated v^* values (Table 5.1) for various Al-Pb nanocomposites are much lower when compared to microcrystalline materials.

SRS data reported in the literature on various nc materials suggests that the nc materials are rate sensitive [47-58]. Single phase fcc materials have displayed enhanced SRS whereas the bcc materials showed reduced SRS in comparison to their respective coarse grained counterparts. Investigations by Chinh et al. [53, 54] on ultrafine grained Al and Al-30wt.%Zn alloy, revealed the possibility of obtaining improved ductility through severe plastic deformation (SPD) process.

Table 5.1 Activation volumes of various Al-Pb nanocomposites.

Material	Activation volume, v^* (b^3)
Al	6.15 ± 0.62
Al-1at.%Pb	5.49 ± 0.72
Al-2at.%Pb	4.12 ± 0.41
Al-3at.%Pb	4.12 ± 0.26
Al-4at.%Pb	2.84 ± 0.13

They observed high SRS values for these materials and suggested that enhanced diffusion along the grain boundaries leading to grain boundary sliding resulted in increased ductility in Al-30wt.%Zn alloy. They emphasized that there is a close relationship between increased SRS and ductility in these materials.

Asaro and Suresh have developed mechanistic models [14] for activation volume and rate sensitivity and estimated increased SRS values and decreased activation volumes ($3 – 10b^3$) for fcc metals. These estimated values are consistent with available experimental data. The activation volumes increased with increasing grain size. These models were based on the emission of dislocations from stress concentrations at a grain boundary or a twin boundary. Recently, Niu et al [59], studied the SRS behavior of nanostructured two phase Cu-Cr and Cu-Zr multilayer thin films. These represent fcc-bcc and fcc-hcp combinations. In case of Cu-Cr, SRS was found to be varying between 0.022-0.031 whereas for Cu-Zr, SRS was in between 0.012-0.025. Cu-Cr had an activation volume of 11.57-15.20 b^3 whereas Cu-Zr had an activation volume in the range of 14.35-22.13 b^3. Although the single phase bcc metals display a reduced SRS, the presence of bcc phase is not affecting the overall SRS of Cu-Cr composite in this case. This is also in agreement with our recent findings on SRS of nc multi-phase Al-10W composite

[37] where the bcc $Al_{12}W$ phase did not affect the SRS of pure Al. In this work, nanostructured Al-10W composite had an SRS of 0.025±0.002 and an activation volume in the range of 1.63-3.88 b^3. It is to be noted that traditionally for conventional coarse grained materials during ASTM testing procedures either strain rate jump tests or stress relaxation tests have been used. In addition, the entire microstructure is assumed to be constant during these tests [60]. In the current study, nanoindentation technique was employed to evaluate SRS and activation volume owing to the sample dimensions. Tests were performed at various peak loads and loading rates on different locations of the sample. This procedure was followed because by performing indentations at various loads and loading rates at different locations of the sample, we wanted to ensure that we are evaluating the bulk behavior of the sample to a reasonable extent possible. The reported values for SRS and activation volume for various nc Al-Pb alloys in the current study are apparent values of SRS and activation volume respectively.

In case of two-phase nc materials where both matrix and second phase are having nc structural features, contribution of second phase and its crystal structure to the overall SRS of the composite material could be significant. Nanocrystalline Al-4at.%Pb composite had SRS of 0.1 which is almost an order of magnitude high in comparison to that of single phase fcc metals. It is to be noted that, in the present investigation, it is fcc-fcc combination as both Al and Pb are of fcc structure.

Both SRS and activation volume are the quantitative measures for rate sensitivity of flow stress to the loading rate. In conventional coarse grained materials with grain size around 30-40 µm, dislocations control the plasticity and measured activation volumes are ~1000 b^3. In all the single phase nc materials reported so far, the measured activation volumes values are about 10-135 b^3. The activation volumes measured for nc Al-Pb composites in the present study are also in

agreement with earlier studies and are in the range of 2.84-6.15 b^3, suggesting that the second phase has no influential effect on overall activation volume of two-phase nanocomposites. These low activation volumes suggest that grain boundary mediated processes [61-63] are controlling the plastic deformation in these two phase nanomaterials.

5.4 Summary

A combination of high energy ball milling and spark plasma sintering (at 573K) have been used to fabricate bulk nc two phase Al-Pb alloys. The average grain size of the Al matrix in nc Al-2at%Pb alloy is about 53 nm and Pb particles are about 6 nm in diameter. The mechanical properties are measured using both microindentation and nanoindentation. The hardness of nc Al-Pb alloys initially increases with additions up to 2at.%Pb and then decreases. This trend is same for both microindentation and nanoindentation studies. Hardness values obtained using microindentaion are smaller than that of nanoindentation probably due to the indention size effect. It appears that the final hardness in these nc alloys is dictated by the competition between the Orowan particle strengthening and grain boundary weakening processes. Pb phase seem to be enhancing the SRS of nc Al-Pb alloys and the SRS increased with increasing Pb content reaching a value of 0.1 for alloy with 4at.%Pb. Pb present especially in the grain boundaries might be influencing the SRS via some grain boundary mediated processes leading to higher SRS in the current investigation. The activation volume values for various Al-Pb alloys are in the range of 2.84-6.15 b^3. The enhanced SRS values and low activation volume numbers indicate that dislocations are not controlling the plasticity in these materials, instead, it is expected that the interfaces viz., grain boundaries and matrix/particle boundaries are the deciding factors of the deformation mechanisms.

References

[1] G.W. Nieman, J.R. Weertman, R.W. Siegel, Mechanical behavior of nanocrystalline Cu and Pd, Journal of Materials Research, 6 (5) (1991) 1012–1027.

[2] H. Gleiter, Nanostructured materials: basic concepts and microstructure, Acta Materialia, 48 (2000) 1-29.

[3] D. Hull, D.J. Bacon, Introduction to Dislocations, 5 ed., Butterworth-Heinnmann, UK, 2011.

[4] K.S. Kumar, H. Van Swygenhoven, S. Suresh, Mechanical behavior of nanocrystalline metals and alloys, Acta Materialia, 51 (2003) 5743-5774.

[5] M.A. Meyers, A. Mishra, D.J. Benson, Mechanical properties of nanocrystalline materials, Progress in Materials Science, 51 (2006) 427-556.

[6] H. Van Swygenhoven, P.M. Derlet, Hasnaoui, Atomic mechanism for dislocation emission from nanosized grain boundaries, Phys. Rev. B, 66 (2002) 024101.

[7] V. Yamakov, D. Wolf, S.R. Phillpot, A.K. Mukherjee, H. Gleiter, Dislocation processes in the deformation of nanocrystalline aluminium by molecular-dynamics simulation, Nature Materials, 1 (2002) 45-48.

[8] J. Schiøtz, T. Vegge, F.D. Di Tolla, K.W. Jacobsen, Atomic-scale simulations of the mechanical deformation of nanocrystalline metals, Physical Review B - Condensed Matter and Materials Physics, 60 (1999) 11971-11983.

[9] H. Van Swygenhoven, M. Spaczer, A. Caro, Microscopic description of plasticity in computer generated metallic nanophase samples: a comparison between Cu and Ni, Acta Materialia, 47 (1999) 561.

[10] E.O. Hall, The deformation and ageing of mild stee: III Discussion of results, Proc. Phys. Soc. B, 64 (1951) 747-753.

[11] N.J. Petch, The cleavage strength of polycrystals, J. Iron and Steel Institute, (1953) 25-28.

[12] C.C. Koch, J. Narayan, The Inverse Hall-Petch Effect—Fact or Artifact?, in: MRS Proceedings, Cambridge Univ Press, 2000, pp. B5. 1.1.

[13] C.C. Koch, D.G. Morris, K. Lu, A. Inoue, Ductility of nanostructured materials, MRS Bulletine, 24 (1999) 54-58.

[14] R.J. Asaro, S. Suresh, Mechanistic models for the activation volume and rate sensitivity in metals with nanocrystalline grains and nano-scale twins, Acta Materialia, 53 (2005) 3369-3382.

[15] M.Y. Wu, O.D. Sherby, Superplasticity in a silicon carbide whisker reinforced aluminum alloy, Scripta Metallurgica, 18 (1984) 773-776.

[16] C.C. Koch, Optimization of strength and ductility in nanocrystalline and ultrafine grained metals, Scripta Materialia, 49 (2003) 657-662.

[17] C.C. Koch, R.O. Scattergood, K.L. Murty, The Mechanical Behavior of Multiphase Nanocrystalline Materials, JOM, 59 (2007) 66-70.

[18] B.D. Cullity, Elements of X-ray Diffraction, Addison-Wesley Publishing Company, Inc., Reading, Massachusetts, 1956.

[19] P. Scherrer, Determining the size and the internal structure of colloidal particles by means of X-rays, GöttingerNachrichten Gesell, 2 (1918) 98-100.

[20] K.V. Rajulapati, R.O. Scattergood, K.L. Murty, G. Duscher, C.C. Koch, Effect of Pb on the mechanical properties of nanocrystalline Al, Scripta Materialia, 55 (2006) 155-158.

[21] H.W. Sheng, F. Zhou, Z.Q. Hu, K. Lu, Investigation of Al-Pb nanocomposites synthesized by non-equilibrium processes, Journal of Materials Research, 13 (1998) 308-315.

[22] S.J. Pennycook, L.A. Boatner, Chemically sensitive structure-imaging with a scanning-transmission electron microscope, Nature, 336 (1988) 565-567.

[23] W.D. Nix, H. Gao, Indentation size effects in crystalline materials: a law for strain gradient plasticity, Journal of the Mechanics and Physics of Solids, 46 (1998) 411-425.

[24] N. Mukhopadhyay, P. Paufler, Micro-and nanoindentation techniques for mechanical characterisation of materials, International materials reviews, 51 (2006) 209-245.

[25] A.A. Elmustafa, D.S. Stone, Indentation size effect in polycrystalline F.C.C. metals, Acta Materialia, 50 (2002) 3641-3650.

[26] A.A. Elmustafa, D.S. Stone, Nanoindentation and the indentation size effect: Kinetics of deformation and strain gradient plasticity, Journal of the Mechanics and Physics of Solids, 51 (2003) 357-381.

[27] H. Gao, Y. Huang, W.D. Nix, Modeling Plasticity at the Micron Scale, Naturwissenschaften, 86 (1999) 507-515.

[28] P. Paufler, B. Wolf, Deformation of quasicrystals by indentation, in: H.-R. Trebin (Ed.) Quasicrystals, Wiley-VCH, Weinheim, 2003, pp. 501-522.

[29] J.G. Swadener, A. Misra, R.G. Hoagland, M. Nastasi, A mechanistic description of combined hardening and size effects, Scripta Materialia, 47 (2002) 343-348.

[30] T.T. Zhu, X.D. Hou, A.J. Bushby, D.J. Dunstan, Indentation size effect at the initiation of plasticity for ceramics and metals, Journal of Physics D: Applied Physics, 41 (2008) 074004(074001-074006).

[31] W.W. Gerberich, N.I. Tymiak, J.C. Grunlan, M.F. Horstemeyer, M.I. Baskes, Interpretations of indentation size effects, Journal of Applied Mechanics, 69 (2002) 433-442.

[32] S. Jang, Y. Purohit, D.L. Irving, C. Padgett, D. Brenner, R.O. Scattergood, Influence of Pb segregation on the deformation of nanocrystalline Al: Insights from molecular simulations, Acta Materialia, 56 (2008) 4750-4761.

[33] R.O. Scattergood, C.C. Koch, K.L. Murty, D. Brenner, Strengthening mechanisms in nanocrystalline alloys, Materials Science and Engineering: A, 493 (2008) 3-11.

[34] X. Liu, M.Q. Zeng, Y. Ma, M. Zhu, Melting behavior and the correlation of Sn distribution on hardness in a nanostructured Al–Sn alloy, Materials Science and Engineering: A, 506 (2009) 1-7.

[35] K.V. Rajulapati, R.O. Scattergood, K.L. Murty, Z. Horita, T.G. Langdon, C.C. Koch, Mechanical properties of bulk nanocrystalline aluminum-tungsten alloys, Metallurgical and Materials Transactions A, 39 (2008) 2528-2534.

[36] M.A. Atwater, D. Roy, K.A. Darling, B.G. Butler, R.O. Scattergood, C.C. Koch, The thermal stability of nanocrystalline copper cryogenically milled with tungsten, Materials Science and Engineering: A, 558 (2012) 226-233.

[37] S. Varam, P. Narayana, M.D. Prasad, D. Chakravarty, K.V. Rajulapati, K. Bhanu Sankara Rao, Strain rate sensitivity of bulk multi-phase nanocrystalline Al–W-based alloy, Philosophical Magazine Letters, 94 (2014) 582-591.

[38] W.C. Oliver, G.M. Pharr, An Improved Technique for Determining Hardness and Elastic Moduli using Load and Displacement Sensing Indentation Experiments, Journal of Materials Research, 7 (1992) 1564-1583.

[39] T.D. Shen, C.C. Koch, T.Y. Tsui, G.M. Pharr, On the elastic moduli of nanocrystalline Fe, Cu, Ni, and Cu–Ni alloys prepared by mechanical milling/alloying, Journal of Materials Research, 10 (1995) 2892-2896.

[40] Q. Wei, Z.L. Pan, X.L. Wu, B.E. Schuster, L.J. Kecskes, R.Z. Valiev, Microstructure and mechanical properties at different length scales and strain rates of nanocrystalline tantalum produced by high-pressure torsion, Acta Materialia, 59 (2011) 2423-2436.

[41] Z. Pan, Y. Li, Q. Wei, Tensile properties of nanocrystalline tantalum from molecular dynamics simulations, Acta Materialia, 56 (2008) 3470–3480.

[42] J.R. Trelewicz, C.A. Schuh, The Hall–Petch breakdown in nanocrystalline metals: A crossover to glass-like deformation, Acta Materialia, 55 (2007) 5948-5958.

[43] D. Tabor, The hardness and strength of metals, Journal Institute of Metals, 79 (1951) 1-18.

[44] A.C. Fisher-Cripps, Nanoindentation, Second Edition ed., Springer, New York, 2004.

[45] V. Maier, K. Durst, J. Mueller, B. Backes, H.W. Höppel, M. Göken, Nanoindentation strain-rate jump tests for determining the local strain-rate sensitivity in nanocrystalline Ni and ultrafine-grained Al, Journal of Materials Research, 26 (2011) 1421-1430.

[46] M. Ames, M. Grewer, C. Braun, R. Birringer, Nanocrystalline metals go ductile under shear deformation, Materials Science and Engineering: A, 546 (2012) 248-257.

[47] Q. Wei, S. Cheng, K.T. Ramesh, E. Ma, Effect of nanocrystalline and ultrafine grain sizes on the strain rate sensitivity and activation volume: fcc versus bcc metals, Materials Science and Engineering: A, 381 (2004) 71-79.

[48] Y.T. Zhu, X.Z. Liao, Nanostructured metals - Retaining ductility, Nature Materials, 3 (2004) 351–352.

[49] T. Zhu, J. Li, A. Samanta, H.G. Kim, S. Suresh, Interfacial plasticity governs strain rate sensitivity and ductility in nanostructured metals, Proc. Natl Acad. Sci., (2007) 3031–3036.

[50] R. Schwaiger, B. Moser, M. Dao, N. Chollacoop, S. Suresh, Some critical experiments on the strain-rate sensitivity of nanocrystalline nickel, Acta Materialia, 51 (2003) 5159-5172.

[51] J. May, H.W. Höppel, M. Göken, Strain rate sensitivity of ultrafine-grained aluminium processed by severe plastic deformation, Scripta Materialia, 53 (2005) 189-194.

[52] B. Ahn, R. Mitra, A. Hodge, E.J. Lavernia, S. Nutt, Strain rate sensitivity studies of cryomilled Al alloy performed by nanoindentation, in: Materials Science Forum, Trans Tech Publ, 2008, pp. 221-226.

[53] N.Q. Chinh, T. Csanádi, J. Gubicza, R.Z. Valiev, B.B. Straumal, T.G. Langdon, The effect of grain boundary sliding and strain rate sensitivity on the ductility of ultrafine-grained materials, Materials Science Forum, 667-669 (2011) 677-682.

[54] N.Q. Chinh, T. Csanádi, T. Győri, R.Z. Valiev, B.B. Straumal, M. Kawasaki, T.G. Langdon, Strain rate sensitivity studies in an ultrafine-grained Al–30 wt.% Zn alloy using micro- and nanoindentation, Materials Science and Engineering A, 543 (2012) 117-120.

[55] Y.M. Wang, E. Ma, Strain hardening, strain rate sensitivity, and ductility of nanostructured metals, Materials Science and Engineering: A, 375–377 (2004) 46-52.

[56] Q. Wei, Strain rate effects in the ultrafine grain and nanocrystalline regimes—influence on some constitutive responses, Journal of materials science, 42 (2007) 1709-1727.

[57] X.Z. Liao, F. Zhou, E.J. Lavernia, D.W. He, Y.T. Zhu, Deformation twins in nanocrystalline Al, Applied Physics Letters, 83 (2003) 5062-5064.

[58] M. Chen, E. Ma, K.J. Hemker, H. Sheng, Y. Wang, X. Cheng, Deformation twinning in nanocrystalline aluminum, Science, 300 (2003) 1275-1277.

[59] J.J. Niu, J.Y. Zhang, G. Liu, P. Zhang, S.Y. Lei, G.J. Zhang, J. Sun, Size-dependent deformation mechanisms and strain-rate sensitivity in nanostructured Cu/X (X=Cr, Zr) multilayer films, Acta Materialia, 60 (2012) 3677-3689.

[60] U.F. Kocks, A.S. Argon, M.F. Ashby, Thermodynamics and kinetics of slip, Progress in Materials Science, (1975) 1–281.

[61] X. Liao, F. Zhou, E. Lavernia, S. Srinivasan, M. Baskes, D. He, Y. Zhu, Deformation mechanism in nanocrystalline Al: Partial dislocation slip, Applied physics letters, 83 (2003) 632-634.

[62] Z. Shan, E.A. Stach, J.M.K. Wiezorek, J.A. Knapp, D.M. Follstaedt, S.X. Mao, Grain boundary-mediated plasticity in nanocrystalline nickel, Science, 305 (2004) 654-656.

[63] H. Van Swygenhoven, J.R. Weertman, Deformation in nanocrystalline metals, Materials Today, 9 (2006) 24-31.

Chapter 6 - Strain Rate Sensitivity of Nanocrystalline Al-W Alloy

6.1 Introduction

The research investigations that address the role of nano sized second phase particles on the mechanical behavior of nanostructured matrix with an average grain size less than 100 nm are very scarce as on today, despite some recent efforts [1-4]. Although the nanocrystalline (nc) materials exhibit high strength, their measured ductility has not been significant [5-8]. Therefore, for the adoption of these bulk nanomaterials in structural applications, they should possess both strength and ductility simultaneously. Koch [8] suggested that the incorporation of second phase particles in a nc matrix could simultaneously yield high strength and enhanced ductility. Zhu et al [9] points out, through their theoretical atomistic calculations, that plasticity at the interfaces dictates the strain rate sensitivity (SRS) and in turn influences the ductility in nanostructured materials. Therefore SRS could be taken as a controlling measure of ductility of nanostructured materials. Higher the value of SRS, more delayed will be the localised necking under tensile stress thus enhancing the ductility of the material. Hence a higher SRS value could qualitatively give a measure of ductility in nanostructured materials [10, 11]. If enough sample sizes are not available to perform mechanical testing as per ASTM standards to evaluate SRS, instrumented nanoindentation could be adopted to evaluate the SRS [11].

Wei et al [12] reported that nanostructured pure fcc metals have exhibited enhanced SRS, whereas the bcc metals have exhibited reduced SRS values in comparison to their coarse grained counterparts. However, the activation volume of fcc metals has decreased by two orders of magnitude and the activation volume of bcc metals remained constant. Although the SRS data of nc pure elements is available for various metals, SRS of nc two phase metallic systems is yet to

be systematically studied. Therefore in the current study, a nanocomposite with nc Al matrix (grain size ~ 40 nm) reinforced with nano sized $Al_{12}W$ particles synthesized using a combination of high energy ball milling and spark plasma sintering (SPS) is considered for further investigations. The microstructural study of this sintered nanocomposite by TEM as well as the mechanical characterization by microindentation and high load nanoindentation is carried out. SRS and activation volume are also calculated for this material. Scanning probe microscopy (SPM) image of the indent shows no presence of cracks and a plastically flown region is observed around the periphery of indent.

6.2 Materials and methods

Bulk nc Al-10at.%W alloy sample in spark plasma sintered condition was procured from PVSL Narayana, a former M Tech student. Initially the elemental powder of pure W (99.9% purity, Sigma-Aldrich, 12 µm particle size) was subjected to ball milling until a saturated grain size of 5 nm was obtained. Pure Al (99% purity, SD Fine Chemicals) powder along with the milled W powder was ball milled at room temperature for 50 h. Spark plasma sintering of compacted discs (10 mm in diameter, 3 mm thickness) was carried out at 748 K for 5 minutes with a heating rate of 6.22 K/s. The pressure applied was 50 MPa at a vacuum of 6 Pa and graphite dies were used. The rest of the experimental procedure is similar to the one described in Chapter 5.

6.3 Results and discussion

The earlier studies on Al-10at.%W nanocomposite [13] indicated that only two phase structure of Al and W is present at nano scale after ball milling. X-ray diffractograms of ball milled powder and sintered Al-10at.%W samples are shown in Figure 6.1 (adopted from [13]).

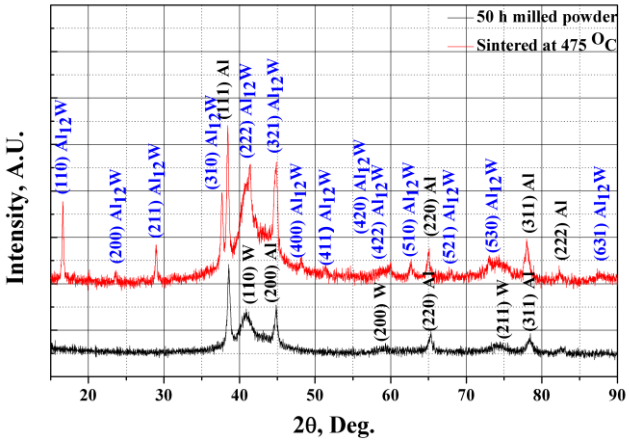

Figure 6.1 X-ray diffractograms of ball-milled and sintered Al-10 at.%W sample. SPS results in the evolution of nanocrystalline $Al_{12}W$ phase in nanocrystalline Al matrix (adopted from [13].

In as-milled condition, peaks corresponding to Al and W are only present. Crystallite size and precise lattice parameter were calculated by Williamson-Hall method [14] and Nelson-Riley extrapolation analysis [15] respectively. The saturated crystallite size of Al in ball milled powder sample was 33±3 nm and the precise lattice parameter of Al was 4.0475 ±0.0005Å. The crystallite size of W was 6 nm with a lattice parameter of 3.156±0.0004Å. This suggests that only two phase structure of Al and W is present at nano scale after ball milling. The ball milled powders were pre-compacted into 10 mm diameter disks at room temperature and are subsequently subjected to spark plasma sintering (SPS) at 748 K. The SPS of these samples yielded a density of 92% of the theoretical value (4.29 g/cc). The XRD pattern (Figure 6.1) of the SPS sample indicates that $Al_{12}W$ phase has precipitated out of nanocrystalline Al-W mixture during SPS. It is plausible that some amount of W is also retained as $Al_{12}W$ peaks and W peaks are very close at few locations, however the formation of $Al_{12}W$ is unambiguously clear from Figure 6.1. The obtained $Al_{12}W$ phase is of BCC structure and possesses a lattice parameter of 7.542±0.006Å. The lattice parameter of Al was measured to be 4.0452±0.0004Å. Therefore SPS of ball milled powders resulted in two-phase structure of Al and $Al_{12}W$ with nanocrystalline features. The microstructural features are shown in Fig. 6.2 (a) and (b) which represent the bright

field and dark field transmission electron micrographs of the sintered sample. The selected area diffraction pattern (SAD) as in the inset of Fig. 6.2 (b) shows concentric rings corresponding to Al, W as well as $Al_{12}W$. Fig. 6.2 (c) indicates the Al grain size distribution obtained from the dark field images. The size distribution of second phase particles (Fig. 6.2 (d)) is very broad with the presence of finer as well as larger particles with an average particle size of ~175 nm.

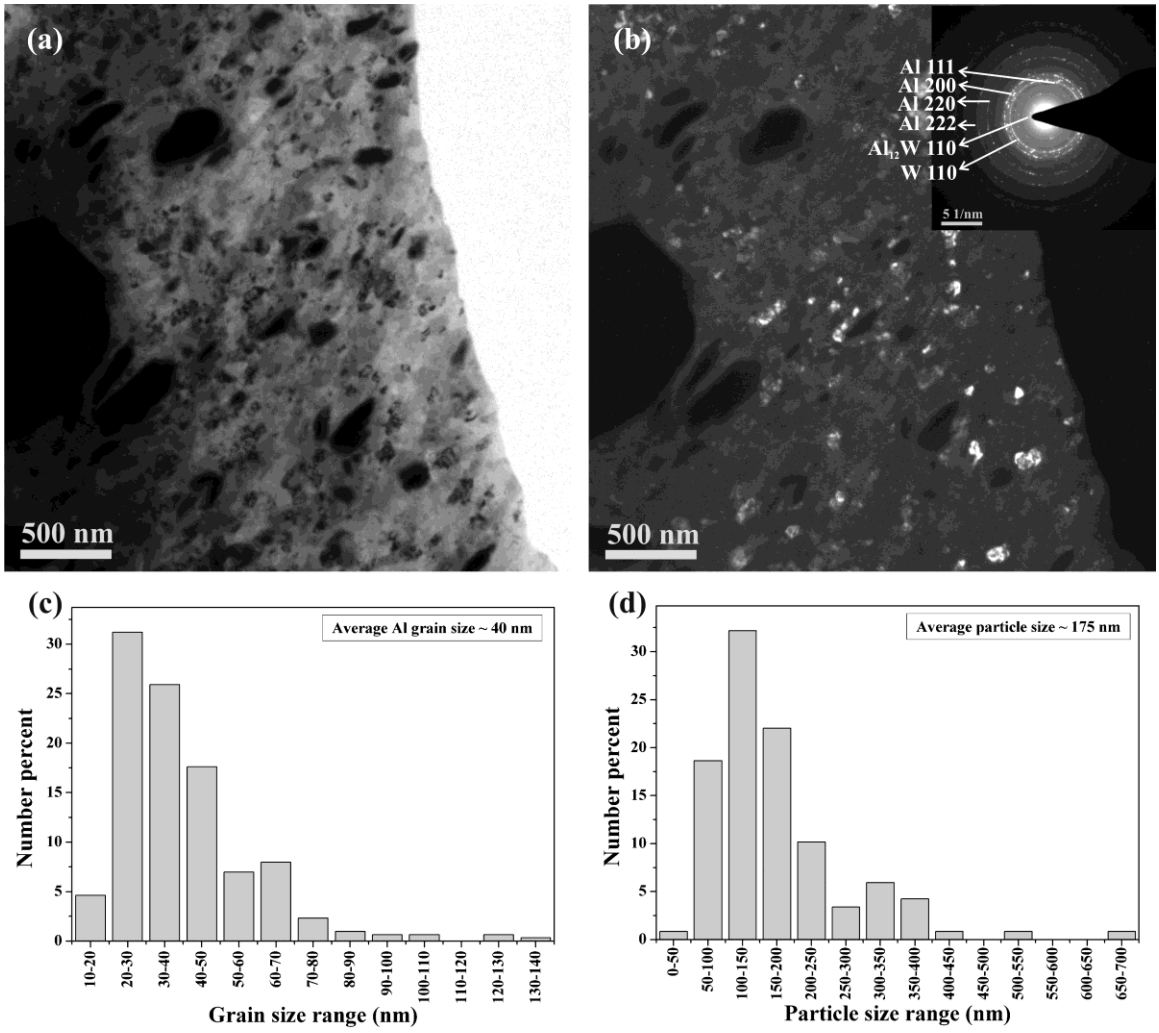

Fig. 6.2 (a) Bright-field and (b) dark-field transmission electron micrographs of nanocrystalline Al-10 at.%W composite along with the (c) Al grain size distribution obtained from dark-field image and (d) the particle size distribution of second-phase particles (darker in contrast in the bright-field image (a)).

Rajulapati et al [4] have earlier studied the processing and characterization of various nanocrystalline Al-W alloys prepared by high energy ball milling. The ball milled powders were

subsequently compacted using two methods, hot compaction at 573 K and high pressure torsion (HPT) at room temperature. However, in either of the cases, the two phase structure that was formed at nano scale during milling was not disturbed. There were several studies where attainment of nanocrystallinity resulted in the formation of stable/metastable phases as well as saturated/supersaturated solid solutions during ball milling [16, 17]. This was attributed to the presence of lattice imperfections in larger fractions aiding the inter-diffusivity among participating elements even at room temperature. However in case of Al-W [4], even the nanocrystallinity as well as the thermal activation provided by heating the samples to 573 K during hot compaction did not result in the formation of either compound or a solid solution. Since W is of higher melting point and thus of lower diffusivity at room temperature, initially its grain size was reduced to 5 nm and this was mixed to microcrystalline Al and were milled together in the present work. This was done mainly to observe if the nanocrystallinity of W and therefore its possibly high diffusivity would aid in the formation of any compound/solid solution or not. No compound/solid solution was formed after milling; however SPS of milled powders at 748 K resulted in the formation of $Al_{12}W$ in nc Al matrix.

The mechanical properties of the nanocomposite are measured using nanoindentation at room temperature at peak loads of 6000 and 8000 μN with varying loading rates. The hardness has varied between 5.0-5.7 GPa (Fig. 6.3 (a) adopted from [13]). This high hardness could be due to a) nc Al matrix with a grain size of ~40 nm, b) homogeneous distribution of nc $Al_{12}W$ phase with a particle size of 175 nm. Although the distribution of $Al_{12}W$ particles (Fig. 6.2 (d)) is broad, it is believed that the smaller particles contribute significantly towards the improvement of hardness via Orowan strengthening [4]. If the particle size is less than that of the matrix grain size and particles are present within the grain, then these particles are expected to contribute to

the overall strength of the material via the Orowan strengthening mechanism. If the particles are much bigger than the matrix grain size, then it is expected that these larger particles contribute through composite-type strengthening via either the rule of mixtures or the inverse rule of mixtures. It is also to be noted that these larger particles will have a lower contribution to the overall strength of the material [4].

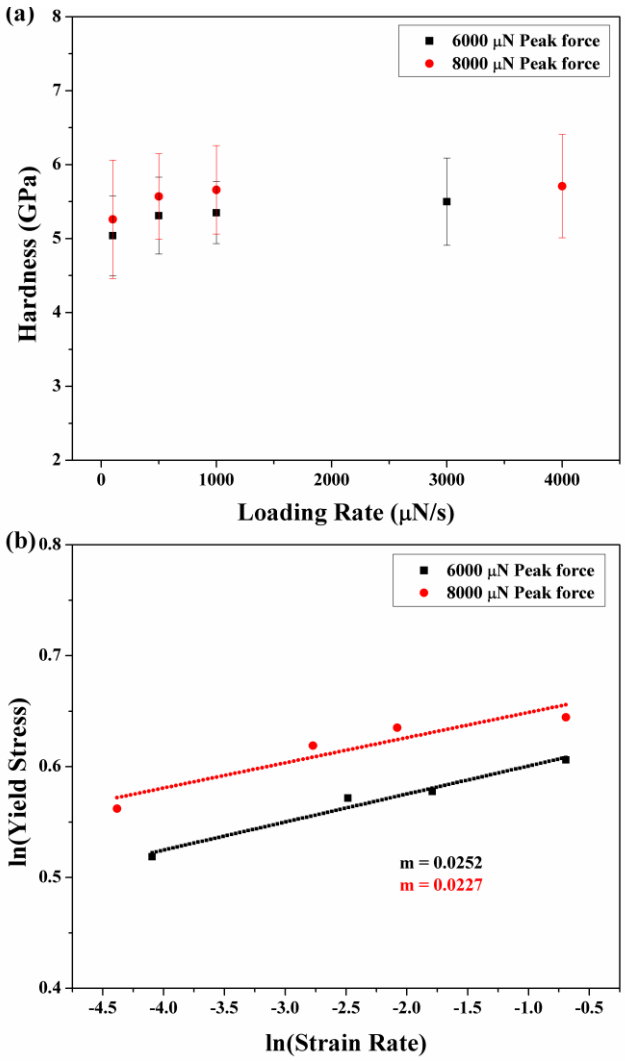

Fig. 6.3 (a) Variation of hardness with loading rate at different peak loads and (b) ln(Stress) versus ln(Strain rate) plot for nanocrystalline Al–$Al_{12}W$ composite obtained using nanoindentation data (adopted from [13]).

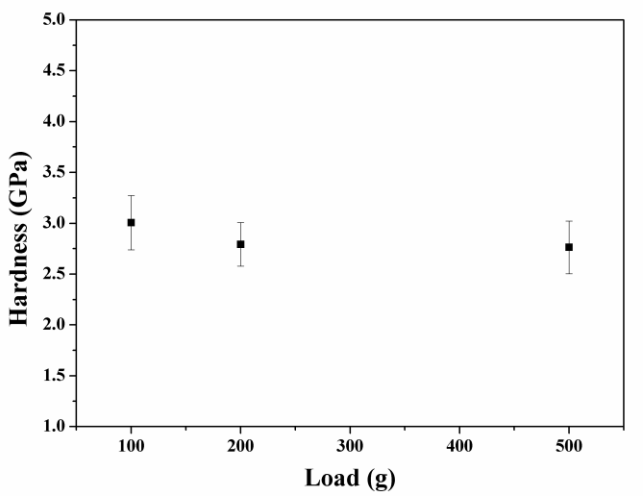

Fig. 6.4 Microhardness of Al-10at.%W nanocomposite with varying applied loads.

The elastic modulus of this nanocomposite was measured to be 145±5 GPa. Nanoindentation has also been carried out at higher load of 1000 mN with different loading rates of 10 mN/s, 50 mN/s, 200 mN/s & 1000 mN/s and an average hardness value of 3.18 GPa was obtained. The average hardness obtained from microindentation is ~ 3 GPa (Fig. 6.4) which is in good agreement with the high load nanoindentation data. The difference in the hardness values of low load nanoindentation and microindentation as well as high load nanoindentation could be possibly due to indentation size effect (ISE) as discussed in detail in Chapter 5 Section 5.2.2 [18, 19].

Feng et al [20] fabricated in-situ Al-$Al_{12}W$ composites using reaction sintering and studied their mechanical behavior. They observed that the strength of the composite has increased because of the reinforcing $Al_{12}W$ particles and observed a ductility of 7.3%. Lee et al [21] developed Al-W based composites using ball milling and reactive hot pressing. They have reported a hardness of about 1 GPa and an elastic modulus of 85-90 GPa. The Al-$Al_{12}W$ nanocomposite synthesized in the current investigation has a nanohardness of 5.4 GPa and an elastic modulus of 145 GPa suggesting that the material in the current study possesses superior

mechanical properties. Except for the studies reported in references [20, 21], to the authors' knowledge, no other study was reported on mechanical behavior of Al-$Al_{12}W$ composites with either microcrystalline/nanocrystalline features.

Hsu et al [22] reported the mechanical properties of Al-Al_3Ti nanocomposites processed by friction stir processing. However their aluminum matrix grain size is in ultrafine regime although the reinforcement size is below 100 nm. They have observed higher yield strength (684±73 MPa) in compression with loss of ductility as the Ti content is increased. They attributed this to the presence of larger fraction of Al_3Ti particles which are brittle in nature. Liu et al [23] fabricated Al-AlN nanocomposites with both the grain size of the matrix and reinforcement particle size in nano regime. They reported a hardness of 3.48 GPa for the composite with 39 vol. % of AlN. Sasaki et al [24] have reported high compressive yield strength of 1 GPa in multiphase bulk Al-Fe alloy, processed by mechanical alloying and SPS, containing microcrystalline Al, nanocrystalline Al and Al_3Fe phase. Therefore, in comparison to the studies on both microcrystalline and nc Al matrix composites reinforced with various intermetallic particles discussed above, the multiphase Al-10at.%W nanocomposite showed superior hardness of about 5.4 GPa and a high elastic modulus of 145 GPa using nanoindentation studies.

Tabor [25] suggested that dividing the hardness with a factor of 3 would approximately give the yield strength of the material. Following this approach, the hardness values are converted to their respective yield stresses. Strain rate is obtained by dividing the loading rate with the peak load. A plot was made with ln (yield stress) as ordinate and ln (strain rate) as abscissa and is shown in Fig. 6.3 (b) (adopted from [13]). The corresponding linear fits are also shown in Fig. 6.3 (b) and the slope of this line gives the strain rate sensitivity. The nanoindentation was carried out at different peak forces which mean different indentation depths. As the indentation depth

increases, the volume of the material being deformed also increases. This gives more reasonable and bulk mechanical behaviour of the nanocomposite which involves the deformation of larger number of nanocrystalline grains and larger fraction of second phase particles. From Fig. 6.3 (b) it is clear that, at different peak loads, the measured SRS value is 0.024±0.001 which indicates that although the indentation depth is changed, SRS is not getting influenced. This confirms the homogeneous nature of the nanocomposite in the present investigation.

Several researchers have reported that many nc metals exhibit loading rate / strain rate sensitivity [26-31]. Single phase fcc metals showed enhanced SRS whereas the bcc metals showed reduced SRS in comparison to their respective coarse grained counterparts. Studies on nc Al-Pb alloys [32] showed increase in SRS with increasing amount of Pb to Al. At room temperature, SRS values of 0.036 and 0.1 are obtained for nc Al and Al-4at.%Pb respectively. Here, Al and Pb are of both fcc crystal structure, where as in the current investigation on Al-W alloy, W is of bcc crystal structure. Slight reduction in SRS to a value of 0.024±0.001 in comparison to that of nc Al can be explained based on fcc-bcc combination of Al and W as bcc systems possess limited ductility. The slope of the plot between kT ln (strain rate) and yield stress gives the activation volume involved in the deformation process and it is calculated for various peak loads. The activation volume varied between 3.78-3.88 b^3 (where b is the Burgers vector of Al) as the peak load varied from 6000 µN to 8000 µN. The measured activation volume is in the same range reported for other nc metals [33]. This low activation volume suggests that the deformation characteristics are not governed by the dislocations and interfaces (grain boundaries in both the matrix and reinforcement, triple junctions in both the matrix and reinforcement, matrix/particle interfaces etc.) might be playing a critical role in the plasticity in this case. Asaro and Suresh [33] have compiled both SRS and activation volume data of Cu and

Ni. Their compilation suggests that as the grain size is decreased to ≤ 100 nm, the SRS increases and the activation volume decreases. Fig. 6.5 (a) shows the SPM image of an indent scanned using the Berkovich tip immediately after the nanoindentation test and the corresponding line profile is also shown in Fig. 6.5 (b). It is clear that there exists a plastically flown region (white contrast) around periphery of the indent. Therefore it can be concluded that a high SRS value could be a qualitative indication of ductility possessed by a nanostructured material. This conclusion is also in agreement with other studies where both higher SRS value and ductility are observed simultaneously [34-36].

Although nc materials exhibit fascinating mechanical properties, the underlying deformation mechanisms are yet to be unfolded in a systematic and unambiguous manner.

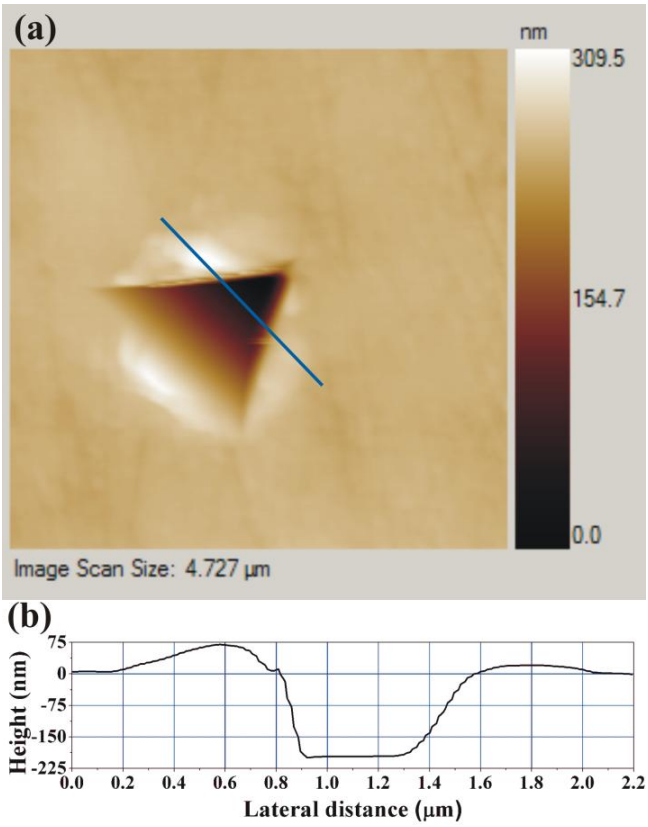

Fig. 6.5 Scanning probe microscopic image of the indent showing plasticity around the indent. The corresponding line profile is also shown.

As the grain size is decreased to nano regime, the role of dislocations in governing the plasticity becomes insignificant and grain boundaries and other interfaces are expected to take a lead role in dictating the deformation characteristics at nano scale. A major insight into the deformation mechanisms so far was provided by Molecular Dynamics simulations [37]. These nc materials are believed to deform by the following mechanisms a) grain boundary sliding b) grain rotation and coalescence and c) grain boundaries acting as sources as well as sinks for lattice imperfections (full dislocations/partial dislocations/stacking faults etc.) [7]. In addition if a nano scale second phase is present, its size, volume fraction, distribution and the matrix/particle interface will also contribute to the plastic deformation. Therefore, based on this discussion, it is expected that in the present study the Al matrix with a grain size of 40 nm, nano sized $Al_{12}W$ particles and their distribution are responsible for the observed mechanical properties with high hardness, high elastic modulus and enhanced SRS. The interfacial regions viz., grain boundaries in the matrix and reinforcement, triple junctions in the matrix and the reinforcement, matrix/particle boundaries etc. might be playing a crucial role in influencing the SRS and activation volume in the present study.

6.4 Summary and conclusions

Spark plasma sintered bulk nc Al-10at.%W nanocomposite sample was structurally and mechanically characterized to understand the mechanical behavior. Transmission electron micrographs revealed that the nanocrystalline intermetallic $Al_{12}W$ phase with an average particle size of 175 nm is uniformly distributed in the nc Al matrix with a grain size of 40 nm. The nanoindentation studies on this novel nanocomposite yielded an average hardness value of 5.4 GPa and an elastic modulus of 145 GPa. A SRS value of 0.024±0.001 was measured with a very low activation volume of 3.78-3.88 b^3 as the peak load varied from 6000 µN to 8000 µN. Slight

reduction in SRS value of Al-W alloy when compared to that of nc Al (0.036) is due to the addition of bcc W to Al. An average hardness value of 3.18 GPa was obtained from nanoindentation carried out by applying a high load of 1000 mN. The average hardness obtained from microindentation is ~3.1 GPa which is in good agreement with the high load nanoindentation data. The difference in the hardness values of low load nanoindentation and microindentation could be possibly due to indentation size effect. The superior mechanical properties of this nanocomposite could be because of an aluminum matrix with a grain size of 40 nm, a nanocrystalline second phase ($Al_{12}W$) with nanocrystalline features and its uniform distribution throughout the matrix. It is also expected that finer $Al_{12}W$ particles might be contributing significantly through Orowan strengthening to the enhanced mechanical properties. The interfacial regions viz., grain boundaries in the matrix and reinforcement, triple junctions in the matrix and the reinforcement, matrix/particle boundaries etc. could be governing the SRS and activation volume of multi-phase nc Al-10at.%W composite in this investigation. The scanning probe microscopic image of the indent shows a plastically flown region around the periphery.

References

[1] C.C. Koch, R.O. Scattergood, K.L. Murty, The Mechanical Behavior of Multiphase Nanocrystalline Materials, JOM, 59 (2007) 66-70.

[2] R.O. Scattergood, C.C. Koch, K.L. Murty, D. Brenner, Strengthening mechanisms in nanocrystalline alloys, Materials Science and Engineering: A, 493 (2008) 3-11.

[3] K.V. Rajulapati, R.O. Scattergood, K.L. Murty, G. Duscher, C.C. Koch, Effect of Pb on the mechanical properties of nanocrystalline Al, Scripta Materialia, 55 (2006) 155-158.

[4] K.V. Rajulapati, R.O. Scattergood, K.L. Murty, Z. Horita, T.G. Langdon, C.C. Koch, Mechanical properties of bulk nanocrystalline aluminum-tungsten alloys, Metallurgical and Materials Transactions A, 39 (2008) 2528-2534.

[5] C.C. Koch, D.G. Morris, K. Lu, A. Inoue, Ductility of nanostructured materials, MRS Bulletine, 24 (1999) 54-58.

[6] K.S. Kumar, H. Van Swygenhoven, S. Suresh, Mechanical behavior of nanocrystalline metals and alloys, Acta Materialia, 51 (2003) 5743-5774.

[7] M.A. Meyers, A. Mishra, D.J. Benson, Mechanical properties of nanocrystalline materials, Progress in Materials Science, 51 (2006) 427-556.

[8] C.C. Koch, Optimization of strength and ductility in nanocrystalline and ultrafine grained metals, Scripta Materialia, 49 (2003) 657-662.

[9] T. Zhu, J. Li, A. Samanta, H.G. Kim, S. Suresh, Interfacial plasticity governs strain rate sensitivity and ductility in nanostructured metals, Proc. Natl Acad. Sci., (2007) 3031–3036.

[10] Y.T. Zhu, X.Z. Liao, Nanostructured metals - Retaining ductility, Nature Materials, 3 (2004) 351–352.

[11] S. Varam, K.V. Rajulapati, K. Bhanu Sankara Rao, Strain rate sensitivity studies on bulk nanocrystalline aluminium by nanoindentation, Journal of Alloys and Compounds, 585 (2014) 795-799.

[12] Q. Wei, S. Cheng, K.T. Ramesh, E. Ma, Effect of nanocrystalline and ultrafine grain sizes on the strain rate sensitivity and activation volume: fcc versus bcc metals, Materials Science and Engineering: A, 381 (2004) 71-79.

[13] P.V.S.L. Narayana, Synthesis and Mechanical Behavior of Al-W Nanocomposites, in: School of Engineering Sciences and Technology, University of Hyderabad, Hyderabad, India, 2013, pp. 107.

[14] G.K. Williamson, W.H. Hall, X-ray line broadening from filed aluminium and wolfram, Acta Metallurgica, 1 (1953) 22-31.

[15] B.D. Cullity, Elements of X-ray Diffraction, Addison-Wesley Publishing Company, Inc., Reading, Massachusetts, 1956.

[16] C. Suryanarayana, Nanocrystalline materials, International Materials Reviews, 40 (1995) 41-64.

[17] B.S. Murty, S. Ranganathan, Novel materials synthesis by mechanical alloying/milling, International materials reviews, 43 (1998) 101-141.

[18] N. Mukhopadhyay, P. Paufler, Micro-and nanoindentation techniques for mechanical characterisation of materials, International materials reviews, 51 (2006) 209-245.

[19] T.T. Zhu, X.D. Hou, A.J. Bushby, D.J. Dunstan, Indentation size effect at the initiation of plasticity for ceramics and metals, Journal of Physics D: Applied Physics, 41 (2008) 074004(074001-074006).

[20] Y.C. Feng, L. Geng, A.B. Li, Z.Z. Zheng, Fabrication and characteristics of< i> in situ</i> Al12W particles reinforced aluminum matrix composites by reaction sintering, Materials & Design, 31 (2010) 965-967.

[21] H.B. Lee, H. Tezuka, E. Kobayashi, T. Sato, K.D. Woo, Fabrication and Mechanical Properties of Al-Based In Situ Nano-Composites Reinforced by Al2O3 and Intermetallic Compounds, Materials Transactions, 53 (2012) 428-434.

[22] C.J. Hsu, C.Y. Chang, P.W. Kao, N.J. Ho, C.P. Chang, Al–Al3Ti nanocomposites produced in situ by friction stir processing, Acta Materialia, 54 (2006) 5241-5249.

[23] Y.Q. Liu, H.T. Cong, W. Wang, C.H. Sun, H.M. Cheng, AlN nanoparticle-reinforced nanocrystalline Al matrix composites: Fabrication and mechanical properties, Materials Science and Engineering: A, 505 (2009) 151-156.

[24] T.T. Sasaki, T. Mukai, K. Hono, A high-strength bulk nanocrystalline Al–Fe alloy processed by mechanical alloying and spark plasma sintering, Scripta Materialia, 57 (2007) 189-192.

[25] D. Tabor, The hardness and strength of metals, Journal Institute of Metals, 79 (1951) 1-18.

[26] Y.M. Wang, E. Ma, Strain hardening, strain rate sensitivity, and ductility of nanostructured metals, Materials Science and Engineering: A, 375–377 (2004) 46-52.

[27] L. Lu, S.X. Li, K. Lu, An abnormal strain rate effect on tensile behavior in nanocrystalline copper, Scripta Materialia, 45 (2001) 1163–1169.

[28] Q. Wei, Z.L. Pan, X.L. Wu, B.E. Schuster, L.J. Kecskes, R.Z. Valiev, Microstructure and mechanical properties at different length scales and strain rates of nanocrystalline tantalum produced by high-pressure torsion, Acta Materialia, 59 (2011) 2423-2436.

[29] Z. Pan, Y. Li, Q. Wei, Tensile properties of nanocrystalline tantalum from molecular dynamics simulations, Acta Materialia, 56 (2008) 3470–3480.

[30] S. Cheng, E. Ma, Y.M. Wang, L.J. Kecskes, K.M. Youssef, C.C. Koch, U.P. Trociewitz, K. Han, Tensile properties of in situ consolidated nanocrystalline Cu, Acta Materialia, 53 (2005) 1521-1533.

[31] Y. Wei, A.F. Bower, H. Gao, Enhanced strain-rate sensitivity in fcc nanocrystals due to grain-boundary diffusion and sliding, Acta Materialia, 56 (2008) 1741-1752.

[32] S. Varam, K.V. Rajulapati, K.B.S. Rao, R.O. Scattergood, K.L. Murty, C.C. Koch, Loading Rate-Dependent Mechanical Properties of Bulk Two-Phase Nanocrystalline Al-Pb Alloys Studied by Nanoindentation, Metallurgical and Materials Transactions A, 45 (2014) 5249-5258.

[33] R.J. Asaro, S. Suresh, Mechanistic models for the activation volume and rate sensitivity in metals with nanocrystalline grains and nano-scale twins, Acta Materialia, 53 (2005) 3369-3382.

[34] N.Q. Chinh, T. Csanádi, J. Gubicza, R.Z. Valiev, B.B. Straumal, T.G. Langdon, The effect of grain boundary sliding and strain rate sensitivity on the ductility of ultrafine-grained materials, Materials Science Forum, 667-669 (2011) 677-682.

[35] N.Q. Chinh, T. Csanádi, T. Győri, R.Z. Valiev, B.B. Straumal, M. Kawasaki, T.G. Langdon, Strain rate sensitivity studies in an ultrafine-grained Al–30 wt.% Zn alloy using micro- and nanoindentation, Materials Science and Engineering A, 543 (2012) 117-120.

[36] R.Z. Valiev, I.V. Alexandrov, Y.T. Zhu, T.C. Lowe, Paradox of strength and ductility in metals processed by severe plastic deformation, Journal of Materials Research, 17 (2002) 5-8.

[37] H. Van Swygenhoven, P.M. Derlet, Hasnaoui, Atomic mechanism for dislocation emission from nanosized grain boundaries, Phys. Rev. B, 66 (2002) 024101.

Chapter 7 – Strain Rate Sensitivity and Modulus Mapping of *In-situ* Consolidated Nanocrystalline Al-Pb-W Alloy

7.1 Introduction

Recently there has been a great interest in understanding the deformation characteristics of nanocrystalline (nc) materials [1-3]. The processing techniques that are being used to prepare nanocrystalline/ultra-fine grained materials either give relatively larger samples with relatively coarser microstructural features (for example SPD techniques) [4] or smaller samples with finer microstructural features [5]. Fabricating bulk samples with finer microstructural features, for a reasonable measurement of bulk mechanical behavior, is still an uphill task. Ball milling is known to yield powders with finer microstructural features but making bulk samples out of these powders with the same "as-synthesized" finer microstructural features hasn't been possible to a larger extent needed, despite some success in few metals and alloys [5]. Therefore in the current study, powders of Al-1at.%Pb-1at.%W are consolidated in-situ during milling itself thus avoiding an additional step of post-synthesis compaction.

Although there have been several reports on mechanical behavior of nc elemental metals most precisely the loading rate/strain rate dependence of flow stress [6-23], similar investigations on multi-phase nc metals need immediate attention from the scientific community. Strain rate sensitivity (SRS) and activation volume are two important parameters that describe the strain rate dependence of flow stress. It was documented that, in elemental metals with nano scale microstructural features, SRS has increased in comparison to their coarse grained counterparts in case of fcc metals whereas SRS decreased in case of nc bcc metals [6, 7]. However activation volume of nc metals measured so far was several orders of magnitude less than that of coarse grained metals [6-8]. Our recent investigation suggests that an addition of nc fcc Pb phase to nc

fcc Al matrix increases the SRS [24] and an addition of nc bcc W phase slightly decreases the SRS of overall composite material [25] with nano scale microstructural entities. Therefore to understand the simultaneous effect of nc Pb phase and nc W phase on the overall SRS and activation volume of nc Al matrix, Al-1Pb-1W nanocomposite was synthesized using ball milling and these flow parameters are evaluated using nanoindentation at room temperature.

7.2 Materials and methods

Nanocrystalline Al-1at.%Pb-1at.%W alloy was synthesized using high energy ball milling at room temperature. The experimental procedure is similar to that given in Chapter 5. The Al powder (99.0% purity, +200 mesh, S-D Fine Chemicals Limited), Pb powder (99.9% purity, Alfa Aesar, -200 mesh) and W powder (99.9% purity, Alfa Aesar, -200 mesh) were used as initial powders for milling. Process controlling agent was not added to aid in *in situ* consolidation of the powder particles during milling operation which resulted in the formation of irregular shaped chunks of materials having varying sizes from 2 mm to 6 mm. These chunks were pressed into 6 mm diameter disks by applying a uni-axial pressure of 1.5 GPa at room temperature. The density of the compacted disk was measured using Archimedes principle and ~ 99% density was achieved.

7.3 Results and discussion

Nanocrystalline Al-1Pb-1W alloy synthesized *in-situ* using high energy ball milling resulted in the formation of irregular shaped chunks of material having varying sizes from 2 mm to 6 mm (Fig. 7.1). The smaller balls are compacted into 6 mm diameter discs (Fig. 7.1 (d)). The X-ray diffractograms of milled Al-Pb-W alloy powders (Fig. 7.2 (a)) indicated peaks corresponding to individual elements of Al, Pb and W.

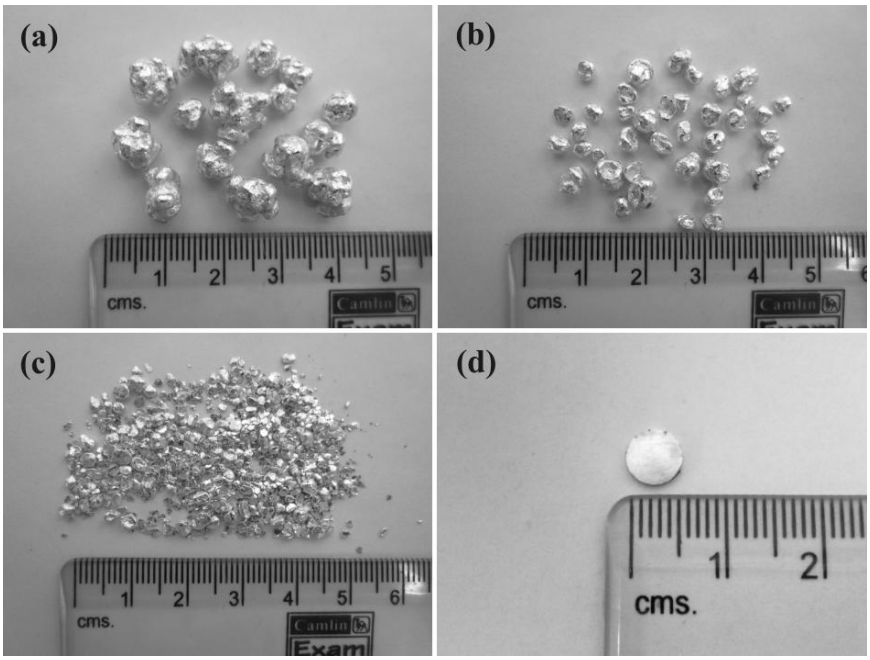

Fig. 7.1 Nanocrystalline Al-Pb-W alloy synthesized by in-situ consolidation ball milling (a), (b), (c) balls of varying sizes formed during milling and (d) compacted disc of 6 mm diameter.

The broadening of peaks was observed with increasing milling time indicating the finer microstructural features. Fig. 7.2 (b) shows the X-ray diffractogram of compacted disc. It is clear from the figure that mechanical alloying did not result in the formation of any solid solution or a compound. The precise lattice parameter value of Al matrix calculated using Nelson-Riley extrapolation function is 4.0468±0.0001 Å which is in good agreement with the standard value of 4.0495 Å.

Microstructural details are investigated by TEM and the micrographs revealed very fine grained structure as in Fig. 7.3. Fig. 7.3 (a) represents the bright filed image, Fig. 7.3 (b) represents the dark field image and the corresponding selected area diffraction (SAD) pattern is shown in Fig. 7.3 (c). The SAD pattern showed rings corresponding to Al, Pb and W. Average grain size calculated from various TEM micrographs using linear intercept method is about 23 (±12) nm. The grain size distribution plot is shown in Fig. 7.4. The smaller grain size obtained

for Al-Pb-W alloy when compared to that of Al-Pb alloy (~ 45 nm) from our recent studies [24] could be due to the addition of W as alloying element. Generally, the minimum grain size obtainable during mechanical milling / mechanical alloying of powders depends on the competition between the plastic deformation and the recovery processes. The addition of alloying elements to pure metals greatly influences the final grain size of the powders. In multi-component systems, the microstructural evolution depends on the mechanical behavior of its component powders.

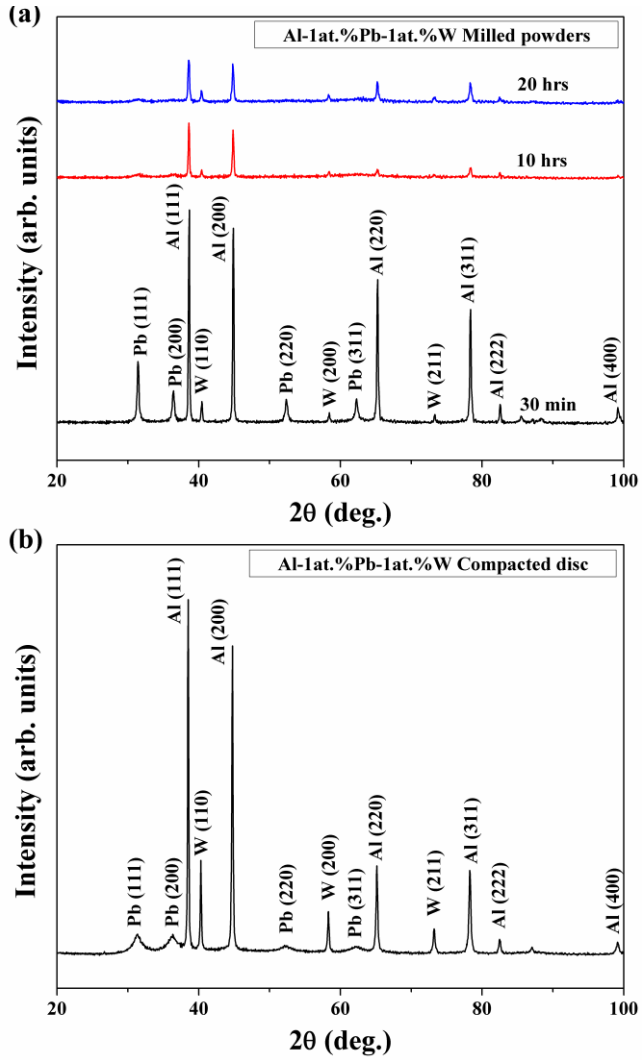

Fig. 7.2 (a) X-ray diffractograms of milled Al-1at.%Pb-1at.%W alloy powders, (b) X-ray diffractogram of the compacted disc.

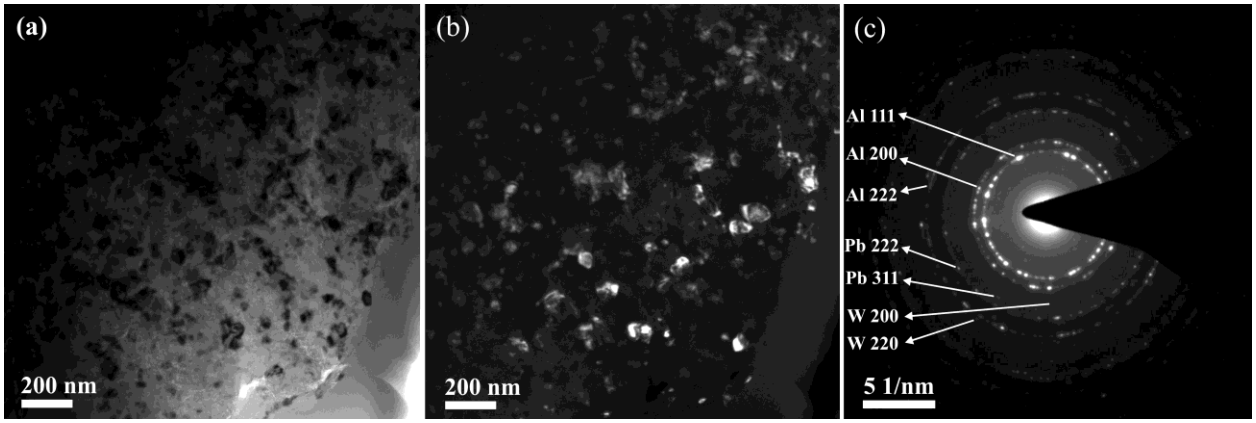

Fig. 7.3 (a) Bright field and (b) dark field transmission electron micrographs and (c) indexed SAD pattern of in-situ consolidated nanocrystalline Al-Pb-W alloy.

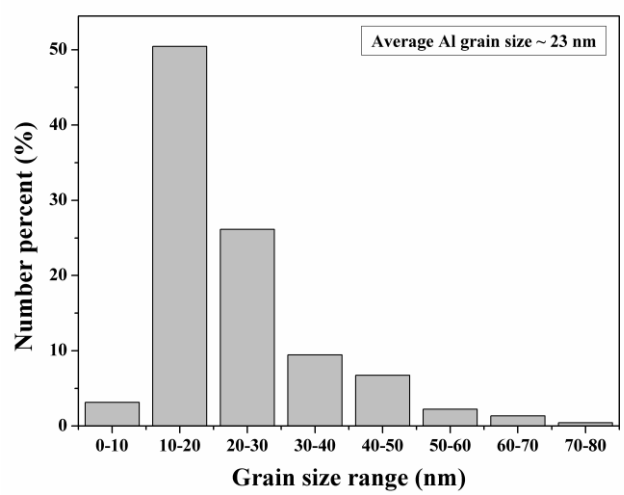

Fig. 7.4 Grain size distribution of Al grains obtained from dark-field TEM micrographs having an average grain size of ~23 nm.

Here, Al-Pb-W is fcc-fcc-bcc combination where Al, Pb are ductile in nature and tungsten is brittle and the presence of tungsten seems to have been resulted in effective milling.

High resolution TEM micrographs are shown in Fig. 7.5 which indicate the formation of faceted Pb particles in Al matrix and similar microstructural features were also observed in several earlier studies [26, 27]. Dahmen et al. [26] have reported that the shapes of Pb inclusions in Al matrix are dependent on the size of the inclusion. They carried out high resolution TEM studies on 100 nm thick Al thin films into which nanosized Pb inclusions were ion implanted. Due to overlapping of the lattice planes of the matrix and the inclusion, Moiré contrast effect was

observed. The authors concluded that when the residual strain energy is negligible, the inclusions tend to form spherical or cuboctahedral shapes and when the strain energy is high the inclusions tend to form irregular faceted polyhedron. Investigations have been carried out by Mizoguchi et al. [27] on the shapes of nanoscale Pb inclusions in the Al matrix using TEM tomography and high-angle annular dark field, scanning transmission electron microscopy (HAADF-STEM). They found that the shapes of Pb inclusions at Al grain boundary were more complex and compound shapes were formed. The Pb inclusions appeared rounded toward one grain and faceted toward another grain. Moiré fringes were also observed at specific tilt angles. In the present work, the faceted inclusions are observed in ball milled and compacted sample when examined by high resolution TEM (Fig. 7.5). These complex shaped inclusions are expected to significantly influence the mechanical properties of the Al matrix. In the present work, the average size of Pb particles was found to be ~ 5 nm.

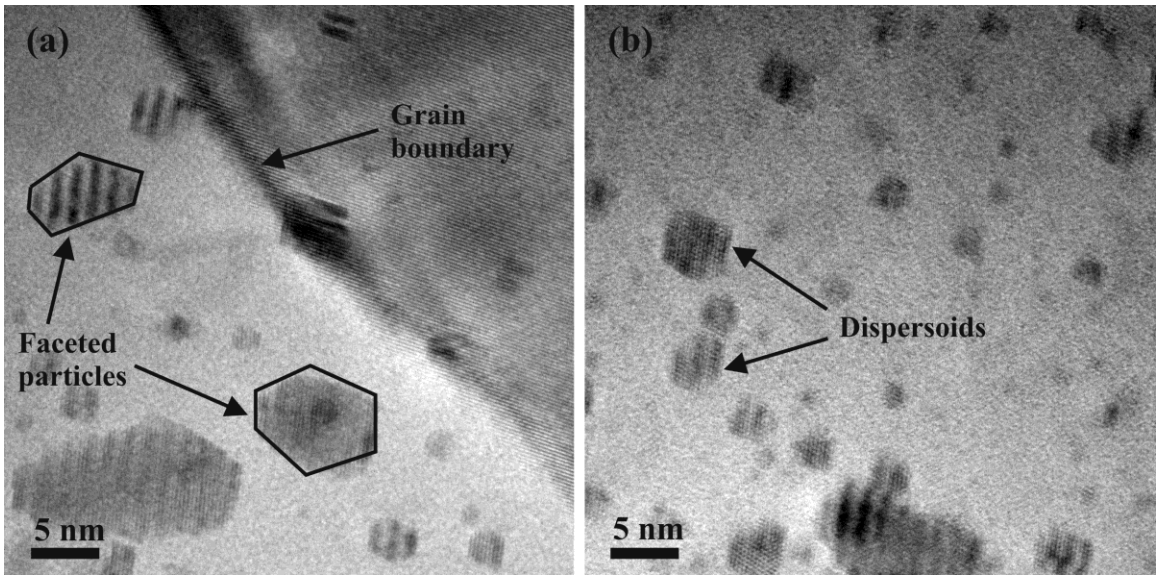

Fig. 7.5 High resolution transmission electron micrographs ((a) and (b)) of in-situ consolidated nanocrystalline Al-Pb-W alloy showing the second phase particles having an average size of ~ 5 nm.

The Pb particles were present within the grains and along the grain boundaries as well, as shown in Fig. 7.5 (a). Since there is a large variation in the elastic moduli of Al (70 GPa), Pb (16 GPa)

and W (411 GPa), modulus mapping studies using Berkovich tip in nanoindentation have been performed to understand the distribution of W phase in the Al matrix. The corresponding details are discussed in the following sections.

Mechanical properties of the compacted disc are evaluated using Vickers microindentation and a depth sensing nanoindentation. Microhardness measurements carried out at various loads ranging from 50 g to 200 g showed that the hardness is independent of applied load (Fig. 7.6 (a)). For comparison purpose, microhardness data of nc Al obtained at various loads [28] is also included in (Fig. 7.6 (a)). Indentation size effect (ISE) [29-32] was observed in case of nc Al whereas the ISE is not observed in nc Al-Pb-W alloy. A microhardness value of ~ 1 GPa was obtained for the bulk Al-Pb-W alloy sample having Al matrix grain size of ~23 nm whereas nc Al fabricated by ball milling (~42 nm) and cold compaction showed slightly higher hardness values (1.29±0.04 GPa and 1.15±0.04 GPa at 50 g and 200 g respectively). The segregation of alloying elements at the grain boundaries is expected to be more when the matrix grain size is low (~23 nm in the current case) because of the larger volume fractions of grain boundary other interfacial regions at such a smaller grain size [33, 34]. Hence the grain boundary mediated deformation processes are expected to dominate in this material. This could be the reason for softening of the Al matrix with Pb and W addition. The second phase is expected to segregate to the grain boundaries initially [24, 35, 36]. Once the grain boundaries are saturated, the excess phase will be present inside the grains as particles.

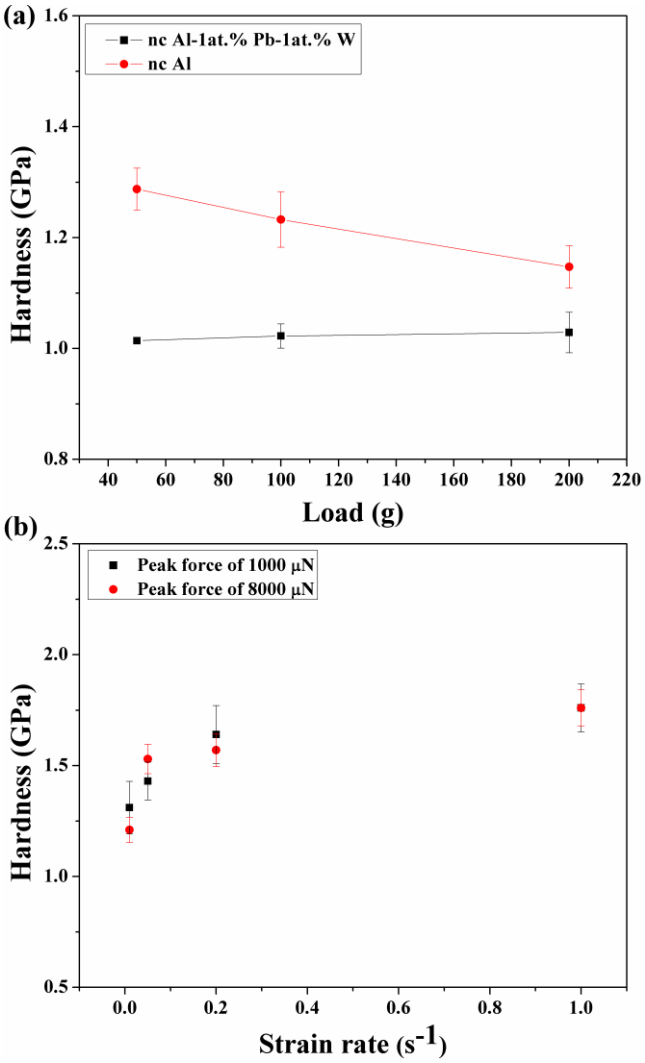

Fig. 7.6 (a) Microhardness data of nanocrystalline Al-Pb-W alloy, hardness data of nanocrystalline Al is also shown for comparision purpose (b) hardness vs strain rate data obtained from nanoindentation at two different peak forces of 1000 µN and 8000 µN.

At this grain size of the matrix, as it was reported by both theoretical [34] and experimental [35] means, the grain boundary phase will soften the matrix whereas the particles present inside the matrix grain will increase the strength by Orowan particle strengthening mechanism [24, 36] in these nc materials. Therefore the overall strength of the alloy is dictated by the competition between grain boundary weakening mechanism and particle strengthening mechanism. It was observed in our earlier studies as well as the current study that Pb is segregated to grain boundaries [24, 34, 35] whereas the presence of W phase is not observed in the grain boundaries

(Fig. 7.5 (a) of this study) [36] of nc Al matrix. Hence Pb phase would either contribute to weakening if it is present in the grain boundaries [34, 35] or to strengthening if it is present in the matrix as dispersions [24, 37]. It is expected that W would only contribute to strengthening based on our earlier investigations [36] as well as current study. This argument is also in agreement with the strengthening effects observed in Cu [38] and Ni [39] due to the presence of W phase.

The hardness data obtained from nanoindentation at two different peak forces of 1000 µN and 8000 µN by varying the loading rates is represented in Fig. 7.6 (b). It is evident that as the strain rate is increased, the hardness has also increased at both the peak loads suggesting a positive SRS value. As the peak load is increased, indentation depth also increases thus sampling large volume of the sample representing the bulk behavior.

Al-Pb-W bulk sample showed an average elastic modulus value of ~ 90 (± 8) GPa from indentation tests. In order to study the distribution of dispersions in Al matrix, modulus mapping studies have been carried out on the bulk sample using a nano indenter in a manner similar to our earlier studies [40]. Dynamic force is applied on the sample to obtain the modulus map while the sample surface is scanned by a probe in raster mode. During a modulus map test, *in situ* image is obtained while the dynamic test is in progress. The complex modulus (E^*) value is the equivalent of reduced modulus during quasi static testing and is given as

$$E^* = E' + iE'' \qquad (7.1)$$

where E' and E'' are storage modulus and loss modulus respectively. E' and E'' are calculated from storage stiffness and loss stiffness respectively which are in turn calculated using phase and amplitude values [41]. The modulus map of 2X2 µm area on the sample surface is shown in Fig. 7.7. The line profile of complex modulus along the black horizontal line on Fig. 7.7 (a) is shown in Fig. 7.7 (b). The elastic modulus values of the alloying elements Pb and W are 16 GPa and

411 GPa respectively. Since there is a large difference in their modulus values line plot of the modulus map can be used to understand how Pb and W are distributed in the Al matrix. High modulus values are seen where ever the brighter spots are present indicating the presence of harder W phase. The average elastic modulus value obtained from the modulus maps is ~ 96 GPa which is in good agreement with the value obtained from indentation tests (~ 90 GPa). The elastic modulus value obtained is higher than the modulus calculated using rule of mixtures (~ 72 GPa) as well as the value calculated from inverse rule of mixtures (~ 66 GPa). The modulus mapping studies shall be used to identify the distribution of various phases based on the contrast variations, but shall not be used to measure the absolute value of the respective phases.

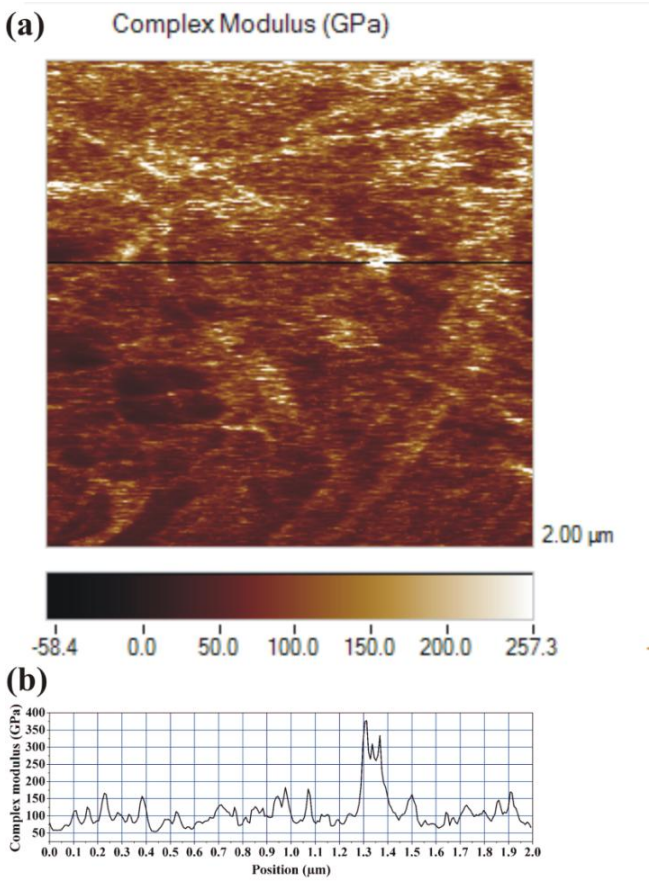

Fig. 7.7 (a) The modulus map of 2X2 µm area on the sample surface of nanocrystalline Al-Pb-W alloy (b) The line profile of complex modulus along the black horizontal line shown in (a).

If the absolute value is required, it is recommended to calculate the same from load-displacement data [42, 43].

SRS and activation volume (v^*) are two key parameters to understand the loading rate dependence of flow stress [44]. It is well known that flow stress is a function of strain, loading rate/strain rate, temperature and microstructure i.e., $\sigma = f(\varepsilon, \dot{\varepsilon}, T, S)$ [45]; Where σ is flow stress, ε is applied strain, T is temperature and S represents the microstructure. As depicted in below differential equation eq. (1).

$$d\sigma = \left(\frac{\partial \sigma}{\partial \varepsilon}\right) d\varepsilon + \left(\frac{\partial \sigma}{\partial \dot{\varepsilon}}\right) d\dot{\varepsilon} + \left(\frac{\partial \sigma}{\partial T}\right) dT + \left(\frac{\partial \sigma}{\partial S}\right) dS \qquad (7.2)$$

Flow stress gets influenced if one or more of these parameters $(\varepsilon, \dot{\varepsilon}, T, S)$ are changed. At constant microstructure and temperature, one can obtain the SRS by using $m = (\partial \ln \sigma / \partial \ ln \ \dot{\varepsilon}) = (\partial \ln(H/3) / \partial \ ln \ \dot{\varepsilon})$; $\sigma \approx H/3$ as per Tabor's relation [46], loading rate divided by the peak load is considered as the effective strain rate ($\dot{\varepsilon}$). Traditionally SRS is evaluated using strain rate jump tests as per ASTM testing procedures, however in the current investigation samples are smaller in size in addition to the finer microstructural features, nanoindentation has been used at room temperature to evaluate SRS and v^*. v^* is calculated using the below equations.

$$v^* = \sqrt{3} kT \left(\frac{\partial \ln \dot{\varepsilon}}{\partial \sigma}\right) = 3\sqrt{3} kT \left(\frac{\partial \ln \dot{\varepsilon}}{\partial H}\right) \qquad (7.3)$$

SRS is measured from the slope of yield strength vs strain rate plots (Fig. 7.8) for different peak forces of 1000 µN and 8000 µN. SRS values of 0.067 and 0.076 are obtained for peak forces of 1000 µN and 8000 µN respectively. In order to represent the bulk deformation behavior of the sample under investigation, a total 49 indentations were performed at a given set of load and loading rate. Loading rates were also varied and sampling was done at various locations.

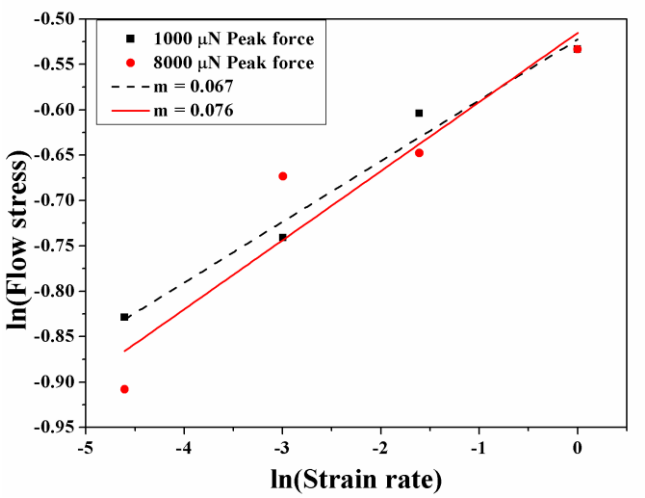

Fig. 7.8 Stress vs strain rate plots on natural logarithmic scale obtained from nanoindentation data at peak forces of 1000 μN and 8000 μN.

Traditionally, SRS is measured at constant microstructure [45]. In this alloy system, as the microstructure is homogeneous, it is expected that similar type of microstructural entities are subjected to deformation at various loads and loading rates using nanoindentation. Therefore the SRS values presented here are the apparent SRS of the material. Even though there is a decrease in hardness of nc Al matrix with the addition of nc Pb and nc W in comparison to pure nc Al [28], the SRS of Al-Pb-W alloy (0.071) is higher than that of nc Al (0.036).

SRS of several metals and alloys reported so far suggest that SRS of nc fcc metals has increased whereas SRS of nc bcc metals has decreased in comparison to their coarse grained counterparts [6, 7]. Our recent investigations revealed that nc Al (fcc) possesses an SRS of 0.036 [28]. When this nc Al is alloyed with various amounts of Pb (fcc), the overall SRS of the composite has increased, Al-1%Pb composite had an SRS of 0.043 [24]. However when a bcc W phase is added to nc Al, SRS of the composite has decreased to 0.024 [25]. In the present study, nc Al is alloyed with 1% of Pb and 1% of W simultaneously and it resulted an SRS of 0.071. It is to be noted that, in all these composites, activation volume did not get effected and remained nearly constant (4.6-6.4 b^3) (Fig. 7.9).

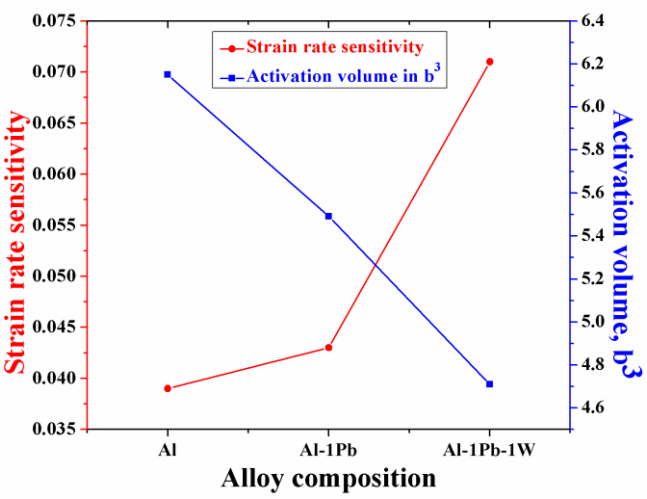

Fig. 7.9 Strain rate sensitivity (SRS) and activation volume of nanocrystalline Al, Al-1at.%Pb and Al-1at.%Pb-1at.%W alloys indicating increasing trend for SRS and decreasing trend for activation volume with the addition of Pb and W.

Fig. 7.9 clearly shows the influence of second phase particles and their crystal structures (fcc vs bcc) on SRS and activation volume which is the uniqueness of this report. It also highlights that presence of multiple phases could enhance the SRS of nc materials. In a study by Niu et al [47], it was observed using nanoindentation in multi-layer thin films that Cu-Cr (fcc-bcc) films possessed a SRS in the range 0.022-0.031. Whereas Cu-Zr (fcc-hcp) films possessed a SRS in the range 0.012-0.025. It suggests that when a single phase bcc is added to afcc phase, SRS is not affected greatly which is evident from refs. [25, 47]. However when a fcc phase and a bcc phases are added in conjunction to a fcc matrix, although in minor quantities, SRS is greatly enhanced which is the outcome of the present report.

Koch pointed out that presence of second phases could delay onset of necking and thereby increasing the ductility of nc materials [48]. Various studies on nc materials indicate that SRS is a good measure of ductility [17, 49, 50]. High SRS value of ~ 0.22 was obtained for ultra-fine grained Al-30wt.%Zn alloy [51, 52] and it showed unusually high ductility with elongation to failure of more than 150%. The authors suggested that the high ductility observed is due to grain

boundary sliding which is controlled by Zn diffusion along Al/Al grain boundaries. In the current study, the higher SRS and lower activation volume values obtained might be due to grain boundary mediated deformation processes [3]. Nanocrystalline Al-1%Pb alloy possessed a SRS of 0.043, addition of 1%W to this alloy further enhanced the overall SRS to 0.071 (Fig. 7.9). As W is bcc, it is expected that the overall SRS would decrease from 0.043 observed for nc Al-1%Pb alloy. Therefore this study suggests that the synergistic effects of presence of nc multi phases, albeit in minor proportions, would enhance the overall SRS of nc metals.

7.4 Summary and conclusions

I*n-situ* consolidation ball milling of nc Al-Pb-W alloy resulted in the formation of chunks of varying sizes from 2 mm to 6 mm. XRD and TEM studies did not indicate the formation of any solid solution or non-equilibrium meta-stable phases. Nanocrystalline Al matrix had a grain size of 23 nm. This novel multi-phase alloy showed a high SRS value of 0.071±0.004 and an activation volume of $4.71b^3$. The higher SRS and lower activation volume values suggest that grain boundary mediated processes govern the mechanics of plasticity in this novel alloy. The synergistic effect of presence of both Pb and W phases on enhancement of SRS to a value of 0.071 is evidenced. It is clear from the present study that multi-phase nc materials offer exciting opportunities to tune the SRS and thereby developing novel bulk nc materials with desired mechanical properties. The modulus mapping studies of the bulk sample enabled mapping of elastic modulus of the material surface by dynamic mechanical analysis and in-situ scanning probe microscopy (SPM) imaging and distribution of various phases could be identified at finer length scales using modulus mapping provided there is a significant variation in the elastic moduli of participating phases.

References

[1] K.S. Kumar, H. Van Swygenhoven, S. Suresh, Mechanical behavior of nanocrystalline metals and alloys, Acta Materialia, 51 (2003) 5743-5774.

[2] M.A. Meyers, A. Mishra, D.J. Benson, Mechanical properties of nanocrystalline materials, Progress in Materials Science, 51 (2006) 427-556.

[3] H. Van Swygenhoven, J.R. Weertman, Deformation in nanocrystalline metals, Materials Today, 9 (2006) 24-31.

[4] R. Valiev, Y. Estrin, Z. Horita, T. Langdon, M. Zechetbauer, Y. Zhu, Producing bulk ultrafine-grained materials by severe plastic deformation, JOM, 58 (2006) 33-39.

[5] C.C. Koch, K.M. Youssef, R.O. Scattergood, K.L. Murty, Breakthroughs in optimization of mechanical properties of nanostructured metals and alloys, Advanced Engineering Materials, 7 (2005) 787-794.

[6] Q. Wei, S. Cheng, K.T. Ramesh, E. Ma, Effect of nanocrystalline and ultrafine grain sizes on the strain rate sensitivity and activation volume: fcc versus bcc metals, Materials Science and Engineering: A, 381 (2004) 71-79.

[7] K. Darling, M. Tschopp, R. Guduru, W. Yin, Q. Wei, L. Kecskes, Microstructure and mechanical properties of bulk nanostructured Cu–Ta alloys consolidated by equal channel angular extrusion, Acta Materialia, 76 (2014) 168-185.

[8] R.J. Asaro, S. Suresh, Mechanistic models for the activation volume and rate sensitivity in metals with nanocrystalline grains and nano-scale twins, Acta Materialia, 53 (2005) 3369-3382.

[9] J. May, H.W. Höppel, M. Göken, Strain rate sensitivity of ultrafine-grained aluminium processed by severe plastic deformation, Scripta Materialia, 53 (2005) 189-194.

[10] L. Lu, R. Schwaiger, Z. Shan, M. Dao, K. Lu, S. Suresh, Nano-sized twins induce high rate sensitivity of flow stress in pure copper, Acta Materialia, 53 (2005) 2169-2179.

[11] J. Chen, L. Lu, K. Lu, Hardness and strain rate sensitivity of nanocrystalline Cu, Scripta Materialia, 54 (2006) 1913-1918.

[12] D. Gianola, D. Warner, J.-F. Molinari, K. Hemker, Increased strain rate sensitivity due to stress-coupled grain growth in nanocrystalline Al, Scripta Materialia, 55 (2006) 649-652.

[13] K. Jonnalagadda, N. Karanjgaokar, I. Chasiotis, J. Chee, D. Peroulis, Strain rate sensitivity of nanocrystalline Au films at room temperature, Acta Materialia, 58 (2010) 4674-4684.

[14] V. Maier, K. Durst, J. Mueller, B. Backes, H.W. Höppel, M. Göken, Nanoindentation strain-rate jump tests for determining the local strain-rate sensitivity in nanocrystalline Ni and ultrafine-grained Al, Journal of Materials Research, 26 (2011) 1421-1430.

[15] Y. Wang, E. Bringa, J. McNaney, M. Victoria, A. Caro, A. Hodge, R. Smith, B. Torralva, B. Remington, C. Schuh, Deforming nanocrystalline nickel at ultrahigh strain rates, Applied physics letters, 88 (2006) 061917.

[16] B. Ahn, R. Mitra, A. Hodge, E.J. Lavernia, S. Nutt, Strain rate sensitivity studies of cryomilled Al alloy performed by nanoindentation, in: Materials Science Forum, Trans Tech Publ, 2008, pp. 221-226.

[17] Y.M. Wang, E. Ma, Strain hardening, strain rate sensitivity, and ductility of nanostructured metals, Materials Science and Engineering: A, 375–377 (2004) 46-52.

[18] Y. Shen, L. Lu, M. Dao, S. Suresh, Strain rate sensitivity of Cu with nanoscale twins, Scripta materialia, 55 (2006) 319-322.

[19] I.-C. Choi, Y.-J. Kim, Y.M. Wang, U. Ramamurty, J.-i. Jang, Nanoindentation behavior of nanotwinned Cu: Influence of indenter angle on hardness, strain rate sensitivity and activation volume, Acta Materialia, 61 (2013) 7313-7323.

[20] Y. Liu, J. Hay, H. Wang, X. Zhang, A new method for reliable determination of strain-rate sensitivity of low-dimensional metallic materials by using nanoindentation, Scripta Materialia, 77 (2014) 5-8.

[21] J. Alkorta, J.M. Martínez-Esnaola, J. Gil Sevillano, Critical examination of strain-rate sensitivity measurement by nanoindentation methods: Application to severely deformed niobium, Acta Materialia, 56 (2008) 884-893.

[22] T. Kunimine, N. Takata, N. Tsuji, T. Fujii, M. Kato, S. Onaka, Temperature and strain rate dependence of flow stress in severely deformed copper by accumulative roll bonding, Materials transactions, 50 (2009) 64.

[23] J.R. Trelewicz, C.A. Schuh, The Hall–Petch breakdown in nanocrystalline metals: A crossover to glass-like deformation, Acta Materialia, 55 (2007) 5948-5958.

[24] S. Varam, K.V. Rajulapati, K.B.S. Rao, R.O. Scattergood, K.L. Murty, C.C. Koch, Loading Rate-Dependent Mechanical Properties of Bulk Two-Phase Nanocrystalline Al-Pb Alloys Studied by Nanoindentation, Metallurgical and Materials Transactions A, 45 (2014) 5249-5258.

[25] S. Varam, P. Narayana, M.D. Prasad, D. Chakravarty, K.V. Rajulapati, K. Bhanu Sankara Rao, Strain rate sensitivity of bulk multi-phase nanocrystalline Al–W-based alloy, Philosophical Magazine Letters, 94 (2014) 582-591.

[26] U. Dahmen, S. Xiao, S. Paciornik, E. Johnson, A. Johansen, Magic-size equilibrium shapes of nanoscale Pb inclusions in Al, Physical review letters, 78 (1997) 471.

[27] T. Mizoguchi, U. Dahmen, 3D shape and orientation of nanoscale Pb inclusions at grain boundaries in Al observed by TEM and STEM tomography, Philosophical Magazine Letters, 89 (2009) 104-112.

[28] S. Varam, K.V. Rajulapati, K. Bhanu Sankara Rao, Strain rate sensitivity studies on bulk nanocrystalline aluminium by nanoindentation, Journal of Alloys and Compounds, 585 (2014) 795-799.

[29] N. Mukhopadhyay, P. Paufler, Micro-and nanoindentation techniques for mechanical characterisation of materials, International materials reviews, 51 (2006) 209-245.

[30] A.A. Elmustafa, D.S. Stone, Indentation size effect in polycrystalline F.C.C. metals, Acta Materialia, 50 (2002) 3641-3650.

[31] A.A. Elmustafa, D.S. Stone, Nanoindentation and the indentation size effect: Kinetics of deformation and strain gradient plasticity, Journal of the Mechanics and Physics of Solids, 51 (2003) 357-381.

[32] W.D. Nix, H. Gao, Indentation size effects in crystalline materials: a law for strain gradient plasticity, Journal of the Mechanics and Physics of Solids, 46 (1998) 411-425.

[33] G. Palumbo, S.J. Thorpe, K.T. Aust, On the contribution of triple junctions to the structure and properties of nanocrystalline materials, Scripta Metallurgica et Materialia, 24 (1990) 1347-1350.

[34] S. Jang, Y. Purohit, D.L. Irving, C. Padgett, D. Brenner, R.O. Scattergood, Influence of Pb segregation on the deformation of nanocrystalline Al: Insights from molecular simulations, Acta Materialia, 56 (2008) 4750-4761.

[35] K.V. Rajulapati, R.O. Scattergood, K.L. Murty, G. Duscher, C.C. Koch, Effect of Pb on the mechanical properties of nanocrystalline Al, Scripta Materialia, 55 (2006) 155-158.

[36] K.V. Rajulapati, R.O. Scattergood, K.L. Murty, Z. Horita, T.G. Langdon, C.C. Koch, Mechanical properties of bulk nanocrystalline aluminum-tungsten alloys, Metallurgical and Materials Transactions A, 39 (2008) 2528-2534.

[37] H.W. Sheng, F. Zhou, Z.Q. Hu, K. Lu, Investigation of Al-Pb nanocomposites synthesized by non-equilibrium processes, Journal of Materials Research, 13 (1998) 308-315.

[38] M.A. Atwater, D. Roy, K.A. Darling, B.G. Butler, R.O. Scattergood, C.C. Koch, The thermal stability of nanocrystalline copper cryogenically milled with tungsten, Materials Science and Engineering: A, 558 (2012) 226-233.

[39] T.J. Rupert, J.R. Trelewicz, C.A. Schuh, Grain boundary relaxation strengthening of nanocrystalline Ni–W alloys, Journal of Materials Research, 27 (2012) 1285-1294.

[40] S.P. Pemmasani, K.V. Rajulapati, M. Ramakrishna, K. Valleti, R.C. Gundakaram, S.V. Joshi, Characterization of multilayer nitride coatings by electron microscopy and modulus mapping, Materials Characterization, 81 (2013) 7-18.

[41] Modulus Mapping User Manual, Hysitron, 2009.

[42] W.C. Oliver, G.M. Pharr, An Improved Technique for Determining Hardness and Elastic Moduli using Load and Displacement Sensing Indentation Experiments, Journal of Materials Research, 7 (1992) 1564-1583.

[43] W.C. Oliver, G.M. Pharr, Measurement of hardness and elastic modulus by instrumented indentation: Advances in understanding and refinements to methodology, Journal of materials research, 19 (2004) 3-20.

[44] G.E. Dieter, Mechanical metallurgy, third ed. ed., McGraw-Hill Book Company, Boston, 1986.

[45] A. Ghosh, On the measurement of strain-rate sensitivity for deformation mechanism in conventional and ultra-fine grain alloys, Materials Science and Engineering: A, 463 (2007) 36-40.

[46] D. Tabor, The hardness and strength of metals, Journal Institute of Metals, 79 (1951) 1-18.

[47] J.J. Niu, J.Y. Zhang, G. Liu, P. Zhang, S.Y. Lei, G.J. Zhang, J. Sun, Size-dependent deformation mechanisms and strain-rate sensitivity in nanostructured Cu/X (X=Cr, Zr) multilayer films, Acta Materialia, 60 (2012) 3677-3689.

[48] C.C. Koch, Optimization of strength and ductility in nanocrystalline and ultrafine grained metals, Scripta Materialia, 49 (2003) 657-662.

[49] Y.T. Zhu, X.Z. Liao, Nanostructured metals - Retaining ductility, Nature Materials, 3 (2004) 351–352.

[50] T. Zhu, J. Li, A. Samanta, H.G. Kim, S. Suresh, Interfacial plasticity governs strain rate sensitivity and ductility in nanostructured metals, Proc. Natl Acad. Sci., (2007) 3031–3036.

[51] N.Q. Chinh, T. Csanádi, J. Gubicza, R.Z. Valiev, B.B. Straumal, T.G. Langdon, The effect of grain boundary sliding and strain rate sensitivity on the ductility of ultrafine-grained materials, Materials Science Forum, 667-669 (2011) 677-682.

[52] N.Q. Chinh, T. Csanádi, T. Győri, R.Z. Valiev, B.B. Straumal, M. Kawasaki, T.G. Langdon, Strain rate sensitivity studies in an ultrafine-grained Al–30 wt.% Zn alloy using micro- and nanoindentation, Materials Science and Engineering A, 543 (2012) 117-120.

Chapter 8 – Structural and Mechanical Characterization of Nanocrystalline Al-Bi Alloys

8.1 Introduction

Al-Bi alloys are used as bearing materials. Importance of Bi as a replacement for lead is increasing as toxicity of lead is more. Nanocrystalline (nc) materials are observed to exhibit outstanding mechanical properties due to their fine grain structure [1, 2]. Studies on mechanical alloying in Al-Bi alloy system [3] showed the formation of non-equilibrium super-saturated solid solution. Though Al-Bi is an immiscible alloy system, through mechanical alloying, extended solubility of Al in Bi was observed in Al-30 at.% Bi alloy [3]. This resulted in depression in the melting temperature of Bi. The authors observed that the hardness of the powders increased with increasing mechanical alloying time, and the hardness was much higher than that calculated from the rule of mixtures [3]. Mechanical properties of cast microcrystalline Al-Bi alloys [4, 5] have been studied extensively. But, the mechanical properties of nc bulk samples synthesized by ball milling and consolidation have not been studied so far. In the present work, bulk nc Al-Bi alloys are synthesized using high energy ball milling followed by room temperature compaction and spark plasma sintering (SPS). Nanoindentation studies on the hardness behavior of nc Al with Bi addition showed reduction in hardness with increasing Bi content.

8.2 Materials and methods

Experimental procedure for the processing of Al-Bi alloys is same as in section 5.1 and elemental Bi powder (99.9% purity, Alfa Aesar) of -200 mesh particle size is used. Spark plasma sintering of compacted samples is carried out at 523 K. In addition to X-ray diffraction (XRD) and transmission electron microscopy (TEM), differential scanning calorimetry (DSC) studies also have been carried out for the milled Al-Bi alloy powders.

8.3 Results and discussion

The X-ray diffractograms obtained from ball milled powders (Fig. 8.1) as well as from bulk samples (Fig. 8.2) sintered at 523 K using SPS, showed only Al and Bi peaks indicating no solid solution formation. The lattice parameter values were measured using X-ray diffraction data and there was no considerable change in lattice parameter value of Al with Bi addition.

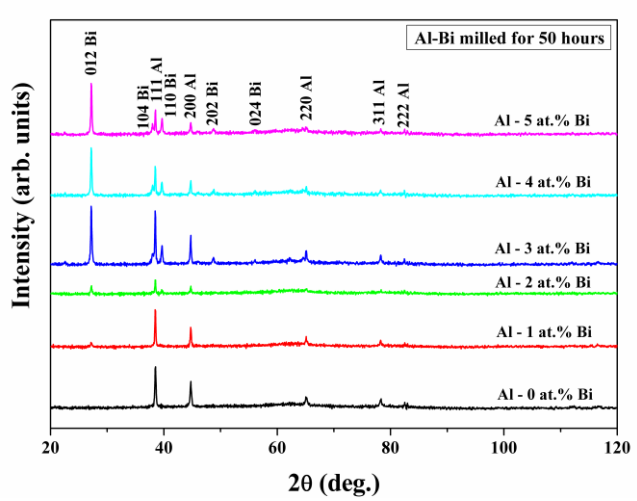

Fig. 8.1 X-ray diffractograms of ball milled Al-Bi nanocomposite powders.

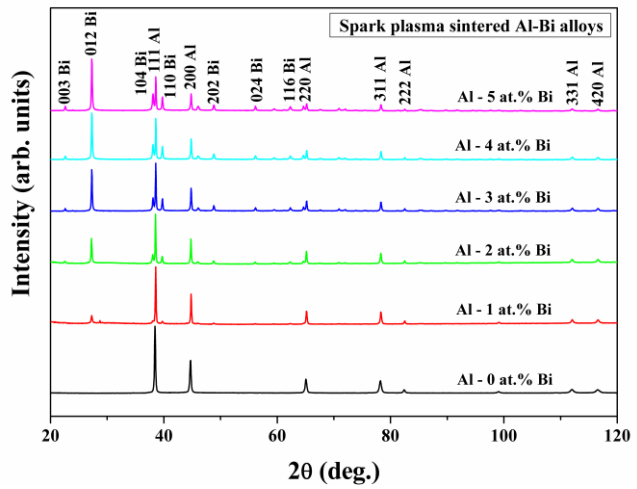

Fig. 8.2 X-ray diffractograms of spark plasma sintered Al-Bi nanocomposites.

Table 8-1 Grain size values of ball milled powders and sintered Al-Bi samples of various compositions measured using Scherrer formula from X-ray line broadening data.

Composition	Grain size, nm	
	Milled	**Sintered**
Al	43 ± 8	48 ± 13
Al-1at.%Bi	59 ± 14	77 ± 17
Al-2at.%Bi	68 ± 15	86 ± 21
Al-3at.%Bi	68 ± 12	81 ± 18
Al-4at.%Bi	78 ± 13	89 ± 23
Al-5at.%Bi	70 ± 14	85 ± 30

Table 8-1 shows the grain size values of ball milled powder (50 hrs of milling) and sintered Al-Bi samples of various compositions measured using Scherrer formula [6] from X-ray line broadening data after accounting for instrumental broadening. The grain size was observed to increase with the addition of Bi content. Since Bi is much softer than Al, Bi addition might be the reason for reduced milling efficiency. It is clear from the obtained grain size values of sintered samples that there is not much grain growth even after sintering. Fig. 8.3 (a) represents the dark-field transmission electron micrograph obtained from 25 hours milled Al-1at.%Bi powder showing the structure having nc grains along with few grains larger than 100 nm. The corresponding diffraction pattern of the micrograph is also shown in Fig. 8.3 (b). Al grain size distribution obtained from the dark field TEM micrographs with an average grain size of ~ 67 (± 25) nm is shown in Fig. 8.4.

DSC plots (Fig. 8.5, Fig. 8.6 and Fig. 8.7) showed depression in melting point of Bi in nc Al-Bi alloys. The temperature depression was more for alloys with smaller Bi additions upto 2at.%Bi (Fig. 8.6) when compared to those with larger Bi additions (Fig. 8.7).

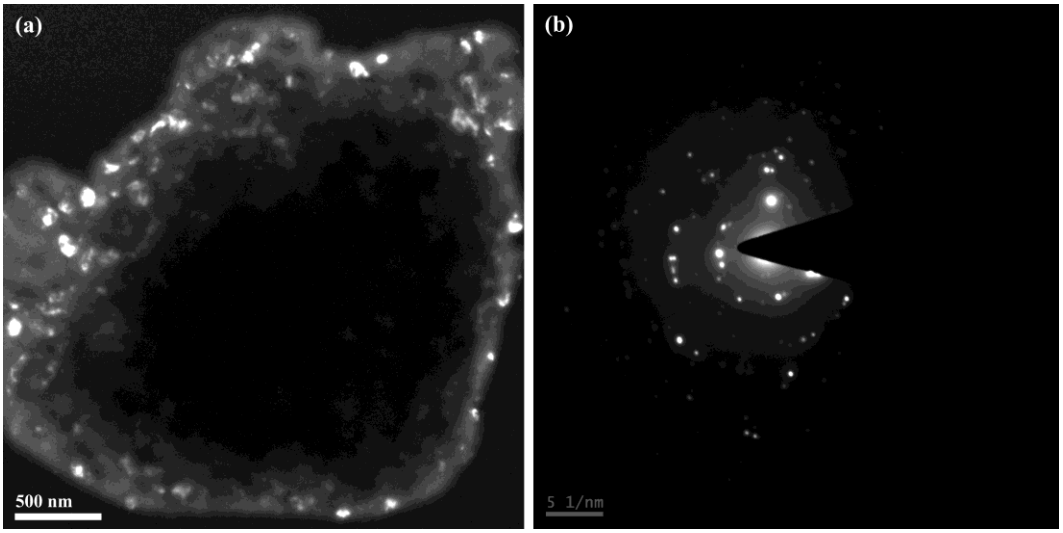

Fig. 8.3 (a) Dark field TEM micrograph and (b) corresponding selected area diffraction pattern of Al – 1 at. % Bi powder milled for 25 hours.

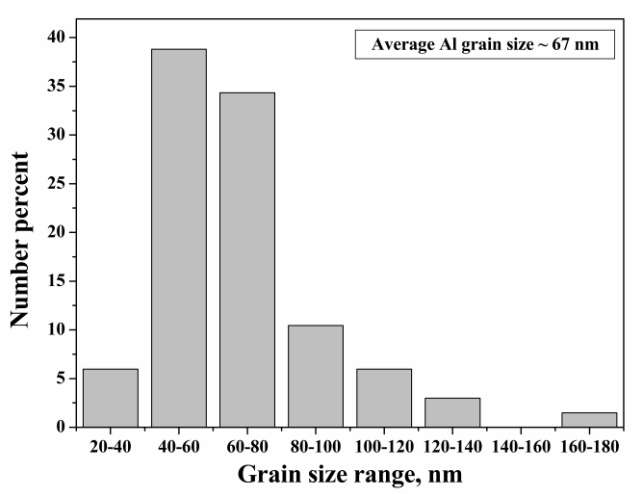

Fig. 8.4 Aluminium grain size distribution plot obtained from dark field TEM micrographs of Al–1at.% Bi powder milled for 25 hours.

Earlier studies on mechanical alloying in Al-Bi alloy system [3] showed the formation of non-equilibrium super-saturated solid solution. Though Al-Bi is an immiscible alloy system, through mechanical alloying, extended solubility of Al in Bi was observed in Al-30 at.% Bi alloy. Authors have reported that, this resulted in depression in the melting temperature of Bi. In the current study, decrease in melting temperature was observed, but no solid solution was formed.

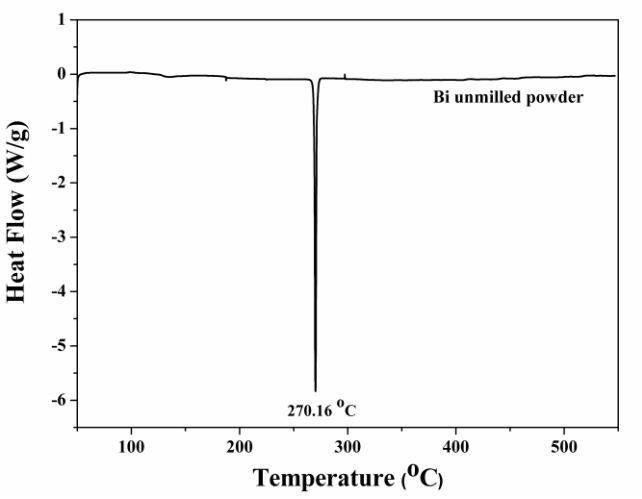

Fig. 8.5 Differential scanning calorimetry plot of unmilled Bi powder.

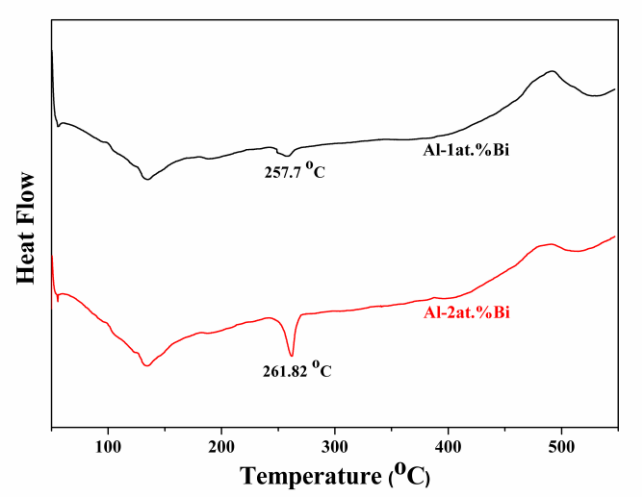

Fig. 8.6 Differential scanning calorimetry plots of milled Al-1at.%Bi and Al-2at.%Bi powders showing depression in melting point of Bi.

The sintered alloys were blackish in color. After polishing, the sample surface became silvery in color, possibly revealing the aluminium oxide layer. But, discoloration was observed on the samples with time on exposure to air for about 5-10 min, even though the samples were polished in kerosene medium. The discoloration seemed to have occurred due to the reaction of the material with the moisture present in the air. It was observed that the alloys were highly reactive with water. The samples seem to be producing hydrogen gas when they react with water.

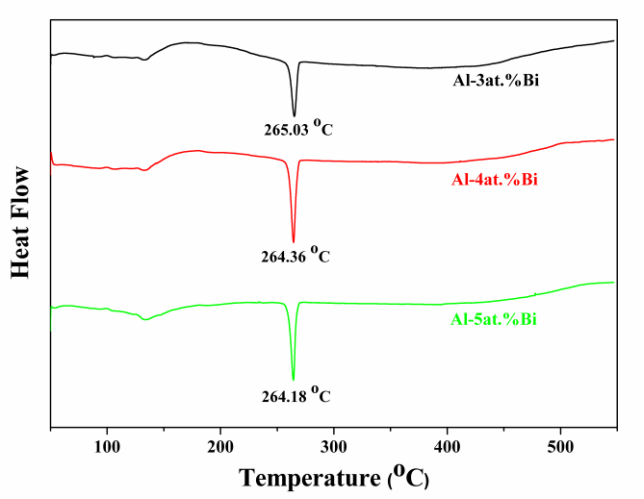

Fig. 8.7 Differential scanning calorimetry plots of milled Al-Bi alloy powders with 3-5at.% Bi content showing depression in melting point of Bi.

Experiments have not been carried out to confirm the hydrogen gas formation since it is out of the scope of the present project work. Based on the literature data [7] on Al-Bi alloys, hydrogen gas formation is considered and more details on this topic are discussed in Appendix I.

Sintered bulk nc Al-Bi alloy samples are shown in Fig. 8.8. Mechanical properties of cast microcrystalline Al-Bi alloys [4, 5] have been studied extensively. But, the mechanical properties of nc bulk samples synthesized by ball milling and consolidation have not been studied in detail so far. Fig. 8.9 shows the nanoindentation data of various Al-Bi alloy compositions at two different peak forces (5000 µN and 8000 µN) with a loading rate of 500 µN/s. The addition of Bi resulted in decreased hardness values of nc Al [8]. The trend of change in hardness with increasing Bi addition is not very clear. Initially the hardness decreased with increase in Bi content up to 3 at.%, then the hardness increased for 4 at.% and 5 at.% Bi addition. Large scatter was observed in the obtained hardness data and the alloy with 2 at.% Bi which got exposed to water while polishing showed much larger scatter.

Fig. 8.8 Sintered bulk nc Al-Bi alloy samples.

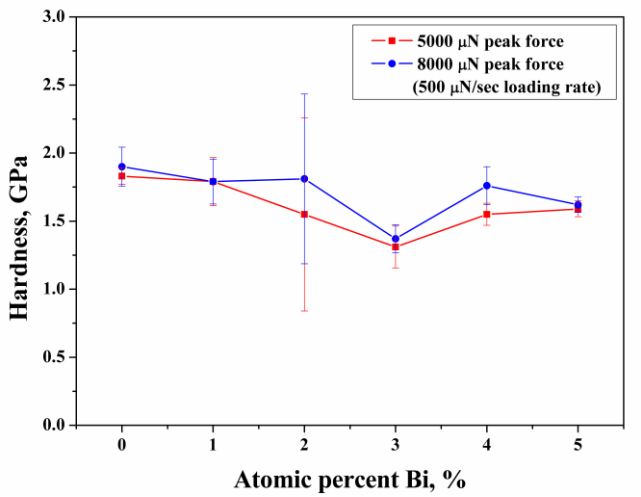

Fig. 8.9 The nanoindentation data of various Al-Bi alloy compositions at two different peak forces of 5000 μN and 8000 μN.

In the earlier work [3] it was observed that the hardness of the powders increased with increasing mechanical alloying time, and the hardness was much higher than that calculated from the rule of mixtures. Since the nc Al-Bi alloys synthesized in the current study are unstable in air, further investigations are not continued and these alloys might not be good candidates for structural applications.

8.4 Summary and conclusions

Bulk nc Al-Bi alloys were synthesized using high energy ball milling followed by high pressure consolidation at room temperature and SPS. The X-ray diffractograms showed only Al and Bi peaks indicating no solid solution formation. Nanocrystalline structure was evident from the TEM micrographs. Decrease in melting point of Bi was observed from DSC data. Nanoindentation studies on the hardness behavior of nc Al with Bi addition showed reduction in hardness with increasing Bi content. The alloys were found to be unstable in air. Further investigations on the structure-property correlation, were not continued considering that these alloys might not be good candidates for structural applications. Nanocrystalline Al-Bi alloys were observed to be highly reactive in water and in future, experimental studies on possible production of hydrogen gas from these alloys shall be considered.

References

[1] K.S. Kumar, H. Van Swygenhoven, S. Suresh, Mechanical behavior of nanocrystalline metals and alloys, Acta Materialia, 51 (2003) 5743-5774.

[2] M.A. Meyers, A. Mishra, D.J. Benson, Mechanical properties of nanocrystalline materials, Progress in Materials Science, 51 (2006) 427-556.

[3] K. Uenishi, K.H. Yong, K.F. Kobayashi, Mechanical alloying in the AI-Bi alloy system, Journal of Materials Science, 31 (1996) 3605-3611.

[4] K. Lepper, M. James, J. Chashechkina, D. Rigney, Sliding behavior of selected aluminum alloys, Wear, 203 (1997) 46-56.

[5] J. Koike, K. Miki, K. Maruyama, H. Oikawa, Influence of liquid-phase inclusion on high-temperature deformation behavior in Al-Bi alloys, Materials Science and Engineering: A, 234–236 (1997) 525-528.

[6] B.D. Cullity, Elements of X-ray Diffraction, Addison-Wesley Publishing Company, Inc., Reading, Massachusetts, 1956.

[7] M.-Q. Fan, F. Xu, L.-X. Sun, Hydrogen generation by hydrolysis reaction of ball-milled Al-Bi alloys, Energy & fuels, 21 (2007) 2294-2298.

[8] S. Varam, K.V. Rajulapati, K. Bhanu Sankara Rao, Strain rate sensitivity studies on bulk nanocrystalline aluminium by nanoindentation, Journal of Alloys and Compounds, 585 (2014) 795-799.

Chapter 9 – Summary and Conclusions

Nanocrystalline (nc) bulk Al samples fabricated by room temperature high pressure compaction (at 1.5 GPa) are of ~ 98 % of theoretical density. Transmission electron micrographs showed an average Al grain size of ~ 42 nm. Precise lattice parameter value of sintered nc Al calculated using Nelson-Riley extrapolation function is 4.0479 ± 0.0005 Å, which is in good agreement with the standard literature value of 4.0495 Å. Hardness and elastic modulus values measured using depth sensing nanoindentation are 1.67 ± 0.09 GPa and 83 ± 8 GPa respectively at an applied peak force of 8000 µN and a strain rate of 10^{-2} s^{-1}. Average strain rate sensitivity (SRS) of nc Al obtained from nanoindentation data is 0.035. High SRS of 0.054 obtained for an applied peak force of 8000 µN qualitatively indicates good ductility of nc Al.

Bulk samples of various nc Al-Pb alloys (with 1-4 at.% Pb) are fabricated using spark plasma sintering of ball milled powders. High angle annular dark field image obtained in STEM mode of TEM indicates the presence of Pb along the nc Al grain boundaries as well as dispersion of smaller Pb particles in the intra-granular regions. Hardness of Al-Pb alloys increased with increase in Pb content up to the additions of 2at.%Pb, beyond that the hardness is decreased. The initial hardening behavior is explained based on the Orowan particle strengthening. SRS has increased with increase in Pb content reaching a value of 0.1 for Al-4at.%Pb alloy. Higher SRS and lower activation volume (2.84-6.15 b^3) suggest that grain boundary mediated processes are controlling the deformation characteristics.

A bulk nanostructured multi-phase Al-10at.%W nanocomposite fabricated using a combination of ball milling and spark plasma sintering at 748 K was characterized by TEM. Nanocrystalline intermetallic $Al_{12}W$ phase with an average particle size of 175 nm is uniformly distributed in the nc Al matrix with a grain size of 40 nm. The nanoindentation studies carried

out earlier yielded high hardness of 5.42±0.33 GPa and an elastic modulus of 145±5 GPa at an applied peak force of 6000 µN. A SRS value of 0.025±0.002 was measured with a very low activation volume of 1.63-3.88 b^3 as the peak load varied from 6000 µN to 8000 µN. The superior mechanical properties of this nanocomposite could be because of an aluminum matrix with a grain size of 40 nm, a nanocrystalline second phase ($Al_{12}W$) and its uniform distribution throughout the matrix. It is also expected that finer $Al_{12}W$ particles might be contributing significantly through Orowan strengthening to the enhanced mechanical properties. The interfacial regions viz., grain boundaries in the matrix and reinforcement, triple junctions in the matrix and the reinforcement, matrix/particle boundaries etc. could be governing the strain rate sensitivity and activation volume of the composite.

Nanocrystalline Al-Pb-W composite (grain size ~ 23 nm) fabricated by *in-situ* consolidation ball milling showed lower microhardness value of ~ 1 GPa where as nc Al (~42 nm) fabricated by ball milling and cold compaction showed slightly higher hardness values (1.29±0.04 GPa and 1.15±0.04 GPa at 50 g and 200 g respectively). The segregation of alloying elements at the grain boundaries is expected to be more when the matrix grain size is low (~23 nm) because of the larger volume fractions of grain boundary and other interfacial regions at such a smaller grain size. Hence the grain boundary mediated deformation processes are expected to dominate in this material. This could be the reason for softening of the Al matrix with Pb and W addition. The material showed a high SRS value of 0.071±0.004. The modulus mapping studies of the bulk sample enabled mapping of elastic modulus of the material surface by dynamic mechanical analysis and in-situ scanning probe microscopy (SPM) imaging. The higher SRS and lower activation volume values obtained might be due to grain boundary mediated deformation processes.

Bulk nc Al-Bi alloys are synthesized using high energy ball milling followed by high pressure consolidation at room temperature and spark plasma sintering. The X-ray diffractograms showed only Al and Bi peaks indicating no solid solution formation. Nanocrystalline structure was evident from the TEM micrographs. Decrease in melting point of Bi was observed from DSC data. Nanoindentation studies on the hardness behavior of nc Al with Bi addition showed reduction in hardness with increasing Bi content. The alloys are found to be unstable in air, hence they may not be considered as good candidates for structural applications. These alloys are found to be highly reactive in water and the studies on possible use of these alloys for hydrogen generation shall be considered in future.

The major outcome of this investigation is that nanocrystalline Al (fcc) possessed an SRS of 0.35; when fcc structured Pb is added, the overall SRS of nanocrystalline fcc-fcc composite has increased. When a bcc structured W is added, the overall SRS of nanocrystalline fcc-bcc composite has slightly decreased. However, when fcc-Pb and bcc-W are simultaneously added, the overall SRS of nanocrystalline fcc-fcc-bcc composite has increased to 0.071. This suggests that the reasonable ductility levels could be imparted to nanocrystalline metals using multi-phase structures. It is to be noted that the Activation Volume is nearly constant in all these alloys.

Chapter 10 - Future Scope of Work

- Warm compaction methods may be employed for nanocrystalline Al and Al alloy powders to optimize the process parameters for obtaining maximum density
- High resolution imaging of the bulk samples to investigate the possibility of twinning especially in *in-situ* consolidated nanocrystalline Al-Pb-W alloy
- High load nanoindentation studies may be conducted on all the bulk samples
- Automated ball indentation studies and the micro tensile testing studies to quantitatively measure percentage elongation which can be further correlated with the obtained strain rate sensitivity (SRS) values for various alloys
- To study the compressive behavior of the bulk alloy samples
- SRS studies of various alloys by changing the matrix and dispersoids having different crystal structures (fcc/bcc/hcp)
- Investigate the effect of grain size of the matrix phase and particle size of the dispersoid on SRS
- Evaluation of comprehensive theory on SRS of multi-phase nc materials
- As nanocrystalline Al-Bi alloys are found to be highly reactive with water, hydrolysis studies of the alloy powders may be carried out for possible generation of hydrogen gas which may be obtained on demand

Appendix I – Nanocrystalline Al-Bi Alloys for Hydrogen Generation

Since the resources of natural oil, gas and coal are getting depleted, there is a need for alternate energy sources. Hydrogen is one of the alternate sources of energy and the problems of hydrogen storage and transportation associated with hydrogen power engineering (HPE) could be solved by obtaining hydrogen on demand for example hydrogen as mobile energy source for automobiles. Experimental studies on Al nano powder for hydrogen generation have been carried out already [1]. The studies showed that the rate of hydrogen extraction when Al nano powder interacts with distilled water at 60 $^{\circ}$C is 70 times more than the rate of extraction through hydrothermal synthesis. The authors experimentally observed the self-heating effect due to the excess temperature inside nano particles when compared to environmental temperature which might be causing the chemical reaction to occur. It was also observed that decrease in water boiling temperature occurs by adding Al nano powder to water. Interaction of Al nano powder with water also resulted in interaction products having cellular structure which may be used as functional materials.

Energy storing substances (ESS) based on Al and Mg activated with various metals-activators like Bi, Ga and In [2], have been used to produce hydrogen for the development of HPE. Nanostructured Al-Mg alloys with alloying elements were produced by crystallization under non-equilibrium conditions by utilizing high alloy cooling rates while casting and these alloys were used to generate hydrogen with high evolution rates. When these alloys react with water at moderate temperatures, dissolution of activated Al in water was caused by intercrystalline corrosion by formation of micro galvanic cells. In the micro galvanic cells formed, Al and Mg, being electro negative elements, act as anode and the interfaces between

grains rich in metals-activators - Bi, Ga or In act as cathode. Investigations on generation of hydrogen by hydrolysis reaction of ball-milled Al-Bi alloys in different media have been carried out by Fan et.al. [3]. Milling of the alloy powders was carried out in a planetary ball mill and the milled powders were subjected to hydrolysis. Conversion yield of 89.88% was obtained during the hydrolysis reaction of Al-16wt%Bi alloy with pure water at room temperature. They also observed that with increasing milling time, the hydrolysis reaction rate increased. They emphasized that the uniform distribution of Bi in Al resulted in higher reactivity of the alloys. Fan et.al. [4] have also studied the hydrolysis of milled Al-Li-Bi alloys for hydrogen generation. They indicated that these alloys have potential applications in fuel cell to produce portable hydrogen. Various studies have been carried out on hydrogen generation for fuel cell applications from the reaction between Al and water [5, 6]. The detailed study on the effect of nanograined structure on the hydrolysis reaction rate of Al-Bi alloys has not been studied so far.

In the present work, the nanocrystalline Al-Bi alloys synthesized were found to be highly reactive with water. The ball milled powder was blackish in color. The sintered pellets were also blackish in color. Passive layer of aluminium oxide layer was observed on the surface of the samples immediately after polishing, but again, the samples became blackish in color with time. Bubbles formed and heat was produced when the sintered alloys came in contact with water at room temperature, possibly due to the generation of hydrogen gas. It was also observed that these alloys have high reactivity with moisture content present in the air. The alloys have formed some reaction product when left in normal air atmosphere. The reaction product was not analyzed further since this study is beyond the scope of the present work. The nanocrystalline structure of the alloys might be causing the high reactivity of these alloy composites with water. Based on the literature data available on Al nano powder [1] and various Al-based alloys [2-4]

and the above mentioned experimental observations, nanocrystalline Al-Bi alloys could be considered as having potential applications as energy storing materials and further detailed investigations on hydrolysis of these alloys for generation of hydrogen gas can be carried out in future.

References

[1] A.P. Ilyin, A.V. Korshunov, L.O. Tolbanova, Application of aluminum nanopowder in hydrogen power engineering, Bulletin of the Tomsk Polytechnic University, 311 (2007).

[2] L.F. Kozin, S.V. Volkov, S.G. Goncharenko, B.I. Daniltsev, Problems of Development of Hydrogen Power Engineering, in: Y.Z. Svetlana, V.S. Dmitry, V.S. Valeriy, V. Ayfer, I. Beycan (Eds.) Carbon Nanomaterials in Clean Energy Hydrogen Systems - II, Springer, Netherlands, 2012, pp. 1-22.

[3] M.-Q. Fan, F. Xu, L.-X. Sun, Hydrogen generation by hydrolysis reaction of ball-milled Al-Bi alloys, Energy & fuels, 21 (2007) 2294-2298.

[4] M.-Q. Fan, D.-S. Mei, D. Chen, C.-J. Lv, K.-y. Shu, Portable hydrogen generation from activated Al–Li–Bi alloys in water, Renewable Energy, 36 (2011) 3061-3067.

[5] C.-C. Wang, Y.-C. Chou, C.-Y. Yen, Hydrogen Generation from Aluminum and Aluminum Alloys Powder, Procedia Engineering, 36 (2012) 105-113.

[6] X. Huang, T. Gao, X. Pan, D. Wei, C. Lv, L. Qin, Y. Huang, A review: Feasibility of hydrogen generation from the reaction between aluminum and water for fuel cell applications, Journal of Power Sources, 229 (2013) 133-140.